Optimization of organic solar cells (OPV devices) based on the semiconductor polymers MEH-PPV, P3HT and PIDT-PhanQ using PCBM as electron donor

Thesis submitted to Centro de Investigaciones en Óptica A.C. (CIO) in partial fulfillment
of the requirements for the degree of

Doctor in Science (Optics)

Presented by

José-Francisco Salinas-Torres, M. Sc.

Under the supervision of:

José-Luis Maldonado-Rivera, Ph. D.

Advisor

Group of Optical Properties of Materials (GPOM)
Photonics Division
Centro de Investigaciones en Óptica A.C.

León, Guanajuato, México

September 2013

Acknowledgments

This work was possible due to the help of some people to whom I want to acknowledge:

- To CONACyT and particularly to the project CONACyT-SENER 153094 for the economic help that allowed me to complete my doctoral studies and the research stay of one year at the University of Washington in Seattle.
- To Centro de Investigaciones en Optica for the space and equipment granted for the development of my doctoral studies.
- To Jose Luis Maldonado Rivera for his guidance during the whole doctoral work and also for the equipment (glove box, evaporator) that allowed me to work using first world standards in my own country.
- To Prof. Alex K. Jen for grant me the opportunity of being in his workgroup during one year, giving me inadvertently the chance to realize my true potential.
- To my parents, sisters and nieces, who believed in me even when I was unable to keep doing it.
- To my friends who contributed through their talk to make my job and my life easier.
- To Ismael Torres, Miguel Vargas, Xavier Mathew, Norberto Farfan and Esteban Jiménez for their advices during the several correction steps of this manuscript.

Abstract

Organic solar cells (OPV devices) are a new sort of photovoltaic devices whose reduced manufacturing cost and facility of fabrication will contribute to solve our dependence on fossil fuels, main reason of the current high levels of greenhouse gases and global warming. In this thesis several approaches were considered to unlock the full potential of organic solar devices: *i*) A low melting point eutectic alloy (Wood's metal) was used as substitute of evaporated aluminum allowing the manufacture of solar cell devices by a free vacuum steps process. Our method proved to be adequate to quickly test the photovoltaic performance (PCE = 0.8 %) of OPV cells based on MEH:PPV and an organo-boron molecule synthesized in our group. *ii*) For both methods (with and without vacuum steps) and using the conventional and inverted architectures, the photovoltaic behavior of OPVs based on the polymer P3HT was compared. Devices prepared under ambient conditions reached efficiencies as high as 2.2% employing the inverted architecture and 1.8% using Wood's metal. *iii*) A thin film optical simulator was developed to provide an optimization route for the development of high-performance solar cells based on ultra-thin silver films. The simulations were in good agreement with the experimental results, allowing the design of a micro-cavity based device of superior performance (PCE = 6.56% using PIDT-PhanQ) even compared to devices using ITO. *iv*) The optical simulator was employed on the design of semitransparent organic devices; by adequately choosing materials and electrodes, solar cells of neutral appearance were developed. The color quality was analyzed using the CIE 1931 color space. *v*) High performance semitransparent solar cells (PCE = 7.56%, using PBDTTT-C-T, Ag: 60 nm) were developed using a wide absorption polymer. Window application was evaluated by analyzing the color rendering index. For several degrees of transparency, neutral appearance with respect to the human eye was achieved. The color rendering indexes were the highest reported for organic solar devices (CRI = 97.3, Ag: 18 nm). Transparencies as high as 37.3 % with respect to the human eye were possible reducing the Ag thickness to 6 nm.

Table of Contents

1. Introduction

Organic solar cells are a new sort of photovoltaic devices whose reduced manufacturing cost and facility of fabrication promise to solve our dependence on fossil fuels, principal reason of the current high levels of green-house gases and global warming. Currently the atmospheric CO_2 levels are 40% higher than before the industrial revolution (when massive use of fossil fuels as source of energy started) [1] and earth's average temperature has approximately raised 1°C since then [2] (Figure 1). As consequence, disappearance of glaciers in mountains and polar areas, release of methane (another green-house gas) by the melting of permafrost in arctic zones, increased frequency of droughts and floods as effect of heat waves, replacement of jungle and forests with savanna and deserts, sea level rise and ocean acidification are some of the documented consequences that have been already observed all around the world and that will be intensified providing the green-house gas emissions continue increasing as they have done so far [3].

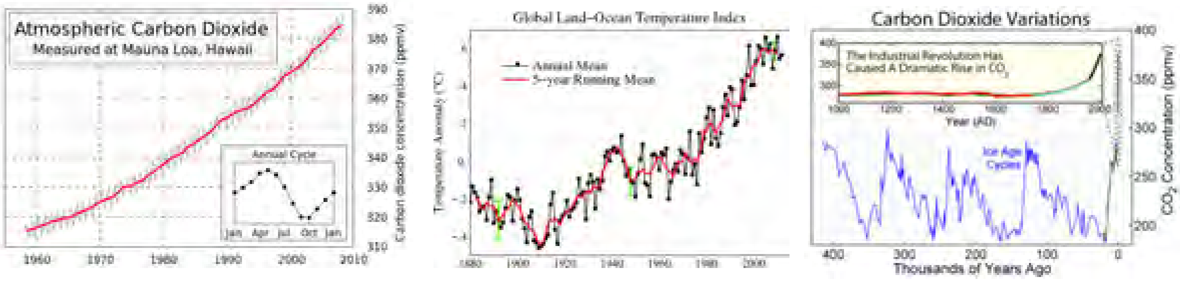

Figure 1 Short-term and long-term behavior of Earth's CO_2 and temperature levels [1-3].

Nevertheless solar cells are the closest of all the renewable energy sources to the ideal concept of extracting energy directly from the Sun, the source driving most of Earth's renewable sources (biofuel, biomass, hydroelectricity, tidal, waves, wind, geothermal and nuclear among others), the use of Sun's power has been very limited because of the high production cost compared to most conventional methods based on fossil fuels (Figure 2). Currently there is one emergent photovoltaic technology that, unlike traditional silicon based cells, do not need expensive nor complicated manufacturing process, its production methods are faster compared to silicon, the used materials can be tailored in order to fit particular absorption ranges or colors and, despite their efficiencies are still lower than Si (Figure 3), can be easily produced in higher amounts using roll to roll printing methods.

Because of these advantages, the "Organic Photovoltaic Cells" (OPVs) or "Organic Solar Cells" as they are commonly known, have strong chances of make possible for the first time the use of photovoltaic energy in the domestic market. Among the current disadvantages of this technology can be mentioned: instability of active materials when exposed to an oxidative atmosphere, lower maximum achievable efficiencies respect Si and low absorption in the infrared (IR) spectral range. All of these disadvantages can be overcome by an adequate design strategy: inverted architectures can be used to improved cell's stability [4], optical design and tandem structures can be used to increase efficiency [5], active molecules and polymers tailoring can modify the absorption of the active materials while tandem cells, using materials with complementary spectra, can help to better exploit the Sun's emission [6].

Each one if these possibilities still needs much further research before providing a definitive solution to each one of these questions, however, since this field of science is currently very active, there is no doubt that, in the near future, new advancements and strategies will bring innovative ways to face each one of these problems.

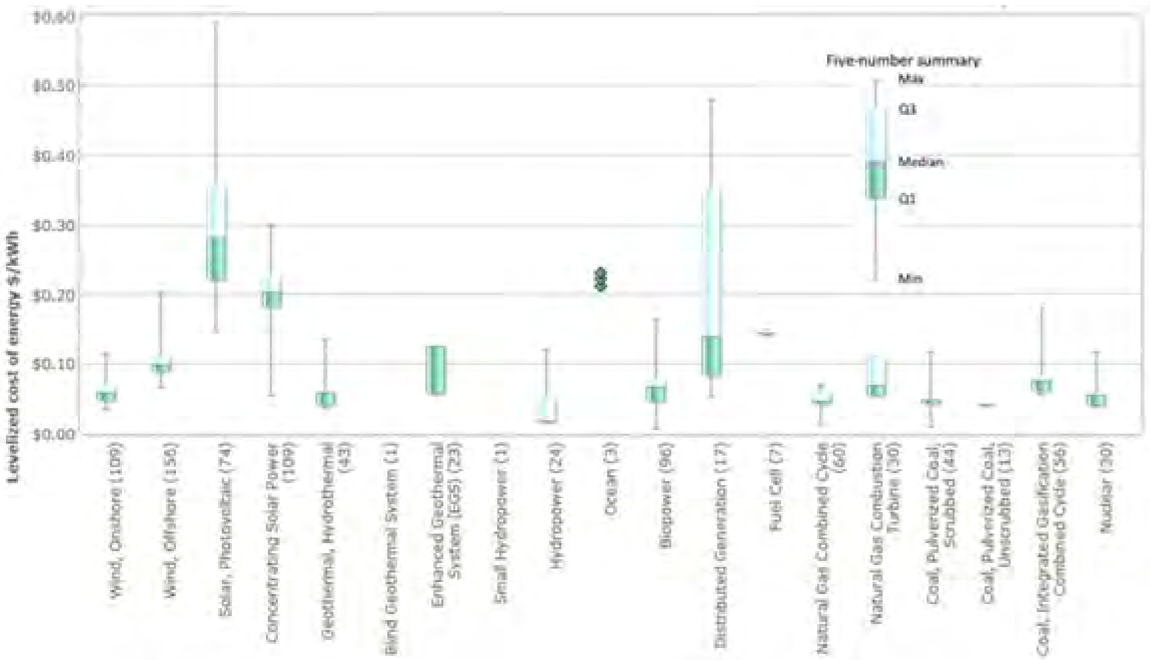

Figure 2 Levelized costs of energy (total costs including capital and yearly operation divided by total energy service production in miles traveled or energy generated) according to data published between 2008 and 2012 [7].

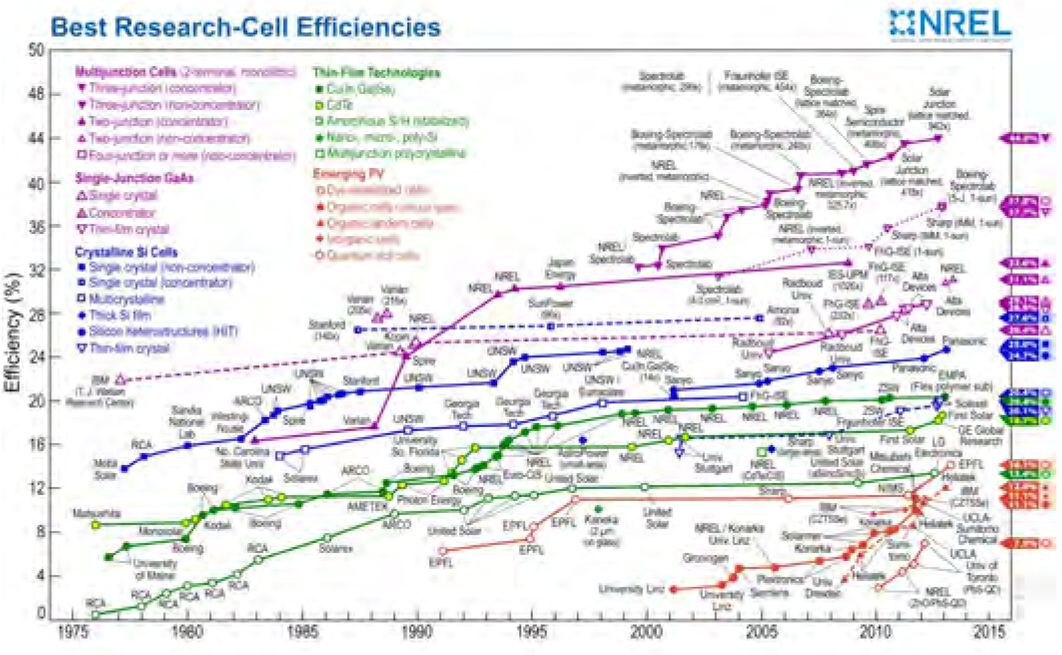

Figure 3 Best solar cell efficiencies reported to date [8].

1.1 Organic solar cells; an overview

The concept of organic solar cell is derived from its inorganic precursors, which traditionally used the interface between two planar n-doped and p-doped silicon films in order to separate the photo-generated electrical charges by using the electric field appearing at the films interface. Nevertheless, the operation of organic devices does not obey exactly the same rules since the dielectric constant of organic materials is much lower compared to inorganic materials (which cause the attractive Coulomb potential well to extend over a greater volume than it does in inorganic semiconductors) and in consequence photo-excited electrons remain loosely bounded to the positive charges (holes) even after being excited, needing another stimulus to completely separate the charges. This stimulus is provided by the electric field appearing at the interface of the two electron-donor and electron-acceptor materials which drives the movement of electrons and holes in opposite directions, breaking the bound and directing them towards different electrodes (Figure 4).

Because the loosely bounded states formed by the electron-hole couples (known as excitons) are not affected by the presence of electric fields since their total electrical charge is zero, the movement towards a donor-acceptor interface will depend only on the random motion of these states. The excitons approaching the interface will separate as was described before while the remaining will recombine, releasing the energy employed to generate the states. In organic materials, the exciton diffusion length is only around 20 nm, which means that only the excitons generated at a distance of 20 nm from the interface will contribute to the electrical current of the cell [9, 10].

For bi-layer cells, similar to the used in inorganic cells (with thicknesses around 100 nm for donor and acceptor film), this means that most of the generated excitons will be lost by recombination. In order to avoid recombination, the organic solar cells make use of what is called “bulk-heterojunction” (BHJ) which consist on the blend of both donor and acceptor materials into a single active film. Since the interfacial area of BHJ is much higher than the area of a planar interface, it ensures most generated excitons are capable to reach an interface and separate into free charges, increasing the electrical current of the cell [11, 12].

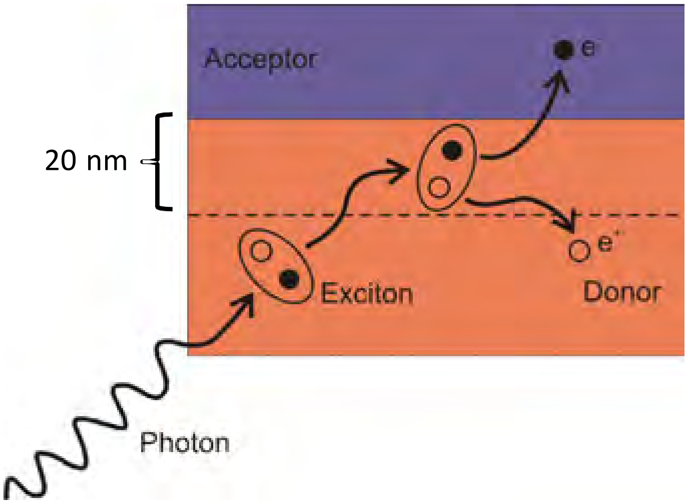

Figure 4 Process of charge generation in an organic solar cell. A photon is absorbed by an electron donor material forming an exciton. If the bounded state is formed within 20 nm of a donor-acceptor interface, the exciton has chances to dissociate into free charges (electrons and holes).

In general, a BHJ-based solar cell consists of several photoactive and charge selective layers that are sandwiched between two conductive electrodes. Optical transparency for at least one electrode is required for harvesting light. Currently, the most commonly used electrodes are mainly based on metal oxides that combine high transparency and low sheet resistance, such as indium tin oxide (ITO), fluorine doped tin oxide (FTO), and aluminum doped zinc oxide (ZnO:Al) [13]. In particular, ITO combines both high optical transparency in the visible range (≈ 82%) and low sheet resistance (10–20 Ω/□, where Ω/square is dimensionally equal to an ohm, but is exclusively used to indicate the sheet resistance of films of uniform thickness) enabling it to be the most commonly used transparent electrode for OPVs.

In amorphous organic materials like the ones used for solar cells, the absence of crystalline structure implies there is no conduction and valence bands like happens with their inorganic counterparts, nevertheless, energetic levels known as LUMO (lowest unoccupied molecular orbital) and HOMO (highest occupied molecular orbital) plays in organic materials a role similar to the conduction and valence bands in inorganic materials respectively. Conductive organic materials exhibit an alternating single bond–double bond structure known as "conjugation" based on sp^2 hybridized carbon atoms that confers the molecule with a high polarizability due to a highly delocalized π-electron system. This enables both the absorption of light on visible wavelengths and electrical charge conductivity.

Important representatives of electron donor semiconducting polymers are: derivatives of phenylene vinylene backbones such as poly[2-methoxy-5-(2-ethylhexyloxy)-1,4-phenyleneinylene] (MEH-PPV), derivatives of thiophene chains such as poly(3-hexylthiophene) (P3HT), derivatives of indacenodithiophene and quinoxaline (PIDT-phanQ) [14] and low bandgap polymer based on alternating units of thieno[3,4-b]thiophene (TT) and benzo[1,2-b:4,5-b']dithiophene (BDT) such as (PBDTTT-C-T) [15]. The polymer systems based on the BDT and TT alternating units are known to be the most successful donor polymers for organic photovoltaics that have shown excellent PCE [16-18]. Polymer solar cells based on the PBDTTT-C-T:$PC_{71}BM$ bulk-heterojunction (BHJ) in both conventional and inverted structures have been demonstrated to achieve power conversion efficiencies (PCEs) as high as 7.6% with relatively constant and efficient spectral response across the whole visible spectrum. The extended absorption produces an excellent neutral color which makes this sort of cells, suitable for window applications. The buckminsterfullerenes C_{60}, C_{70} and its highly soluble derivatives [6,6]-Phenyl C_{61} butyric acid methyl ester ($PC_{61}BM$) and [6,6]-Phenyl C_{71} butyric acid methyl ester ($PC_{71}BM$) are the most widely extended representatives of electron acceptor semiconducting materials used in OPVs cells. Since moisture and oxygen tend to degrade both, donor and acceptor materials, processing under nitrogen or argon atmosphere is a common procedure for the BHJ manufacturing steps.

Lithium fluoride (LiF), Zinc Oxide (ZnO), Calcium (Ca) and the surfactant C_{70}-bis are good examples of materials successfully used in literature as electron transport materials (ETL). On the other hand, Molybdenum oxide (MoO_3), Vanadium oxide (V_2O_5) and poly(3,4-ethylenedioxythiophene) poly(styrenesulfonate) (PEDOT:PSS) are good examples of hole transport materials (HTM). Self-assembled monolayers (SAM) like C_{60}-SAM can be used to enhance the interfacial electronic coupling, providing an easy method to modify the surface energy and the internal series resistance of solar devices (Figure 5).

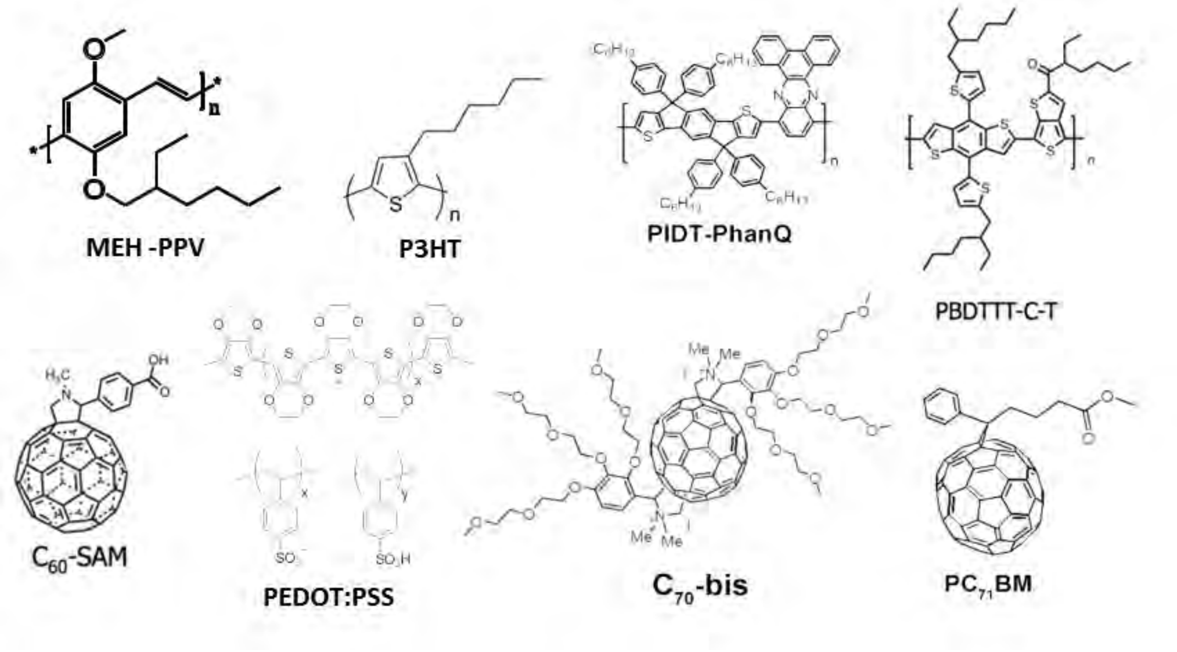

Figure 5 Chemical structures of some of the most representative materials used for organic solar cell manufacturing.

The cell's architecture is determined by the election of electron/hole transport materials and the order in which they are set in the cell. Conventional organic cells are those whose order is comprised as: Substrate/Anode/HTL/BHJ/ETL/Cathode. Currently the highest efficiencies in the field of OPVs are achieved using this architecture; nevertheless this architecture is unstable with a life span of only a few days when exposed to air due to the low work function (and so higher reactivity) of the metals used as cathode and ETL (for example, cathode: Al 4.27 eV, ETL: Ca 2.87 eV, both reacts with H_2 from water and steams and form hydroxides). Another architecture known as "inverted" corresponding to the configuration:

Substrate/Cathode/ETL/BHJ/HTL/Anode is much more stable since metals with a higher work function such as silver (Ag, 4.75 eV, not reactive, found free in nature, oxides decompose with heating) can be used as anode, while PEDOT:PSS or metal oxides like MoO_3 that are stable when exposed to oxygen, can be used as HTL, protecting the BHJ from the harmful influence of air [4, 19].

In order to extract the electrical charges, two carefully chosen HTL and ETL are selected in order to match either the HOMO of the donor material or the LUMO of the acceptor respectively. Cathode and anode are chosen similarly in order to facilitate the extraction from ETL and HTL respectively (Figure 6). Since the solar cell is a system in thermodynamic equilibrium, the alignment of the Fermi levels of all layers originates an electric field which is ultimately responsible of directing electrons and holes towards their corresponding electrode.

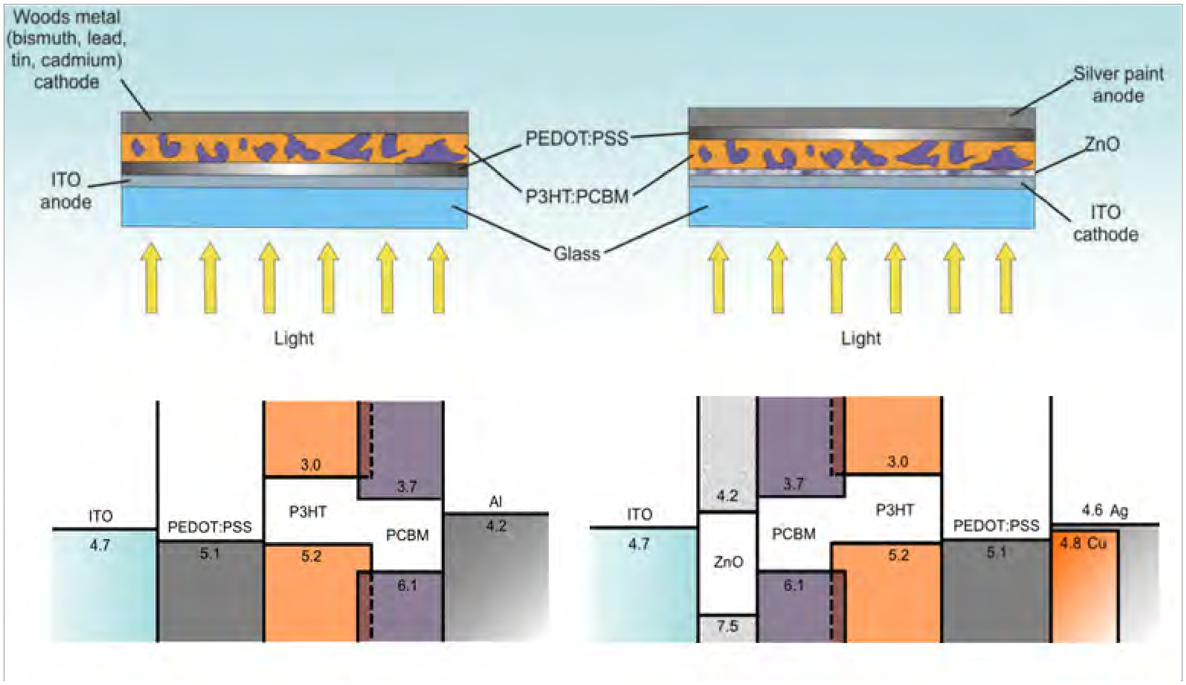

Figure 6 Conventional (left) and inverted (right) architectures of OPV cells employed in this work. Energy level diagrams in eV are shown beneath the corresponding architecture.

1.2 Solar cell characterization

Since there are several kinds of solar cells, an illumination standard that allows comparing among all those types is needed. This standard is called Air Mass 1.5 or AM1.5 and consist on the sun's illumination in a clear day when the ratio between the optical path crossed by the sun's light in the atmosphere and the thickness of the atmosphere at the level of sea is equal to 1.5 [20]. This is achieved when the angle between sun and the zenith is approximately 48°. Experimentally this condition is impractical since it relies on having a clear day with fixed power intensity. In the real life, the testing of solar devices is performed by using solar simulators that replicates the Sun's emission spectrum under the AM1.5 condition using a fixed 100 mW/cm^2 luminous intensity.

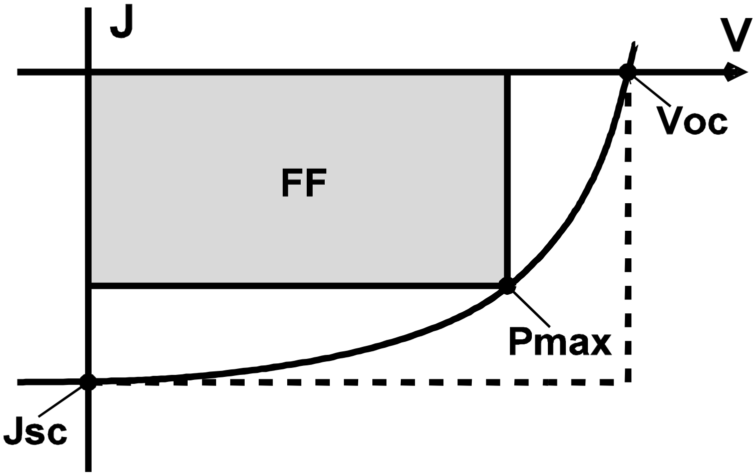

Figure 7 JV graph for a typical solar cell. Geometrically, the Fill Factor (FF) can be visualized as the area ratio of the gray rectangle and the dashed rectangle ($P_{max}/V_{OC}J_{SC}$).

A JV curve from a solar device taken under AM1.5 conditions (Figure 7) provides all the electrical parameters needed to estimate its power conversion efficiency (PCE). Such parameters are listed as follows: open circuit voltage (V_{oc}), short circuit current density (J_{sc}), maximum power voltage (V_{max}), maximum power current density (J_{max}) and fill factor (FF). The V_{oc} is the voltage where the JV curve crosses the horizontal axis ($J = 0$), J_{sc} is the current where the JV curve crosses the vertical axis ($V = 0$), Vmax and Jmax are respectively the voltage and current density of the point whose generated power is maximum among all the JV curve points ($P_{max} = V_{max}\ J_{max}$) and FF is defined as:

$$FF = \frac{V_{max}\,J_{max}}{V_{OC}\,J_{SC}} \tag{1}$$

from which the power conversion efficiency is defined as:

$$PCE = FF\,\frac{V_{OC}\,J_{SC}}{P_{in}} \tag{2}$$

where P_{in} stands for the luminous incident power on the cell (100 mW/cm^2 if following the standard).

1.3 Required properties for ideal materials

To design ideal materials as the donor in polymer-based BHJ solar cells with high PCE, the following issues need to be carefully addressed:

Open circuit voltage (V_{oc})*:* V_{oc} is tightly correlated with the energy level difference between the HOMO of the donor polymer and the LUMO of the acceptor. In theory, polymers with low HOMO levels would exhibit higher V_{oc}. However, the HOMO level of the donor polymer cannot go too low. This is because generally a minimum energy difference of ≈ 0.3 eV between the LUMO energy levels of the donor polymer and the acceptor is required to facilitate efficient exciton splitting and charge dissociation. Continuously lowering the HOMO level of the donor polymer would inevitably enlarge the band gap of the polymer, diminishing the light absorbing ability of the donor polymer (thereby a low J_{sc}).

Short circuit current (J_{sc})*:* The theoretical upper limit for J_{sc} of any excitonic solar cell is decided by the number of excitons created during solar illumination. Ideally, the absorption of the active layer should be compatible with the solar spectrum to maximize the exciton generation. Since $PC_{61}BM$ has a poor absorption in the visible and near-IR region where most of the solar flux is located, the donor polymer has to serve as the main light absorber. Roughly 70% of the sunlight energy is distributed in the wavelength region from 380 to 900 nm [21]; hence, an ideal polymer should have a broad and strong absorption in this range, which requires the polymer band gap to be 1.4−1.5 eV. A narrower band gap polymer could absorb more light, which would increase the J_{sc}; however, continuing to lower the band gap would require an increase of the HOMO level of the donor polymer (since the LUMO level cannot be lower than −3.9 eV with $PC_{61}BM$ as the acceptor for efficient exciton splitting and charge dissociation)[22] and would reduce the V_{oc}. If one assumes a fill factor of 0.65, an external quantum efficiency of 65%, and an optimal morphology, a PCE up to of 10% can be achieved by an ideal polymer with an optimal band gap of 1.5 eV and a HOMO level around −5.4 eV when it is blended with $PC_{61}BM$. Though the experimental V_{oc} can be very close to the predicted value based on the measured HOMO level of the polymer, the actual J_{sc} extracted from a polymer solar cell is usually significantly lower than the theoretical J_{sc} due to a number of loss mechanisms (e.g., monomolecular or bimolecular recombination) during the charge generation, transport, and extraction[21, 23]. Thus a few other desirable features need to be included to mitigate these losses, such as polymers of high molecular weight that allow charges to move through the polymer backbone for longer distances, high charge mobility that facilitates the charge extraction, and optimized active layer morphology that, providing a fine intermixing of both materials, produce larger interfacial areas that helps the exciton separation, and consequently, help to improve the actual J_{sc}.

Fill factor (FF): From a semiconductor photovoltaic device point of view, a high FF requires a small series resistance (R_s) and a large parallel resistance (R_p), both of which are significantly impacted by the morphology of the polymer/fullerene blend. Thus, the morphology of the active layer should be optimized to promote charge separation and favorable transport of photogenerated charges in order to maximize the FF and the attainable J_{sc}.

Finally, besides high PCE, solution processability (offered by side chains) and long-term stability of polymer solar cells (related with both materials and encapsulation) are of equal importance for future application and commercialization. In short, the properties desired for a high performance polymer are (1) good solubility, (2) high molecular weight, (3) HOMO level around −5.4 eV, (4) LUMO level around −3.9 eV, (5) high hole mobility, (6) optimal morphology, and (7) long-term stability.

1.4 Optical optimization

As stratified media which film dimensions are comparable to the wavelength of the visible light, the interference of coherent reflected and transmitted waves at the internal interfaces of an OPV determines the local electromagnetic field in the cell and the charge generation within the BHJ. Traditionally in order to maximize the power extraction, a series of experiments modifying materials and thicknesses need to be carried out in order to find the experimental condition that best enhances the cell's performance, however currently, with the help of computer aided design, the old long labor of experimental optimization can be reduced to a few computational simulations capable to find, sometimes in a matter of minutes, potential experimental conditions for high performance photovoltaic solar cell devices. In order to achieve this goal, a careful analysis of the processes happening within the solar cell is needed. This analysis can be performed in an accurate and elegant way through the use of a transfer matrix method (TMM).

1.4.1 Photocurrent generation model

In order to simulate the solar cell devices developed during this thesis, a series of assumptions were made in order to make the algorithm easier to code and to implement in real world applications. Those assumptions are listed as follows:

1. It is assumed that all interfaces are parallel and flat compared to the wavelength of light.
2. All the materials are considered to be isotropic (something not necessarily true, particularly for the BHJ), so that their linear optical response can be described by a scalar complex index of refraction.
3. The light incident at the device can be described by planar waves.
4. All generated charges contribute to the steady state photocurrent.

Stratified structures with isotropic and homogeneous media and parallel plane interfaces can be described by 2×2 matrices since the equations governing the propagation of the electric field are linear and the tangential component of the electric field is continuous.

1.4.2 Algorithm

The coherent interference of light interacting with the cell is modeled using the methods described in [24, 25]. Let's consider a plane wave incident from left at a multilayer structure having m layers, the light is incident perpendicular to the interfaces. Each layer is referred as j ($j=1,2,\ldots,m$) and has a thickness d_j. The incident light is propagating in the positive direction of the x axis, so the material interfaces are parallel to the yz plane. The waves are resolved in two components corresponding to the resultant total electric field, one component propagating in the positive x direction and one propagating in the negative x direction. These components are denoted as $\boldsymbol{E}_j^+(x)$ and $\boldsymbol{E}_j^-(x)$ respectively. The optical properties of each layer are described by its wavelength dependent complex refractive index $n_j(\lambda) = \eta_j(\lambda) + i\kappa_j(\lambda)$ where η is the real refractive index, κ is the extinction coefficient and λ is the wavelength of light. Variable angle spectroscopic ellipsometry (VASE) was used to acquire the refractive data. The imaginary part κ was additionally corrected using the transmission spectrum of thin films of the materials as reference.

1.4.2.1 Coherent case

According to the transfer matrix formalism, appropriate matrices can be used to describe the interaction of light with matter. In the case of the layered system with the characteristics described before (Figure 8), two kinds of matrices, one to describe the interfaces (refraction matrix) and one to describe the propagation through the layer are all what is needed to simulate the light's behavior within a layered media.

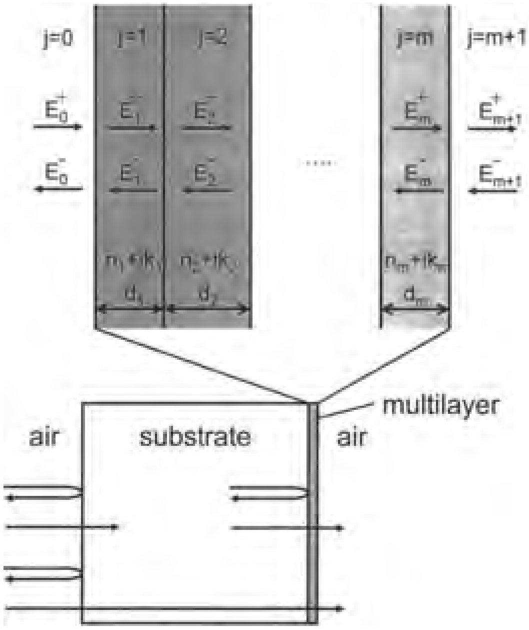

Figure 8 Geometry of the multilayer stack used in the optical electric field simulation.

Let's call the interface between the layer j and $j+1$, interface $j(j+1)$. Then the reflection and transmission at this interface will be characterized by the complex Fresnel reflection and transmission coefficients $r_{j(j+1)}$ and $t_{j(j+1)}$ respectively. The matrix describing the refraction at this interface can be written as:

$$I_{j(j+1)} = \frac{1}{t_{j(j+1)}} \begin{pmatrix} 1 & r_{j(j+1)} \\ r_{j(j+1)} & 1 \end{pmatrix} \quad (3)$$

while the matrix describing the propagation through layer j is expressed as:

$$L_j = \begin{pmatrix} e^{-i\xi_j d_j} & 0 \\ 0 & e^{-i\xi_j d_j} \end{pmatrix} \tag{4}$$

where $\xi_j = \frac{2\pi}{\lambda} n_j$ and $\xi_j d_j$ is the phase change the wave experiences as it traverses layer j. For a plane wave propagating along the surface normal in adjacent layers j and $j+1$, the complex Fresnel reflection and transmission coefficients are expressed as: $r_{j(j+1)} = \frac{n_j - n_{j+1}}{n_j + n_{j+1}}$ and $t_{j(j+1)} = \frac{2n_j}{n_j + n_{j+1}}$ respectively. Following this rules, the field amplitudes on the left-hand side of the $j(j+1)$ interface are related with the corresponding field amplitudes on the right-hand side as:

$$\begin{pmatrix} \boldsymbol{E}_j^+\left(x_{j(j+1)}\right) \\ \boldsymbol{E}_j^-\left(x_{j(j+1)}\right) \end{pmatrix} = I_{j(j+1)} \begin{pmatrix} \boldsymbol{E}_k^+\left(x_{j(j+1)}\right) \\ \boldsymbol{E}_k^-\left(x_{j(j+1)}\right) \end{pmatrix} \tag{5}$$

while the field amplitudes on the left-hand side of layer j are related with the corresponding field amplitudes on the right-hand side of layer j as:

$$\begin{pmatrix} \boldsymbol{E}_j^+\left(x_{(j-1)j}\right) \\ \boldsymbol{E}_j^-\left(x_{(j-1)j}\right) \end{pmatrix} = L_j \begin{pmatrix} \boldsymbol{E}_j^+\left(x_{j(j+1)}\right) \\ \boldsymbol{E}_j^-\left(x_{j(j+1)}\right) \end{pmatrix} \tag{6}$$

In this way, the electric fields in the two outermost layers $j = 0$ and $j = m + 1$ are related via the transfer matrix S in the form:

$$\begin{pmatrix} \boldsymbol{E}_0^+(x_{01}) \\ \boldsymbol{E}_0^-(x_{01}) \end{pmatrix} = S \begin{pmatrix} \boldsymbol{E}_{m+1}^+\left(x_{m(m+1)}\right) \\ \boldsymbol{E}_{m+1}^-\left(x_{m(m+1)}\right) \end{pmatrix} \tag{7}$$

where

$$S = \begin{pmatrix} S_{11} & S_{12} \\ S_{21} & S_{22} \end{pmatrix} = \left(\prod_{v=1}^{m} I_{(v-1)v} L_v \right) \cdot I_{m(m+1)} \tag{8}$$

The complex reflection and transmission coefficients for the multilayer can be conveniently expressed using the terms of this matrix as:

$$\mathrm{r} = \mathrm{r}_{0(\mathrm{m}+1)} = \frac{\mathbf{E}_0^-}{\mathbf{E}_0^+} = \frac{\mathrm{S}_{21}}{\mathrm{S}_{11}} \tag{9}$$

$$\mathrm{t} = \mathrm{t}_{0(\mathrm{m}+1)} = \frac{\mathbf{E}_{\mathrm{m}+1}^+}{\mathbf{E}_0^+} = \frac{1}{\mathrm{S}_{11}} \tag{10}$$

$$\mathrm{r}' = \mathrm{r}_{(\mathrm{m}+1)0} = \frac{\mathbf{E}_{\mathrm{m}+1}^-}{\mathbf{E}_{\mathrm{m}+1}^+} = -\frac{\mathrm{S}_{12}}{\mathrm{S}_{11}} \tag{11}$$

and

$$\mathrm{t}' = \mathrm{t}_{(\mathrm{m}+1)0} = \frac{\mathbf{E}_0^-}{\mathbf{E}_{\mathrm{m}+1}^+} = \frac{\mathrm{S}_{11}\mathrm{S}_{22} - \mathrm{S}_{12}\mathrm{S}_{21}}{\mathrm{S}_{11}} \tag{12}$$

where r and r' are the front and back complex reflection coefficients and *t* and *t'* are the complex transmission coefficients. The reflectance and transmittance coefficients are obtained as a square of the magnitudes of *r*, *r'*, *t* and *t'*. Since equations (9)-(12) relate the *S* elements to the complex reflection ad transmission coefficients, the *S* matrix can be written in terms of the amplitude coefficients as

$$S = \begin{pmatrix} S_{11} & S_{12} \\ S_{21} & S_{22} \end{pmatrix} = \frac{1}{t_{0(m+1)}} \begin{pmatrix} 1 & -r_{(m+1)0} \\ r_{0(m+1)} & t_{0(m+1)}t_{(m+1)0} - r_{0(m+1)}r_{(m+1)0} \end{pmatrix} \tag{13}$$

Unlike other optical systems where only the total transmitted or reflected light is worth to calculate, in a solar cell, it is only worth to calculate the intensity within the BHJ. In order to calculate the internal electric field in layer j, the layer system can be divided into two subsets separated by layer j, which means the total system transfer matrix will be written as

$$S = S_j' L_j S_j'' \tag{14}$$

where the partial system transfer matrices S_j' and S_j'' are defined as:

$$S_j' = \begin{pmatrix} S_{j11}' & S_{j12}' \\ S_{j21}' & S_{j22}' \end{pmatrix} = \left(\prod_{v=1}^{j-1} I_{(v-1)v} L_v \right) \cdot I_{(j-1)j} \tag{15}$$

and

$$S_j'' = \begin{pmatrix} S_{j11}'' & S_{j12}'' \\ S_{j21}'' & S_{j22}'' \end{pmatrix} = \left(\prod_{v=j+1}^{m} I_{(v-1)v} L_v \right) \cdot I_{m(m+1)} \tag{16}$$

relating the electric fields in the boundaries $(j-1)j$ and $j(j+1)$ with the outermost electric fields in the manner

$$\begin{pmatrix} \boldsymbol{E}_0^+(x_{01}) \\ \boldsymbol{E}_0^-(x_{01}) \end{pmatrix} = S_j' \begin{pmatrix} \boldsymbol{E}_j^+\left(x_{(j-1)j}\right) \\ \boldsymbol{E}_j^-\left(x_{(j-1)j}\right) \end{pmatrix} \tag{17}$$

and

$$\begin{pmatrix} \boldsymbol{E}_j^+\left(x_{j(j+1)}\right) \\ \boldsymbol{E}_j^-\left(x_{j(j+1)}\right) \end{pmatrix} = S_j'' \begin{pmatrix} \boldsymbol{E}_{m+1}^+\left(x_{m(m+1)}\right) \\ \boldsymbol{E}_{m+1}^-\left(x_{m(m+1)}\right) \end{pmatrix} \tag{18}$$

Considering that at the last medium $m+1$ there is no contra-propagating term since there are no boundaries that could cause reflection we can assume $\boldsymbol{E}_{m+1}^-\left(x_{m(m+1)}\right) = \mathbf{0}$, then using (7) and (14)

$$\begin{pmatrix} \boldsymbol{E}_0^+(x_{01}) \\ \boldsymbol{E}_0^-(x_{01}) \end{pmatrix} = S_j' L_j S_j'' \begin{pmatrix} \boldsymbol{E}_{m+1}^+\left(x_{m(m+1)}\right) \\ 0 \end{pmatrix} \tag{19}$$

Performing the matrix products and solving for $\boldsymbol{E}_{m+1}^+\left(x_{m(m+1)}\right)$ we get

$$\boldsymbol{E}_{m+1}^+\left(x_{m(m+1)}\right) = \frac{\boldsymbol{E}_0^+(x_{01})}{S_{j11}' S_{j11}'' e^{-i\xi_j d_j} + S_{j12}' S_{j21}'' e^{i\xi_j d_j}} \tag{20}$$

The electric field at the $(j-1)j$ interface can then be calculated by

$$\begin{pmatrix} \boldsymbol{E}_j^+\left(x_{(j-1)j}\right) \\ \boldsymbol{E}_j^-\left(x_{(j-1)j}\right) \end{pmatrix} = L_j S_j'' \begin{pmatrix} \boldsymbol{E}_{m+1}^+\left(x_{m(m+1)}\right) \\ 0 \end{pmatrix} \tag{21}$$

performing the matrix products, using the value calculated at (20) and rearranging terms we get the expression:

$$\frac{\boldsymbol{E}_j^+\left(x_{(j-1)j}\right)}{\boldsymbol{E}_0^+(x_{01})} = t_j^+ = \frac{\frac{1}{S_{j11}'}}{1 + \frac{S_{j12}' S_{j21}''}{S_{j11}' S_{j11}''} e^{2i\xi_j d_j}} \tag{22}$$

which describes the electric field propagating in the positive direction in layer j at the left interface. In the same way, an expression describing the electric field propagating in the negative direction at the interface $(j-1)j$ can be derived following a similar procedure getting

$$t_j^- = t_j^+ \frac{S_{j21}''}{S_{j11}''} e^{i2\xi_j d_j} \tag{23}$$

With this, the total electric field in an arbitrary position in layer j at a distance h from the left boundary $(j-1)j$ in terms of the incident plane wave is given by

$$\boldsymbol{E}_j(h) = \boldsymbol{E}_j^+(h) + \boldsymbol{E}_j^-(h) = \left(t_j^+ e^{i\xi_j h} + t_j^- e^{-i\xi_j h}\right) \boldsymbol{E}_0^+(x_{01}) \tag{24}$$

1.4.2.2 Introduction of incoherence

Every single solar cell developed in this thesis was manufactured on a thick substrate, either glass or polyethylene naphthalate (PEN). The thicknesses of these substrates are usually so thick that coherent interference can no longer be used to describe their behavior. For this reason, an incoherent treatment using modified intensity matrices instead of complex amplitude matrices similar to the method described in [26] was employed to simulate the substrate. In order to calculate the electric field, first the system transfer matrix of the coherent multilayer is calculated. The complex-amplitude reflection and transmission coefficients are evaluated from this transfer matrix. When these coefficients are replaced with their square amplitudes, the modified intensity matrix becomes

$$S^{Int} = \frac{1}{\left|t_{0(m+1)}\right|^2} \begin{pmatrix} 1 & -\left|r_{(m+1)0}\right|^2 \\ \left|r_{0(m+1)}\right|^2 & \left|t_{0(m+1)}t_{(m+1)0}\right|^2 - \left|r_{0(m+1)}r_{(m+1)0}\right|^2 \end{pmatrix} \quad (25)$$

And directly yields the reflectance and transmittance of the coherent multilayer rather than complex reflection and transmission coefficients. This modified intensity matrix is multiplied with a modified intensity propagation matrix L_{subst}^{Int} for the incoherent substrate and a refraction intensity matrix S_{face}^{Int} representing the external face of the substrate. This refraction matrix (S_{face}^{Int}) is calculated using the same coherent procedure used for the multilayer (but for only one interface) and then the squares of the terms are obtained. The intensity matrix of the whole system is then expressed as

$$\begin{aligned} S^{Incoh} &= S_{face}^{Int} L_{substrate}^{Int} S^{Int} \\ &= S_{face}^{Int} \begin{pmatrix} \left|e^{\frac{-i2\pi n_{subst} d_{subst}}{\lambda}}\right|^2 & 0 \\ 0 & \left|e^{\frac{i2\pi n_{subst} d_{subst}}{\lambda}}\right|^2 \end{pmatrix} S^{Int} \end{aligned} \quad (26)$$

Then the reflectance and transmittance of the whole system are obtained in terms of the elements of this matrix as:

$$R^{Incoh} = \frac{S_{21}^{Incoh}}{S_{11}^{Incoh}} \quad (27)$$

and

$$T^{Incoh} = \frac{1}{S_{11}^{Incoh}} \quad (28)$$

In order to get the local electric field within the device considering both, multilayer and substrate, the effect of the substrate is calculated using

$$S_{subst}^{Incoh} = S_{face}^{Int} L_{substrate}^{Int} \tag{29}$$

from which the transmitted light through the substrate can be calculated using the corresponding term as

$$T_{subst}^{Incoh} = \frac{1}{S_{subst\,11}^{Incoh}} \frac{\eta_{subst}}{\eta_{air}} \tag{30}$$

Finally the electric field intensity within layer *j* at position *h* is calculated using the squared magnitude of the electric field obtained in (24) corrected with the transmittance of the substrate. Considering an incident light intensity I_0 (in our case, the intensity of the AM1.5 spectrum at wavelength λ), the intensity within the active layer is:

$$I_j(h) = \frac{\eta_j}{\eta_{subst}} T_{subst}^{Incoh} \left| \boldsymbol{E}_j(h) \right|^2 I_0 \tag{31}$$

The time averaged energy dissipated as a function of position is then given by:

$$Q_j(h) = \frac{2\pi c \varepsilon_0 \eta_j \kappa_j}{\lambda} I_j(h) \tag{32}$$

where c is the speed of light, ε_0 is the permittivity of free space and λ is the wavelength of light. If an internal quantum efficiency (IQE) of 100% is considered, every single absorbed photon will generate a pair hole-exciton. Since the energy of one photon is given by

$$E = \frac{hc}{\lambda} \tag{33}$$

dividing $Q_j(h)$ by this factor an integrating it over the whole active layer will lend us the total number of photogenerated charges, in other words, the contribution to the electrical current of photons of wavelength λ or, $EQE_{100\%}(\lambda)$, where EQE stands for external quantum efficiency. The same procedure can be followed for all the significant wavelengths in order to calculate the total short circuit electrical current of the cell ($J_{sc-100\%}$). In real world devices the IQE will most likely differ from 100%. By experimentally determining the external quantum efficiency, the real internal quantum efficiency of the cell can be calculated as:

$$IQE = \frac{EQE}{EQE_{100\%}} \tag{34}$$

1.4.2.3 Refractive index correction

Nevertheless the refractive index data used for this thesis was determined by VASE, strong deviations between the calculated and the experimental behavior of devices are observed when using directly this data for the simulation. This mainly happens because VASE measures the change in polarization of light when it interacts with a material of interest, obtaining an amplitude ratio and a phase difference as parameters. The refractive index is then obtained fitting the VASE data using adequate dispersion models. Since a good fitting is not always possible even combining several dispersion models, the refractive index data obtained by VASE is not always accurate. For this reason it is a common practice to correct the experimental data using the UV/VIS spectrum of a thin film and the Beer-Lambert law.

$$T = \frac{I}{I_0} = e^{-\alpha l N} \tag{35}$$

As it is concluded from optical analysis, the transmittance of a multilayer depends on the materials and thicknesses used to make the multilayer. Under particular conditions it is even possible to increase the transmission of a layered system by adding more films. The Beer-Lambert law (35) is unable to explain that increase in transmittance since it cannot account for internal interference on the films, so, it can't be used to correct the refractive index as it is incorrectly done in most literature.

A more adequate method to correct the refractive index data was designed for this thesis taking advantage of the transfer matrix simulation. That method is described as follows:

1. Make a single film sample on a substrate of known complex refractive index.
2. Using VASE, find the refractive index data of the sample.
3. Take the transmission spectrum (T_{exp}) of the whole system (glass/film); this implies the use of air as reference when measuring the spectrum.
4. Measure the thickness of the film d using Atomic Force Microscopy (AFM).
5. Using the film thickness and the refractive index data obtained by VASE, calculate the simulated transmission spectrum (T_{sim}) of the whole system (glass/film).
6. Calculate $\Delta T = T_{exp} - T_{sim}$
7. Correct the refractive index data according to the rule:
$$n = n - i\frac{\lambda}{4\pi d}\Delta T \qquad (36)$$
8. Repeat steps 5 to 7 until $\Delta T \leq \epsilon$, where ϵ is a minimal acceptable difference between experimental and simulated data chosen by the user.

Since the calculation of total transmittance loses all information regarding phase when taking absolute values $|E|^2$, it is not possible to analytically express, in terms of the real amount ΔT, the correction required by the real and imaginary parts η and κ in order to make $T_{exp} = T_{sim}$. In our case, as can be concluded from (36), we chose to correct only the extinction coefficient κ since it is the main factor modeling the shape of T. On the other hand, little changes on η do not produce big effects on T, so, even values slightly incorrect of η, taken directly from VASE, will provide a good enough first approach for modeling purposes [27]. The factor $\frac{\lambda}{4\pi d}$ was semi-empirically found to provide good results within 10 iteration steps.

This adjustment technique proved to be particularly useful for OPV optimization since, while technically keeping the same manufacturing conditions, the absorption spectrum of each BHJ solution, prepared in this study, presented an slightly different transmission spectrum, apparently related to small variations in the concentration of donor and acceptor materials. Since these variations were beyond our control, and because using VASE to measure the refractive index of every single experimental batch was too complicated, we opted for measuring the refractive index of our materials using VASE only once and then, correct the data for every batch using an easy to measure UV/VIS spectrum. This way we could quickly modify our data and adapt the simulator to the real experimental conditions.

For some materials we found that a good fitting using the VASE data was extremely difficult. In the particular case of metals, the preparation conditions (deposition rate, thickness, substrate temperature) strongly modify the final optical behavior of films. When refractive index data was already available in literature, this correction method allowed us to adapt the published data to represent our materials, getting results that closely match the experimental device behavior.

1.5 Color analysis

For the case of semitransparent solar cells, the color of the cells was analyzed using the CIE 1931 and the CIE 1960 UCS color spaces.

1.5.1 CIE 1931

In base on the works of William David Wright and John Guild [28, 29], the International Commission of Illumination (CIE) defined the specification for the CIE XYZ space. In this specification the human observer is characterized by color matching functions $\bar{x}(\lambda)$, $\bar{y}(\lambda)$ and $\bar{z}(\lambda)$ which are numerical descriptions of the human average chromatic response within 2° arc of the fovea. These curves represent spectral sensitivity curves of three linear light detectors yielding the CIE tristimulus values X, Y and Z. For a spectral power distribution $I(\lambda)$, the tristimulus values are given in terms of the color matching functions by:

$$X = \int_{380\text{ nm}}^{780\text{ nm}} I(\lambda)\bar{x}(\lambda)d\lambda \tag{37}$$

$$Y = \int_{380\text{ nm}}^{780\text{ nm}} I(\lambda)\bar{y}(\lambda)d\lambda \tag{38}$$

$$Z = \int_{380\text{ nm}}^{780\text{ nm}} I(\lambda)\bar{z}(\lambda)d\lambda \tag{39}$$

The Y value has been deliberately design by CIE to represent the brightness or luminance of $I(\lambda)$. Let's note that the concept of color can be divided into two elements: chromaticity and brightness. As an example, the color gray can be obtained as a reduced in brightness version of white. In this way, white and gray share the same chromaticity but differs in brightness. The tristimulus values XYZ are capable to represent both features of color in a tridimensional space; nevertheless in order to facilitate representation, another color space is defined in terms of XYZ as:

$$x = \frac{X}{X+Y+Z} \tag{40}$$

$$y = \frac{Y}{X+Y+Z} \tag{41}$$

$$z = \frac{Z}{X+Y+Z} \tag{42}$$

Since x, y and z are normalized, the value of z can be obtain in terms of x and y as

$$z = 1 - x - y \tag{43}$$

which means only x and y provide meaningful chromatic information. The color space CIE xyY is then defined using x and y to represent the chromaticity while using Y to represent the luminosity of the power distribution $I(\lambda)$.

1.5.2 CIE 1960 Uniform Color Space (UCS)

Nevertheless the CIE 1931 is the most widely used color space, it is not suitable for color comparison. The uniform color space CIE 1960 UCS is a projective transformation of the CIE XYZ color space that allows comparing visual differences, since in such a space equal color differences corresponds to equal perceptual changes in color, in other words, distance between two points in this space describes the change in color between them. Today it is mostly used to calculate correlated color temperature (CCT) that is the temperature of the Planckian radiator whose perceived color most closely resembles that of a given stimulus at the same brightness and under specific viewing conditions. The u,v coordinates from the UCS color space are related to the coordinates of the xyY space according to the rules:

$$x = \frac{3u}{2u - 8v + 4} \tag{44}$$

$$y = \frac{2v}{2u - 8v + 4} \tag{45}$$

1.5.3 Planckian Locus

The Plankian locus is defined as the path that the color of an incandescent blackbody takes in a particular color space as the blackbody temperature changes. Since in the UCS space isotherm curves are perpendicular to the Planckian locus and the metric is uniform (something not happening in the xyY space), determining the correlated color temperature in the UCS space is equivalent to find the closest point in the Planckian locus to the u, v coordinates representing our power distribution $I(\lambda)$.

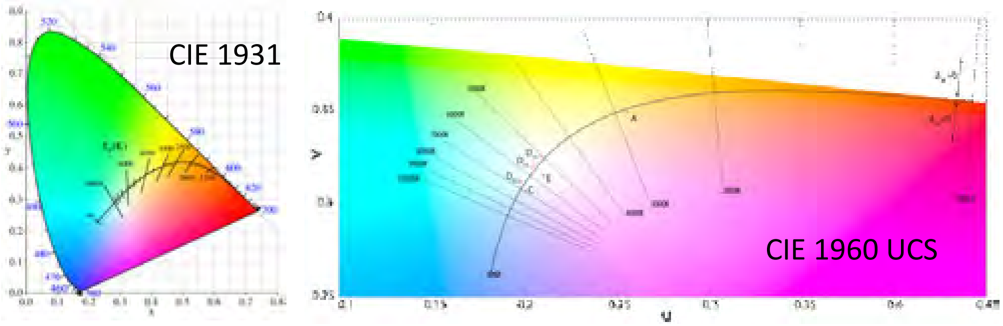

Figure 9 The Planckian locus on the CIE 1931 and CIE 1960 UCS color space showing the isotherms.

1.5.4 Color rendering

Color rendering is defined by CIE as the effect of an illuminant on the color appearance of objects by conscious or subconscious comparison with their color appearance under a reference illuminant. In simple words, it means that for a human observer the apparent color of objects depends on the kind of light used to illuminate it. The human vision system is capable to correct for color deviations caused by varying illumination conditions. This ability is known as color constancy [30]. Experimentally it has been determined that the different chromaticities associated to the phases of daylight are close to that of blackbody radiators in the range 4000 to 25000 K [31]. Because the color constancy of our vision system is known to be excellent, blackbody radiators (Planckian Locus) are referred in colorimetry as light sources of perfect color rendering capacities.

In order to make the value meaningful, the color temperature of a light source can only be defined for test sources differing less than $\Delta_{uv} = 0.05$ from the Planckian locus, in other words, for illuminants that are approximately white. A quantitative amount called Color Rendering Index (CRI) was defined in order to allow estimating the quality of an illuminant. The CRI is calculated comparing the color associated in the UCS color space to 8 standard color samples (TCS01-08) evenly distributed over the complete range of hues when they are illuminated by a probing light $I(\lambda)$, and a reference white light source with the same correlated color temperature as the probing light (the closest point in the Planckian Locus), using the test sample method (TSM) [32]. The method involves chromatically adapting the (u, v) coordinates through the use of a von Kries transform in order to get the corresponding adapted coordinates (u_c, v_c). Let's say (u_t, v_t), (u_r, v_r) and $(u_{t,i}, v_{t,i})$ are the coordinates in the CIE 1960 UCS space of the test light, the reference white light (closest point in Planckian locus) and the reflected light of the color sample *i* illuminated by the test light (inner product of test light and color sample *TCS0i*), then the von Kries transform of the color sample *i* under our test light is calculated as follows:

$$c = \frac{4.0 - u - 10.0v}{v} \tag{46}$$

$$d = \frac{1.708v - 1.481u + 0.404}{v} \tag{47}$$

$$u_{c,i} = \frac{10.872 + 0.404\left(\frac{c_r}{c_t}\right)c_{t,i} - 4\left(\frac{d_r}{d_t}\right)d_{t,i}}{16.518 + 1.481\left(\frac{c_r}{c_t}\right)c_{t,i} - \left(\frac{d_r}{d_t}\right)d_{t,i}} \tag{48}$$

$$v_{c,i} = \frac{5.520}{16.518 + 1.481\left(\frac{c_r}{c_t}\right)c_{t,i} - \left(\frac{d_r}{d_t}\right)d_{t,i}} \tag{49}$$

Where c_r, d_r; c_t, d_t and $c_{t,i}$, $d_{t,i}$ are the values obtained using (46)-(47) for (u_r, v_r); (u_t, v_t) and $(u_{t,i}, v_{t,i})$ respectively. With this, the test color method is defined as follows:

1. Using the 2° standard observer, the chromaticity coordinates of the test source in the CIE 1960 UCS color space is found.
2. The CCT of the test source is determined by finding the closest point to the Planckian locus on the (u, v) chromaticity diagram.
3. If the test source has a CCT $<$ 5000 K, a blackbody with the same CCT is used for reference, otherwise the CIE standard illuminant D with the same CCT is used (see definition below).
4. Measure the chromaticity distance of the test source to the Planckian Locus in the CIE 1960 UCS color space. The calculation will only be meaningful if the distance is under 5.4×10^{-3}. The distance between two p and q points is calculated by:

$$\Delta_{u,v} = \sqrt{\left(u_p - u_q\right)^2 + \left(v_p - v_q\right)^2} \tag{50}$$

5. Illuminate the test samples TCS01-08 using alternately both sources.
6. Using the 2° standard observer, find the coordinates of the light reflected by each sample in the CIE 1964 color space.
7. Chromatically adapt each sample by using the von Kries transform.
8. For the eight color samples, calculate the distance ΔD_i between the coordinates produced by the reference and the test source using (50).
9. The special CRI is calculated using the formula: $R_i = 100 - 4.6\Delta D_i$.
10. The general CRI (R_a) is found by calculating the arithmetic mean of the special CRIs.

The mean of the special CRIs is called the general CRI, which represents the color rendering capacity of the sample. By definition, the special and the general CRI can range only from 0 to 100, where a higher general CRI represents a better color rendering capacity. The blackbody radiation corresponding to a correlated color temperature T can be calculated by the Planck's law:

$$I(\lambda, T) = \frac{2\pi hc^2}{\lambda^5} \frac{1}{e^{\frac{hc}{\lambda kT}} - 1} \tag{51}$$

where I is the blackbody spectral radiance, h is the Planck constant, c is the speed of ligth and k is the Boltzmann's constant.

The D series of illuminants are mathematical constructions intended to represent daylight [33]. The spectral power distribution of the D series of illuminants can be approximated by the linear combination of three fixed spectral power distributions called $S_0(\lambda)$, $S_1(\lambda)$ and $S_2(\lambda)$ [34, 35]. Derived in terms of its chromaticities coordinates in the CIE 1931 color space (x_D, y_D), a D illuminant of temperature T can be expressed as follows:

$$x_D = \begin{cases} 0.244063 + 0.09911 \frac{10^3}{T} + 2.9678 \frac{10^6}{T^2} - 4.6070 \frac{10^9}{T^3}, 4000K \leq T \leq 7000K \\ 0.237040 + 0.24748 \frac{10^3}{T} + 1.9018 \frac{10^6}{T^2} - 2.0064 \frac{10^9}{T^3}, 7000K < T \leq 25000K \end{cases} \tag{52}$$

$$y_D = -3.000x_D^2 + 2.870x_D - 0.275 \tag{53}$$

$$M = 0.0241 + 0.2562x_D - 0.7341y_D \tag{54}$$

$$M_1 = \frac{1}{M}(-1.3515 - 1.7703x_D + 5.9114y_D) \tag{55}$$

$$M_2 = \frac{1}{M}(0.03000 - 31.4424x_D + 30.0717y_D) \tag{56}$$

$$I_D(\lambda) = S_0(\lambda) + M_1S_1(\lambda) + M_2S_2(\lambda) \tag{57}$$

1.6 JV curve fitting

The degradation of the electrodes in respect to bending can be associated to changes in the sheet resistance, usually related to cracks in the conductive films. In order to determine the effect of the bending over the internal resistances of the flexible devices developed during this thesis, for each one of their JV curves, a corresponding ideality factor (n) and series and parallel resistances (R_s and R_p respectively) were extracted, fitting the JV curves, according to the single diode model described by:

$$J = J_0\left(e^{\frac{q(V-R_sJ)}{nkT}} - 1\right) + \frac{V - R_sJ}{R_p} - J_{ph} \tag{58}$$

using an extraction method based on the Lambert W function. Here q is the charge of the electron, k is the Boltzmann constant, T is the temperature (fixed to room temperature $T = 296\ K$), J_{ph} is the photocurrent and J_0 is the saturation current.

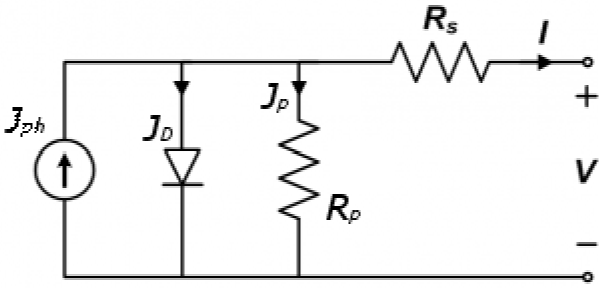

Figure 10 Single diode model.

2. | Results and discussion

During this thesis, several approaches were attempted in order to improve the performance of the solar devices. The results will be discussed in separated sections since each approach attempts to solve a different problem of the OPV technology. Each section presents an appropriate background in order to introduce the reader to the particular problem to address. The topics will be described in chronological order so the progress in the experimental results can be appreciated. The main research projects addressed during the doctoral work are discussed in different sections of this chapter. The main topic of each research project (and so, the main topic of each section), can be described as follows:

2.1 Development of functional OPVs using the technology available in CIO. In this case the results refers only to solar cells, in conventional architecture, prepared without HTL or ETL and using Wood's metal as cathode to test the photovoltaic properties of the boronates M1 and M2 synthesized within the workgroup.

2.2 Development of devices in both conventional and inverted architecture. HTL and ETL were introduced for the first time in the thesis. PEDOT:PSS was used as HTL in both architectures while ZnO was used as ETL, specifically for the inverted architecture. Since the inverted architecture is known to be stable when exposed to oxygen and moisture, it was introduced in an attempt to increase our efficiencies and fill factor for cells produced at ambient conditions.

2.3 This section refers to the main project developed during the research stay at Jen Group at the University of Washington. In this project, a transfer matrix software was developed in order to optically optimize the solar cell performance. The software was applied to the design of a micro-cavity based device of superior performance using a polymer developed within Jen Group (PIDT-PhanQ). The cell's design makes use of two Ag electrodes one of which is thin enough to behave as a semitransparent electrode. The cells were developed in a nitrogen atmosphere, taking advantage of the wide experience of the group.

2.4 Since the optical simulator had wide applications for the design of solar devices, this section explains how the simulator was used to evaluate the quality of semitransparent solar cell devices by optimizing and analyzing the color properties of cells using the polymer PIDT-PhanQ. This project was also developed at University of Washington. My main contribution to this project was the theoretical analysis and optical optimization of the devices.

2.5 A detailed color analysis based on color rendering indexes was performed on an inverted system of promising properties (PBDTTT-C-T). This project was also developed at the University of Washington. In this project, my main contribution is the theoretical analysis, optical optimization and color evaluation. The cells developed presented the highest color rendering indexes ever reported in semitransparent organic solar cell devices.

2.1 Fabrication of solar cells based on MEH-PPV:$PC_{61}BM$ by a vacuum free method [36]

Since many laboratories that possess expertise in synthesis of organic materials may not always have solar cell fabrication and testing capabilities, simple in-house methods for device testing are desirable for fast and easy evaluation of new materials [37, 38]. In this study, we proposed the use of Woods metal, which is an eutectic alloy of Pb/Bi/Cd/Sn (25 %, 50 %, 12.5 % and 12.5 % respectively) that can be applied by a vacuum free method, as a convenient substitute for evaporated aluminum. The melting point of Woods metal (75 °C), enables the alloy to be applied by an inexpensive method without a vacuum chamber. Although the work function of this eutectic alloy is not known, the work functions of the components (Pb: 4.25 eV, Bi: 4.34 eV, Cd: 4.08 eV, and Sn: 4.42 eV) could suggest smaller work function than that of the anode (ITO): 4.7 eV and so, relatively close to the acceptor LUMO (in this work $PC_{61}BM$: 3.7 eV).

Aluminum is the most common material used in OPVs cells because its work function of 4.3 eV is adequate for extracting electrons from fullerene derivatives. There are very few alternatives to metal evaporation, one of which is the use of mercury electrodes. Mercury is however highly undesirable because of its high toxicity and its work function of 4.5 eV, very close to that of ITO [38]. A second alternative is to test materials in liquid electrolyte, which can introduce other effects such as hysteresis. Other alternatives are the use of Ga-In eutectic alloy, a material whose melt point is 15.7 °C [38, 39].

Two new molecules 6-nitro-3-(E)-3-(4-dimethylaminophenyl)allylidene)-2,3-dihydrobenzo[d]-[1,3,2]-oxazaborole (M1), and (E)-3-(4-dimethylaminophenyl)allylidene)-2,3-dihydrobenzo[d]-[1,3,2]-oxazaborole (M2) (see Figure 11) are proposed as donor semiconducting materials for OPV use. Strong non-linear optical (NLO) properties for this family of organoboron molecules were previously observed [40, 41], indicating a strongly delocalized π system and suggesting its potential for OPV use. Both molecules have broad and strong absorption peaks in the visible spectrum that combined with MEH-PPV increased the absorption of the organic blends. Very few reports of boron molecules used for OPVs devices currently exist [42].

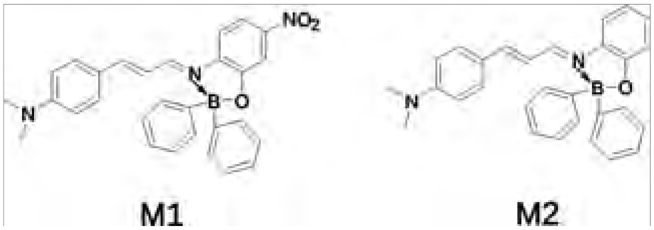

Figure 11 Chemical structure of the two molecules used in blend with MEH-PPV as donor materials.

2.1.1 Sample preparation

The commercial chemicals (MEH-PPV, polystyrene, $PC_{61}BM$, Woods metal) were purchased from Aldrich (México) and used as received. Powders of the compounds M1 and M2, previously synthesized and reported by the group (GPOM, CIO, Mexico), were used unmodified. ITO/Glass substrates with 5-15 Ω/square were purchased from Delta Technologies. Previous to the preparation of OPVs cells, the thin film morphology was studied by AFM to determine the best deposition conditions by spin cast and solvent effect. MEH-PPV solutions were prepared in the solvents tetrahydrofuran (THF), dichloromethane, chloroform and toluene; $PC_{61}BM$ was dissolved in dichloromethane, chloroform, toluene and xylene. Different mixtures of MEH-PPV and $PC_{61}BM$ were prepared. These solutions were used to make all possible combinations of solvents, always keeping a 1:1 ratio of MEH-PPV:$PC_{61}BM$, and were deposited by spin-coating over glass substrates for the morphology study.

The OPVs cells were fabricated at different material concentrations employing as electron donors, the organic semiconductors MEH-PPV, M1 and M2 mixed with the electron acceptor $PC_{61}BM$. When using an inert polymer (the host, in this study polystyrene or PS), it is possible to create films of good optical quality in which low molecular weight molecules (the guest) such as M1 and M2 can be dispersed. OPVs cells of MEH-PPV:$PC_{61}BM$ (weight ratio 1:1, 1:2, 1:3 and 1:4); M1:$PC_{61}BM$:PS, M2:$PC_{61}BM$:PS (weight ratio 1:1:0.5 in both cases); MEH-PPV:M1:$PC_{61}BM$, MEH-PPV:M2:$PC_{61}BM$ (weight ratio 1:1:2 in both cases); M1:M2:$PC_{61}BM$:PS (weight ratio 1:1:2:1) and MEH-PPV:M1:M2:$PC_{61}BM$ (weight ratio 1:1:1:3) were prepared using dichloromethane or chloroform. The solutions were deposited by spin-coating at about 1000 rpm over glass/ITO substrates. The ITO electrodes were ultrasonically cleaned in distilled water and ethanol baths with 30 minutes intervals. The organic films were heated (in air) in an oven at 80 °C for 20 min [43]. To deposit the cathode, Woods metal pellets were placed on a pyrex glass beaker and heated between 90-100 °C using a hot plate. The melted material was deposited dropping it over the organic films (heated at the same temperature to avoid freezing). The photoactive area tested was about 1 cm^2. The architecture of the cells is shown in Figure 12. A typical solar cell manufacturing process is exemplified in Figure 13.

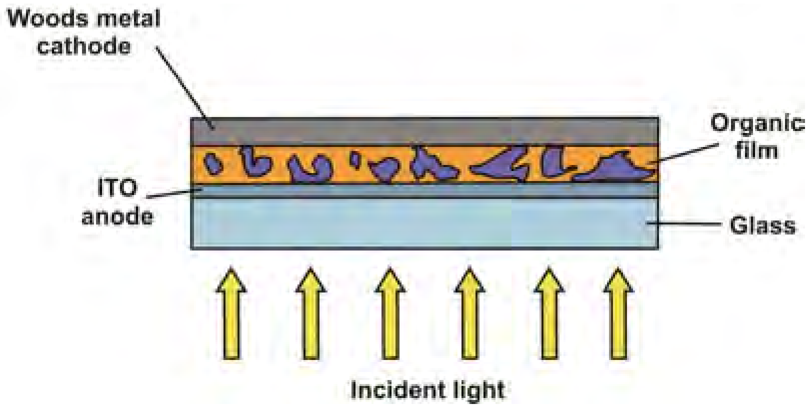

Figure 12 Design employed for the solar cells made with MEH-PPV, M1, M2 and $PC_{61}BM$ using the bulk hetero-junction approach.

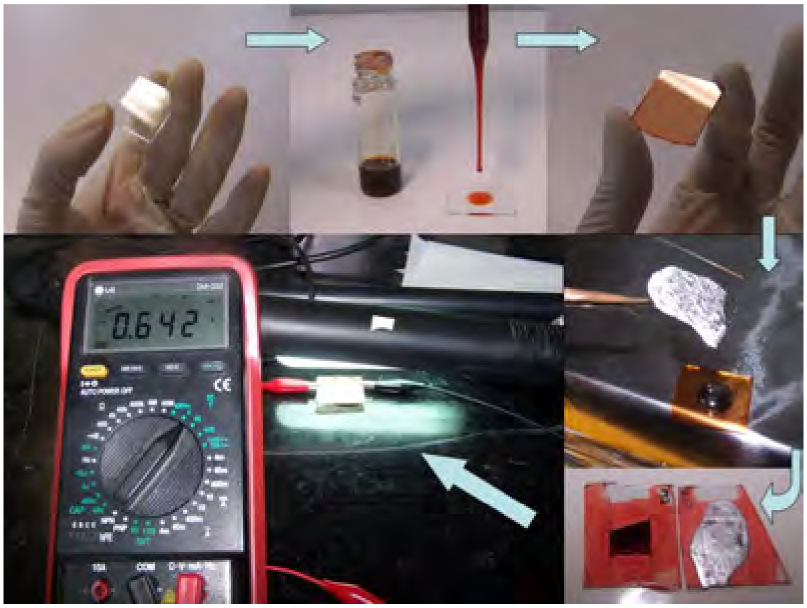

Figure 13 Manufacturing process of an organic solar cell using Wood's metal as cathode.

2.1.2 Experimental results

The morphological measurements by AFM of MEH-PPV:$PC_{61}BM$ films showed that the best component integration occurs when the same solvent (dichloromethane) is used to dissolve both materials (see Figure 14). MEH-PPV:$PC_{61}BM$ cells were made using the ratios 1:1, 1:2, 1:3 and 1:4. With the goal of maximizing electron and hole mobility by forming two inter-percolated phases of MEH-PPV and $PC_{61}BM$ and since the morphology of the phases [44] is strongly dependent on processing conditions such as solution concentration, solvent nature and annealing conditions, a study regarding the best manufacturing composition was performed on our own devices.

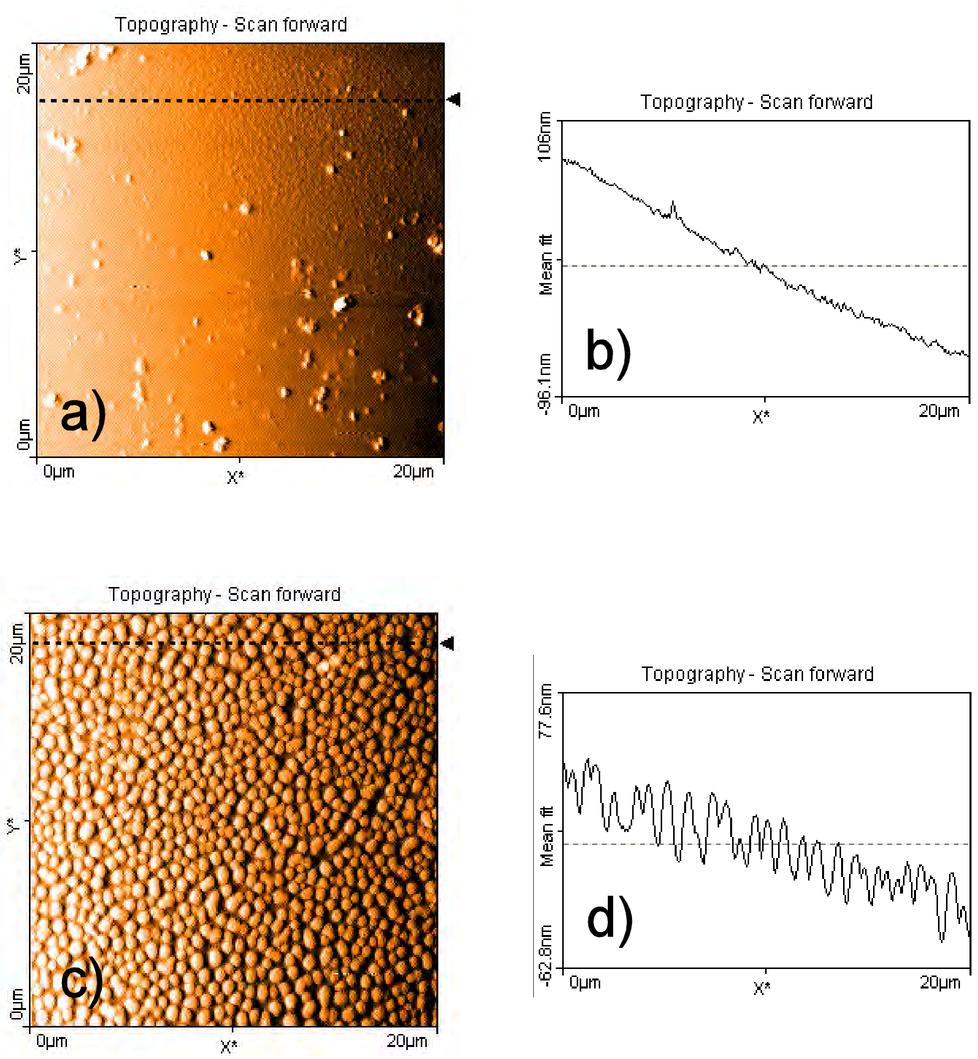

Figure 14 Surfaces of MEH-PPV:PC$_{61}$BM films at 1:1 and 1:2 weight ratios acquired by AFM. The images correspond to: a) 1:1 ratio film, b) cross section of the 1:1 ratio film, c) 1:2 ratio film, d) cross section of the 1:2 ratio film. Both films were heated at 75 °C by 20 min. The 1:3 and 1:4 blends have morphologies nearly equal to that one of 1:2: c) and d).

Tests under sunlight exhibited the best performance on current and voltage for the 1:2 (MEH-PPV:PC$_{61}$BM) ratio with $V_{oc} = 730$ mV and $J_{sc} = 0.8$ mA/cm^2. Higher concentrations of PC$_{61}$BM (1:3 and 1:4) enhance the current but reduce voltage, while lower concentrations (1:1) have smaller V_{oc} and J_{sc} than the 1:2 ratio. The AFM studies showed a considerable phase separation, i.e., a bicontinuous phase structure [44] of the fullerene PC$_{61}$BM for the concentrations that enhance the current (1:2, 1:3 and 1:4, see Figure 14 c)). These large phases, could provide quasi-continuous paths that facilitate the electrical charge transport toward the electrodes, moreover, the improved photo-response is related to the increase of the total interfacial area at the heterojunction [44]. Figure 15 shows a cross sectional SEM image of a typical film prepared for our OPVs cells. In this figure, for a film of 126 nm on glass substrate (MEH-PPV:PC_{61}BM at 1:2 weight ratios), nanocluster-shaped structures immersed in MEH-PPV, similar to the ones reported previously by Hoppe et al. [45], are observed (see also Figure 14 c)).

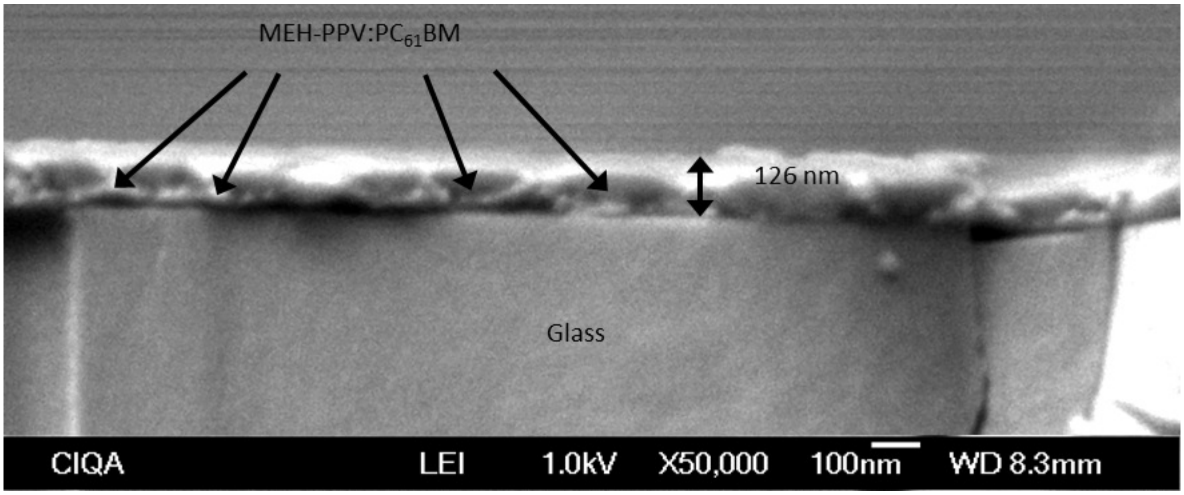

Figure 15 Cross sectional SEM image of MEH-PPV:PC_{61}BM film at 1:2 weight ratios. Film thickness was 126 nm. Nanocluster-shaped structures similar to the reported by Hoppe et al. [45] are observed.

For cells with M1:PC_{61}BM:PS and M2:PC_{61}BM:PS (PS used just as inert polymer matrix) both in a 1:1:0.5 ratio dissolved in chloroform and dichloromethane, the best performance for M1 was observed for the chloroform blend reaching, under sunlight, V_{oc} = 500 mV and J_{sc} = 0.5 mA/cm^2 with a 130 nm thin film. For M2 blends, there was not a significant difference between the performance in chloroform or dichloromethane, reaching maximum values of voltage and current: V_{oc} = 360 mV and J_{sc} = 0.37 mA/cm^2, respectively, with a 98 nm thin film. A thinner film preserves the current density J_{sc} but reduces the V_{oc} voltage. For both mixtures, a thicker film decreases the J_{sc} current, presumably due to the low electrical mobility (for most organic materials about 10^{-5} - 10^{-7} cm^2/(Vs)) [46, 47].

The spectra of MEH-PPV, M1 and M2 based films (Figure 16) have absorption bands in complementary wavelength regions. Particularly, the blend of MEH-PPV:M1:PC$_{61}$BM (1:1:2 ratio) has a wider absorption band that covers from 400 to 700 nm, which is a considerable region of the optical range. External quantum efficiency (EQE) measurements of cells prepared with this blend (Figure 17) verifies that the charge production is been extended to the whole absorption range covered by MEH-PPV and M1, indicating that M1 is effectively working as a donor material in conjunction with MEH-PPV. This increased charge production range is reflected in an increased total electrical current. Under sunlight, current densities of J_{sc} = 3.1 mA/cm^2 for the MEH-PPV:M1:PC$_{61}$BM blend and J_{sc} = 1.73 mA/cm^2 for the MEH-PPV:M2:PC$_{61}$BM blend were measured, they are larger than those for OPVs cells based on MEH-PPV, M1 or M2 alone. V_{oc} values were similar in both cases to those for OPV cells based on MEH-PPV, M1 or M2 alone (≈ 600 mV). These V_{oc} values suggest an alike inner resistance of the cells.

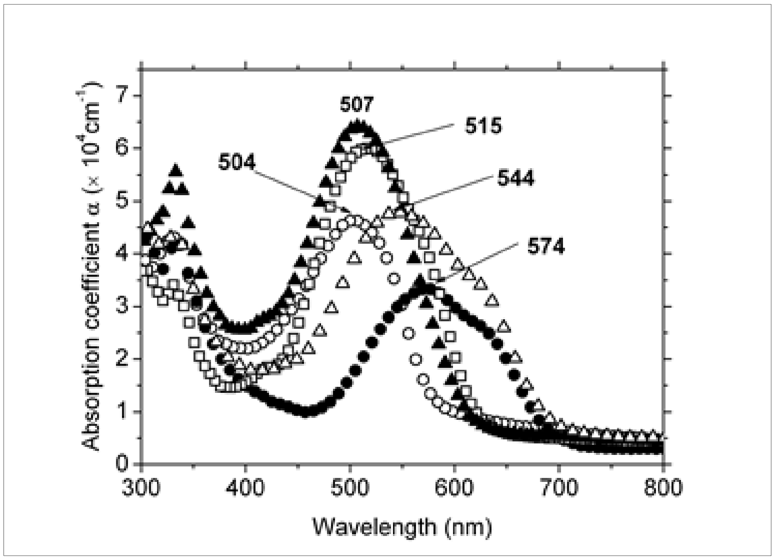

Figure 16 Absorption spectra of MEH-PPV:PC$_{61}$BM film on a 1:1 weight ratio (open circles), M1:PC$_{61}$BM:PS film on a 1:1:0.5 weight ratio (filled circles), M2:PC$_6$1BM:PS film on a 1:1:0.5 weight ratio (open squares), MEH-PPV:M1:PC$_{61}$BM film on a 1:1:2 weight ratio (open triangles) and MEH-PPV:M2:PC$_{61}$BM film on a 1:1:2 weight ratio (filled triangles). The wavelengths corresponding to the peaks are indicated.

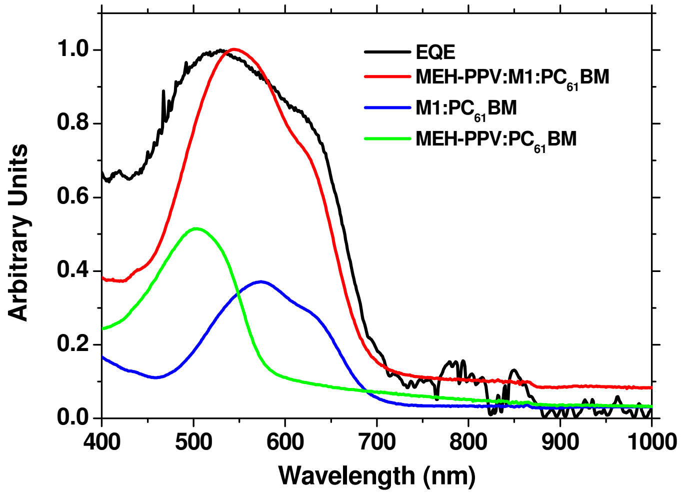

Figure 17 Comparison of EQE and absorption spectra of several organic blends; black: EQE of cell with a MEH-PPV:M1:$PC_{61}BM$ active layer; red, blue and green: absorption spectra of organic films of MEH-PPV:M1:$PC_{61}BM$, M1:$PC_{61}BM$ and MEH-PPV:$PC_{61}BM$.

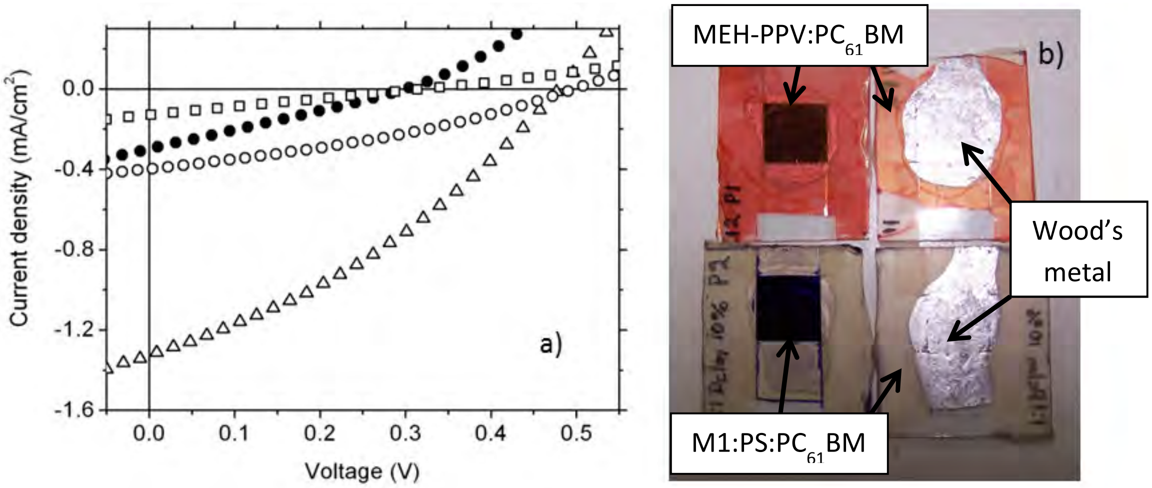

Figure 18 a) JV curves, under Xe lamp illumination at 60 mW/cm^2, for OPVs cells based on: MEH-PPV:$PC_{61}BM$ on a 1:2 weight ratio dissolved in dichloromethane (open circles), M1:$PC_{61}BM$:PS on a 1:1:0.5 weight ratio dissolved in chloroform (filled circles), M2:$PC_{61}BM$:PS on a 1:1:0.5 weight ratio dissolved in chloroform (open squares) and MEH-PPV:M1:$PC_{61}BM$ on a 1:1:2 weight ratio dissolved in dichloromethane (open triangles). b) Photograph of OPVs cell with Woods metal as cathode, active area ≈ 1 cm^2.

Graphs of J-V curves and conversion parameters under Xenon lamp using a light intensity of 60 mW/cm^2 are shown in Figure 18 and Table 1. The efficiencies of MEH-PPV:M1:PC$_{61}$BM cells increased 9 and 3.3 times in comparison to M1:PC$_{61}$BM:PS and MEH-PPV:PC$_{61}$BM respectively, mainly due to an increased charge production. This improvement in electric current means that the MEH-PPV:M1:PC$_{61}$BM blend can separate and transport more electric charge than MEH-PPV:PC$_{61}$BM or M1:PS:PC$_{61}$BM alone.

Table 1 Conversion parameters for different OPVs cells using Woods metal as cathode under Xe lamp illumination at 60 mW/cm^2. Values correspond to graphics in Figure 18.

Components (weight ratio)	Solvent	V_{oc}(mV)	J_{sc}(mA/cm^2)	FF	PCE(%)
MEH-PPV:PC$_{61}$BM (1:2)	Dichloromethane	496	0.40	0.34	0.11
M1:PC$_{61}$BM:PS (1:1:0.5)	Chloroform	301	0.30	0.26	0.04
M2:PC$_{61}$BM:PS (1:1:0.5)	Chloroform	322	0.13	0.25	0.02
MEH-PPV:M1:PC$_{61}$BM (1:1:2)	Dichloromethane	479	1.33	0.34	0.36
MEH-PPV:M1:PC$_{61}$BM$^{a)}$ (1:1:2)	Dichloromethane	600	3.1	0.34	0.8

$^{a)}$ Electrical performance tested under solar light at 80 mW/cm^2.

For the MEH-PPV:M1:PC$_{61}$BM OPV cell (see Table 1 and Figure 18), using the V_{oc} and J_{sc} values measured under sunlight (600 mV and 3.1 mA/cm^2 respectively), assuming the same *FF* (0.34) measured with Xenon lamp, and a solar intensity of 800 W/m^2, provides an estimated efficiency of up to 0.8 %.

Three possible reasons for the low electrical efficiency under our experimental conditions are the following: i) Because an electrical contact for the cell must cover the entire active surface without shorting the device and to provide uniform contact to the organic film, it is very important to avoid any damage of the film when depositing the cathode over the very thin active layers (≈ 100 nm). In our devices the active area was relatively large (≈ 1 cm^2) in comparison with many previous reports using areas round 0.07 cm^2 [42, 48-50], this could lead to a cathode that is not entirely uniform and with not good electrical contact (i.e. lower fill factor) in all the active area. To corroborate the area effect, we prepared cells of MEH-PPV:M1:PC$_{61}$BM (1:1:2 wt. ratio) with about 0.04 cm^2 of active region, by measuring the JV curve we estimated FF = 0.37. Under solar illumination the parameters V_{oc} = 600 mV and J_{sc} = 3.9 mA/cm^2 lead to an efficiency around 1.1 % for these small cells. ii) PEDOT-PSS conductive layer on ITO was not used, so the charge extraction from the BHJ to ITO was harder due to a larger difference in energy levels. iii) In our methodology, the OPVs cells were prepared in an easy and fast manner, and tested under normal room conditions, i.e., not in a controlled atmosphere within a glove-box (mainly because we didn't have a globe-box system at this stage of the doctoral work).

Despite efficiencies as high as 12% reached in the laboratory for some particular OPVs cells [51], the understanding of their performance requires to take into account several important factors such as, cell architecture, the electrodes, the film morphology and the organic materials used. By now, research is being conducted in OPVs cells even when efficiencies are rather small since it is needed to achieve a better understanding of the internal processes happening within the cells in order to increase the efficiency. On the other hand, very few reports about the use of boron complexes exist for OPVs devices, one of them the one from Quiao et al. [42] where a fluorescent fluorine-boron complex (PIDB) was used by blending it with MEH-PPV and reaching the electrical parameters: V_{oc} of 590 mV, J_{sc} of 0.068 mA/cm^2, a FF of 0.54, and an efficiency of 0.31%. Other optical uses of these boron complexes, with close relation to OPVs cells, are for electroluminescent devices (OLEDs) [52], so, the boron complexes M1 and M2 proposed here have potential uses in this area.

2.1.3 Conclusions of section 2.1

Wood's metal alloy used as cathode permits an economical, easy and fast way to manufacture OPV cells under environmental conditions without the need of high vacuum chambers or any specialized equipment like the one used to apply aluminum. Wood's metal could be an alternative to evaporated Al, Ca or other metals for fabrication and testing of new promising organic materials with different cell composition ratios and deposition conditions. As an example, in this work the performance of boronate derivatives M1 and M2, and the polymer MEH–PPV in OPVs devices was tested using this approach. In our experiments, open circuit voltages (V_{oc}) of 730 mV and short circuit currents (J_{sc}) of 0.8mA/cm^2 under solar

(AM1.5) illumination were measured for MEH–PPV:$PC_{61}BM$ based samples, V_{oc} = 500 mV and J_{sc} = 0.5 mA/cm^2 were measured under the same illumination for M1:$PC_{61}BM$ based samples. For the cells with mixtures of either M1 and MEH–PPV or M2 and MEH–PPV there was a large electrical enhancement showing V_{oc} ≈ 600mV and J_{sc} ≈ 3.1mA/cm^2. Measurements of FF from the J–V curves, under Xe lamp illumination, allow estimating the electrical efficiencies under solar illumination up to 0.8%. Currently the reported efficiency of similar devices using the architecture ITO/MEH-PPV:PCBM/Ca is aproximately ≈ 1.5% [12], while more complex architectures ITO/PEDOT:PSS/MEH-PPV:PCBM/Ca/Ag reports efficiencies of 2.07% for 80 mW/cm^2 [53]. Comparatively talking, our best conversion efficiency (PCE = 0.8%) is still good considering the simplified manufacture method used here. The Wood's metal electrode could be not viable for the future manufacture of commercial solar cells panels, but it is very convenient for quick screening of materials in research laboratories. On the other hand, OPV cells, based on the boronates M1 and M2, proof the potential of these materials to be used in organic PV devices with similar performance to those based on MEH–PPV.

2.2 Performance of OPVs cells based on a P3HT:PC$_{61}$BM blend as active layer [54]

In order to ease the application of OPV technology for large scale manufacture, architectures whose realization avoids the use of vacuum technology are very desirable. The inverted architecture using ZnO and ITO [37] as cathode and PEDOT:PSS and Ag as anode, has been implemented as a successful approach for roll-to-roll (R2R) production [55-57] of OPVs cells through a vacuum free process using silver inks as back contact. The devices obtained with these massive production tests have reached efficiencies close to 3%. Despite this efficiency is not as high as that obtained in some OPVs cells with the couple of electrodes ITO-Al, the completely vacuum free process allows mass production by using only simple and conventional technology. In this context, the exploration of new or improved approaches for the fabrication of OPVs cells that circumvent the use of vacuum deposition steps is important to further develop such technology.

In this study, through the use of the well-known polymer blend P3HT:PC$_{61}$BM [38, 58-62], the usability of Wood´s metal and silver paint as cathode and anode in conventional and inverted OPVs cells was corroborated as convenient substitutes to evaporated metals. We demonstrated that OPVs cells based in the structures ITO/PEDOT:PSS/P3HT:PC$_{61}$BM/Wood´s metal and ITO/ZnO/P3HT:PC$_{61}$BM/PEDOT:PSS/Silver paint exhibit very acceptable electrical performance which is comparable with OPVs based in P3HT:PC$_{61}$BM fabricated by conventional methods with ITO and Al as electrodes.

2.2.1 Sample preparation

The OPVs cells were fabricated under the bulk hetero-junction approach in conventional and inverted architectures; mixes of P3HT and PC$_{61}$BM in a weight ratio of 1:2 were dissolved in chloroform or chlorobenzene. The solutions were used to deposit thin films (between 80 and 120 nm in thickness) by spin-coating at about 1000 rpm. For the inverted cells, ZnO nanoparticles were synthesized following the procedure described by Beek et al. [63] obtaining particles dispersed in chlorobenzene of around 4 nm (Figure 19). The ZnO films were prepared by spin-coating at 1000 RPM the suspension. The ITO electrodes were ultrasonically cleaned with distilled water, ethanol and an alkaline solution (Hellmanex II mixed with water) in baths of 30 minutes each. The architectures followed here were ITO/ZnO/P3HT:$PC_{61}BM$/PEDOT:PSS/Anode and ITO/ PEDOT:PSS/P3HT:$PC_{61}BM$/Wood's metal for the inverted and conventional architecture respectively.

In the case of the inverted cells, three types of anodes were used: Ag, Cu and silver paint. Silver and cooper were applied by thermal evaporation while Wood's metal and silver paint were applied in a process with no vacuum steps. We used cooper as anode since its work function is similar to that of silver (Figure 6), suggesting it could perform reasonably well as anode in inverted cells. The PEDOT:PSS film was applied in the conventional case by spin-coating.

The surface of P3HT:$PC_{61}BM$ films is highly hydrophobic and doesn't allow to spin-coat water based solutions such as PEDOT:PSS over it. For all the inverted cells, the PEDOT:PSS was deposited following the next procedure: 1) a drop of PEDOT:PSS was deposited on top of the P3HT:$PC_{61}BM$ film, 2) using an air flow directed perpendicularly to the substrate, the drop was forced to spread over the whole cell, 3) while spreading the PEDOT:PSS, the air current induced the solution to dry, forming a film. Despite the thickness of PEDOT:PSS was impossible to control using this method, the efficiencies got by this method were highly reproducible. All the organic films were processed in presence of air, and annealed in an oven at 80 ºC for 20 min. The photoactive area tested was about 0.09 cm^2.

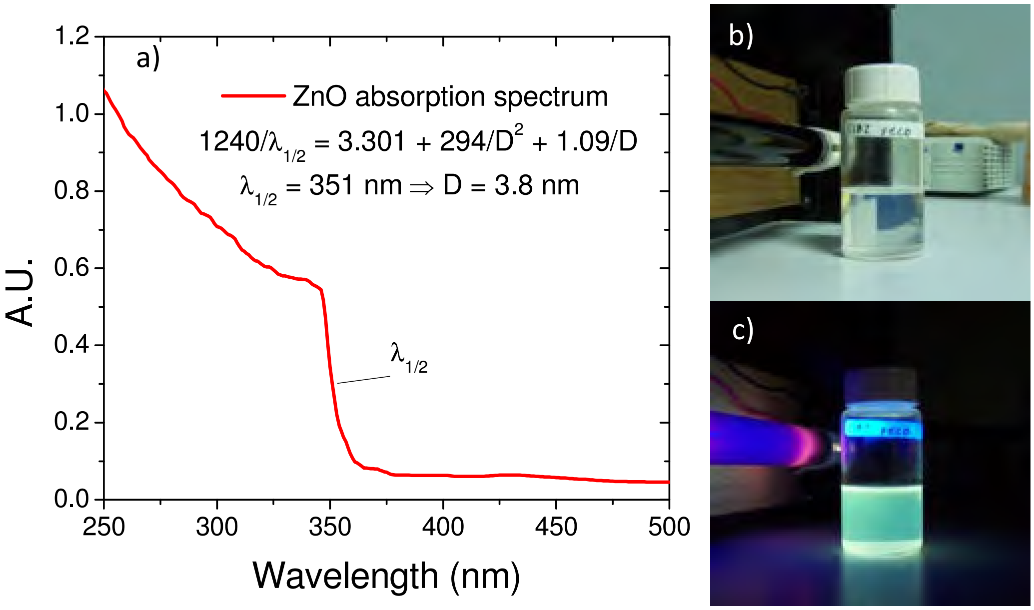

Figure 19 a) Absorption spectrum of the ZnO NPs suspended in chlorobenzene indicating an average diameter of 3.8 nm. b) Photograph of the ZnO suspension, notice that it is almost transparent and has not precipitates. c) Fluorescence under UV illumination reveals the nanoparticles.

2.2.2 Experimental results

Figure 20 shows typical JV curves recorded for our bests OPV samples based on P3HT:PC$_{61}$BM (1:2 wt. %, dissolved in chloroform). From data in Figure 20, the best electrical power conversion efficiencies (got using no vacuum steps) was about 2.2 % and 1.8 % for the inverted and conventional cells respectively. These efficiencies are in some cases comparable to typical values reported for OPVs cells fabricated by using vacuum technology for cathode deposition [58-62]; it shows that in principle Wood´s metal and silver paint can have an acceptable performance in free vacuum steps processes. The typical morphologies of the active layer and the surface of Wood's metal used in our OPVs devices were obtained by AFM (see Figure 21 and Figure 22 for images of 10×10 μm). In Figure 21 we can see that the active layer is characterized by a very smooth surface, while in Figure 22 we can appreciate that the surface of the eutectic alloy used as cathode is not as smooth as in the case of the organic layer. In this case the cathode film analyzed by AFM was removed carefully from an OPV previous to its analysis.

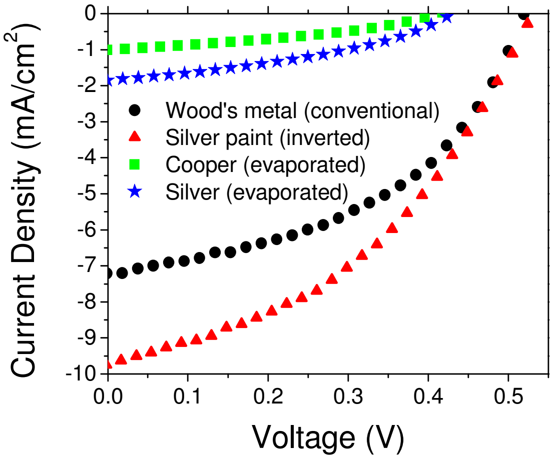

Figure 20 a) J-V curves, under Xe lamp illumination at 100 mW/cm^2, for OPVs cells based on P3HT:PC$_{61}$BM with 1:2 weight ratio dissolved in chloroform. The Wood's metal and silver paint cells were prepared in a free vacuum steps process.

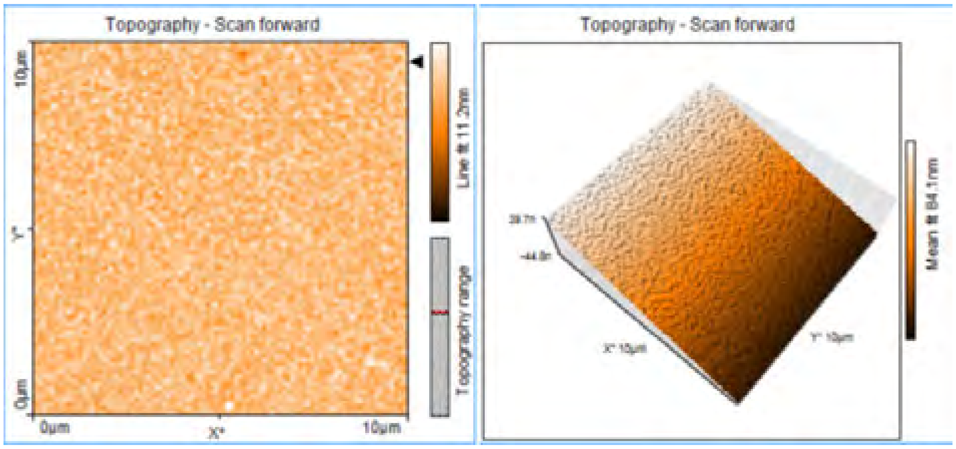

Figure 21 Surface of P3HT:PC$_{61}$BM film at 1:2 weight ratio acquired by AFM; chloroform as solvent was used. The polymer blend was annealed at 80 °C by 20 min.

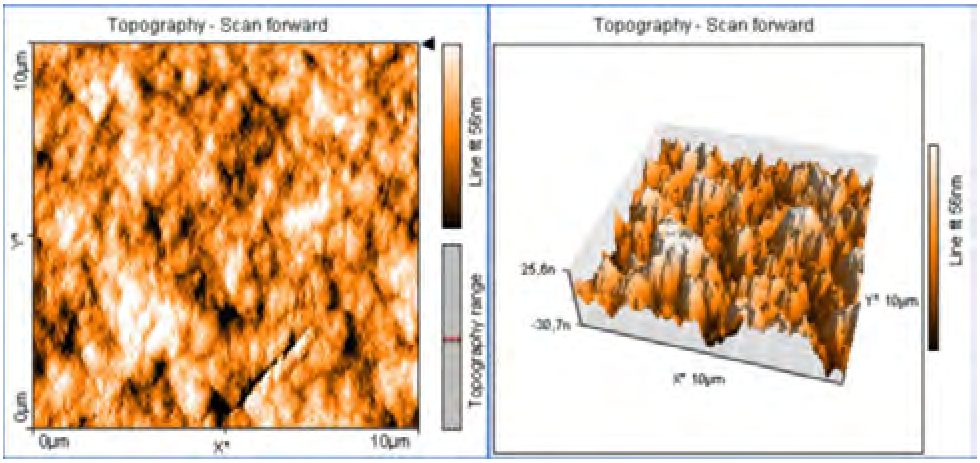

Figure 22 AFM image of the surface of the eutectic alloy Wood's metal used as cathode in an OPV.

In addition to the characteristics of the interface between the organic layer and the cathode there are other factors that determined the performance of our OPV's. i.e., processing conditions such as solution concentration, solvent nature and annealing treatments [44]. These factors have been taken into account in the inverted case when the overall performance of our OPVs fabricated through vacuum free process is compared with the performance of devices with similar composition of the organic layer but with evaporated Ag and Cu. Table 2 summarizes the values for the electrical conversion parameters V_{oc}, J_{sc}, FF and PCE obtained for our cells and their comparison with the values of structures ITO/PEDOT:PSS/P3HT:PC_{61}BM/Al reported in recent works [58-60]. From Refs. [59, 60] we can see that our OPV cells electrical performance is very acceptable (larger in fact), having advantages taking into account the fast and vacuum free process used here. It must be pointed out that the conductivity of Woods metals is 1×10^{6} S/m [64], which is about an order of magnitude smaller compared with Aluminum (3.5×10^{7} S/m) [65].

Table 2 Electrical parameters of OPVs cells for blends of P3HT:$PC_{61}BM$ illuminated with a Xe lamp at 100 mW/cm^2.

Architecture	Concentration wt. ratio	Back-contact	V_{oc} (mV)	J_{sc} (mA/cm^2)	FF	PCE (%)
Conventional	(1:2) 6:6 mg/ml	Wood's metal	528	7.35	0.45	1.75
Inverted	(1:1) 30:30 mg/ml	Silver paint	530	9.64	0.42	2.19
Inverted	(1:0.6) 5:3 mg/ml	Cooper(evaporated)	412	1.01	0.37	0.15
Inverted	(1:0.6) 5:3 mg/ml	Silver (evaporated)	428	1.86	0.38	0.30

Note: From Ref. [60], for samples based on P3HT:$PC_{61}BM$ (1:1):

V_{oc} = 640 mV, J_{sc} = 3.6 mA/cm^2, FF = 0.30 and PCE = 0.9 without graphene

V_{oc} = 640 mV, J_{sc} = 5.3 mA/cm^2, FF = 0.41 and PCE = 1.4 with 10 % of graphene

From Ref. [59], idem:

V_{oc} = 480 mV, J_{sc} = 5.1 mA/cm^2, FF = 0.46 and η = 1.1

From Ref. [58], for samples based on P3HT:$PC_{61}BM$ (1:1.5):

V_{oc} = 580 mV, J_{sc} = 9.41 mA/cm^2, FF = 0.64 and η = 3.5

2.2.3 Conclusions of section 2.2

The photovoltaic performance of OPVs cells based on the polymer blend P3HT:$PC_{61}BM$ (1:2 wt. ratio) by using Wood's metal and silver paint as cathode and anode respectively was very acceptable in comparison with previous reports of devices based on the same polymers blend. The fabrication of our OPVs cells was possible within a vacuum free process. In addition, this manufacturing process was easier and faster than other processes reported in the literature where usually Al is employed as back electrode and where specialized equipment is needed. Our electrical performance with Wood's metal was V_{oc} = 528 mV, J_{sc} = 7.35 mA/cm^2, FF = 0.45 with an efficiency PCE = 1.8 % and with silver paint V_{oc} = 530 mV, J_{sc} = 9.64 mA/cm^2, FF = 0.42 and PCE = 2.19%. We associate the higher efficiency got for the inverted cell to the greater stability respect degradation that is associated with this architecture. Our results also indicated that, while thermal evaporation can cause severe damage to the organic films due to the high energy of the evaporated materials (possible reason of their low PCE in our experiments), Wood's metal and silver paint are much more friendly with the organic films.

2.3 Optical design of transparent thin silver electrodes for microcavity based devices [66]

ITO-free polymer solar cells with efficiency as high as 6.6% and 5.8% were fabricated on glass and PEN by using TeO_2 to enhance in-coupling of light in an Ag-Ag microcavity. These cells exhibited higher performance, selective microcavity resonance as a function of the thickness of TeO_2, and better bending stability than flexible devices made with ITO (Figure 23).

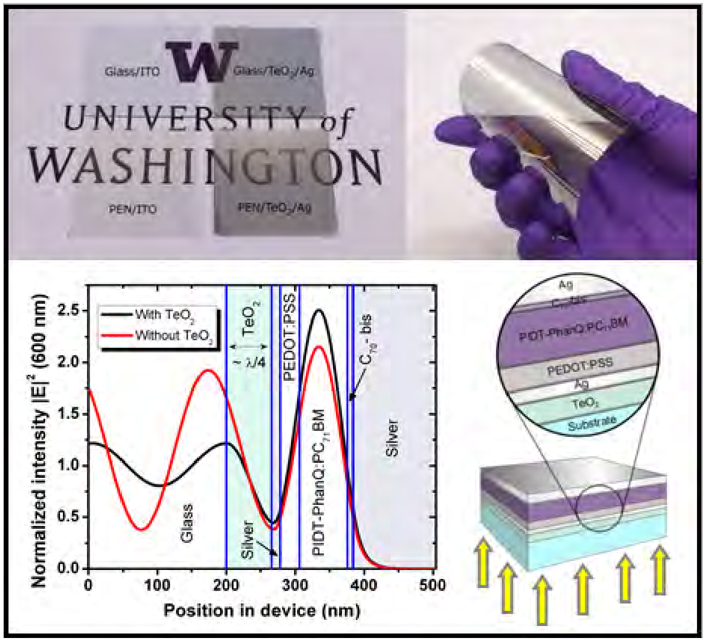

Figure 23 Overview of the project for optical design of semitransparent, ultra-thin, highly conductive, silver electrodes.

Although polymer/fullerene blends has been employed to increase the number of interfaces for facilitating charge separation, the low carrier mobilities and tortuous transport paths in these structures increase recombination losses in thicker devices [12, 67, 68]. Therefore, it is important to develop efficient light-trapping structures that can increase light absorption and at the same time be compatible with processes used for fabricating high-performance flexible thin film OPVs [69, 70].

Indium is a rare and valuable element used in the manufacture of ITO-based flat panel displays and portable electronics. Due to rapid expansion of the consumer electronics market and natural scarcity of indium, the price for ITO has increased significantly in recent years. Therefore, it is critical to find viable options that can replace ITO [71, 72]. Besides, the low mechanical ductility and high sheet resistance ($\approx 60\ \Omega/\square$) of ITO on flexible substrates also need to be improved [73-75]. It is known that the performance of large-area solar cells is dictated by their series resistance which significantly affects fill factor and PCE [76-78]. Therefore, the proposed ITO replacement should possess even lower resistance than ITO. Several alternatives have been tried, including the use of conducting polymers [79, 80], carbon nanotubes [81], graphene films [82], metal nanowires [83], metal grids [84-86], and ultrathin metal films (UTMF) [87]. Among them, metal grids and UTMF combine the characteristics of high electrical conductivity of metals and good mechanical ductility on thin films (≈ 5-40 nm). Especially, the UTMFs possess good compatibility with most organic materials and can be simply applied by thermal evaporation. However, the application of UTMFs has been limited by their considerable absorption and reflection, which cause poorer device performance than ITO. Among all metals attempted, Ag exhibits the lowest resistivity ($1.62 \times 10^{-8}\ \Omega\ \ \mathrm{m} = 1.62\ \mu\Omega\ \ \mathrm{cm}$), the highest optical transparency, and is extremely ductile (only surpassed by Au), making it the preferred choice for UTMF electrodes.

The conductivity and optical properties of thin metal films are strongly dependent on the quality of the films such as roughness, grain size, and film continuity, which is governed by the nucleation and growth kinetics of metals on a particular substrate. The initial steps of Ag thin film growth have been extensively studied and identified with different growth modes, like the Volmer-Weber mode (*ie.* island mode) or the Stranski-Krastanov mode (*ie.* layer-plus-island mode) [88-90]. They are strongly dependent on the type of substrate and the rate of vacuum deposition. In particular, the poor wettability of Ag on electrically insulating substrates often leads to undesirable rough surface morphologies, high sheet resistances, and poor optical quality [91].

It is known that conductivity and optical quality of UTMFs can be improved considerably by applying an adequate seed layer. For example, the wetting angles of molten silver over substrates treated with TeO_2 and MoO_3 (≈ 50°) have been reported to be much lower than that using other metal oxides like ZnO or Ta_2O_5 (≈ 90°) [92]. TeO_2 and MoO_3 not only are transparent to visible light but also have quite low melting points (733°C and 795°C respectively), allowing them to be easily evaporated over glass or plastic substrates before the deposition of silver. Since charge generation is affected by the spatial distribution of the optical electric field within the device; a careful selection of film thickness or insertion of additional transparent layers as optical spacers will contribute to higher current densities and improve overall performance [5, 93].

In this study, we have applied a high refractive index TeO_2 layer to facilitate the growth of smooth, highly conductive, and optically transparent thin silver films by thermal evaporation. By coupling with optical design, the TeO_2 film allowed us to improve the collection and trapping of light, leading to superior device performance that even exceeds that using ITO as electrode. Although similar approaches have been tried to improve the performance of OLED and OPV devices [94, 95], our results show the highest efficiency.

A novel bilayer hybrid electrode consisting of ultra-thin fullerene-containing surfactant and Ag metal is exploited to achieve a suitable cathode with high conductivity. The fullerene surfactant (C_{70}-bis, Figure 24) was reported earlier as an excellent interfacial electron selective layer (ESL) that not only can effectively modify the energy level alignment at the organic/metal cathode interface but also facilitate more efficient electron extraction and photocurrent generation [96, 97].

2.3.1 Experimental

The solar cells prepared for this project are based on the following device architecture: polyethylene naphthalate (PEN) or glass/TeO_2 (10-70 nm)/Ag (12 nm)/PEDOT:PSS (28 nm)/PIDT-PhanQ:$PC_{71}BM$ (66 nm)/C_{70}-bis (8 nm)/Ag (120 nm), where the (BHJ) active layer is based on the blend of PIDT-PhanQ:$PC_{71}BM$ [14], and the surfactant (C_{70}-bis) [97, 98] functions as the electron selective layer as illustrated in Figure 24. The PIDT-PhanQ polymer was synthesized within the Jen group (Seattle, University of Washington), $PC_{71}BM$ was purchased from American Dye Source. The reference devices were made with the same device structure but using commercially available ITO-coated (120 nm) glass substrates or PEN substrates as the transparent electrode.

2.3.1.1 Electrode fabrication and characterization

The substrates (glass and ITO-coated glass: Colorado Concept Coatings LLC, PEN: Teonex Q65FA, ITO-coated plastic: Bayview Optics) were cleaned using soap, acetone and isopropyl alcohol (IPA) in successive 10 min sonication steps applying a final 20 s oxygen plasma treatment to eliminate any remaining organic component. TeO_2 films of 10, 20, 30, 40, 50, 60 and 70 nm were applied by thermal evaporation at 0.2 Å s^{-1} followed by a 12 nm Ag film applied at 5 Å s^{-1} at a vacuum pressure $<10^{-6}$ torr. The transmission spectra of the electrodes were measured in air by using a Perkin-Elmer Lambda-9 UV/VIS spectrometer, while an Alessi four-point probe was used for measuring the sheet resistance.

2.3.1.2 Device fabrication

To avoid possible etching of Ag by the aqueous solution of PEDOT:PSS, a layer of PEDOT:PSS/IPA/butanol in proportion of 1/2/2 was applied first over the Ag substrate and then the aqueous solution of PEDOT:PSS was spin-coated. PhanQ (5 mg/ml) and $PC_{71}BM$ (15 mg/ml) were dissolved in dichlorobenzene, stirred overnight at 80 °C and then spin-coated at 2000 RPM and annealed at 110 °C in a glove box under N_2 atmosphere to create a film of ≈ 66 nm. The surfactant film (≈ 8 nm) was also applied within the glove box at 5000 RPM and annealed at 110 °C. Finally, a 120 nm-thick Ag film was evaporated at 5 Å/s through a mask to define an OPV area of 10.08 mm^2. The thickness of each layer was measured by using Atomic Force Microscopy (AFM).

2.3.1.3 Device characterization

The JV measurements were performed under N_2 atmosphere using a Keithley 2400 source meter. A 300 W xenon arc solar simulator (Oriel) with an AM 1.5 global filter operated at 100 mW/cm^2 was used to simulate the AM 1.5G solar irradiation. The illumination intensity was corrected by using a silicon photodiode with a protective KG5 filter calibrated by the National Renewable Energy Laboratory (NREL). The External Quantum Efficiency (EQE) was recorded under monochromatic illumination with another 450 W xenon lamp in ambient atmosphere. The incident beam was chopped with a mechanical chopper, and the photocurrent was recorded with a lock-in-amplifier (Stanford Research Systems SR830). The irradiance spectrum of the solar simulator (used for the numerical simulation) was measured using an Ocean Optics spectrometer.

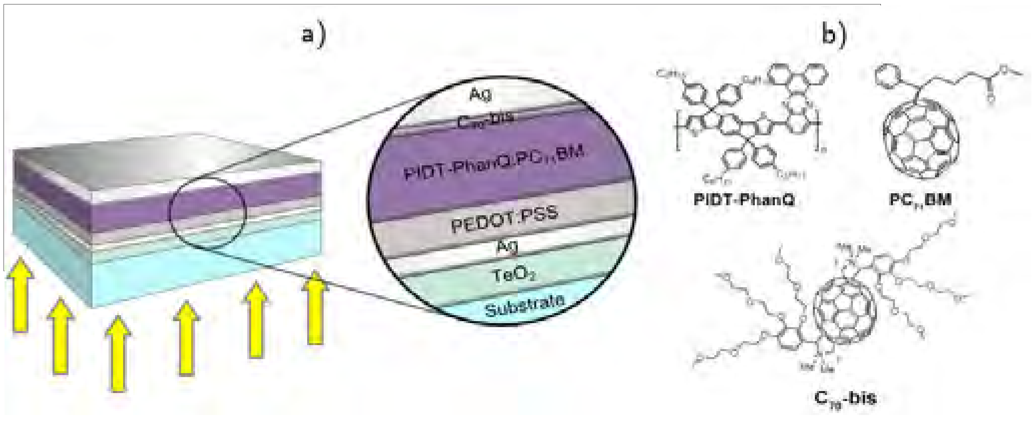

Figure 24 a) Schematic cross section of the PIDT-PhanQ OPV devices showing the order of the layers. The light is incident from the substrate side. b) Schematic diagrams for the materials used as surfactant and active layer.

2.3.2 Optical analysis

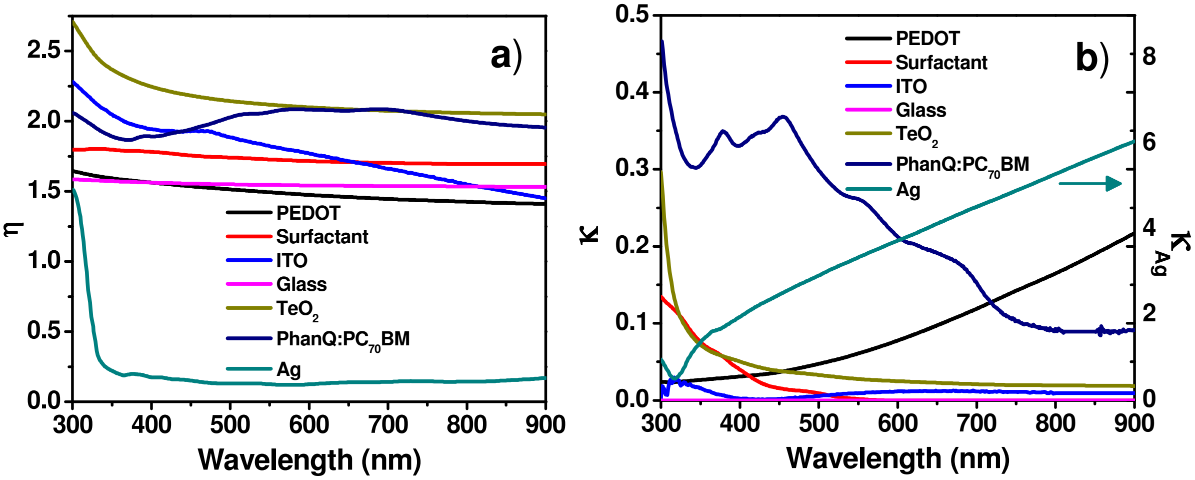

Figure 25 Refractive indexes used in the simulation: a) real refractive index (η), b) Extinction coefficient (κ). For the particular case of silver, κ_{Ag} is plotted in a different scale because it is much higher than the κ values of the other materials.

Due to the use of two metallic electrodes, an optical microcavity between both Ag contacts is formed. In order to achieve a constructive resonant condition within the microcavity, the Ag electrodes should be positioned at the nodes of the electric field. This can be achieved by making the optical length of the cavity a multiple integer of the wavelength. Because the reflections at each Ag electrode will introduce phase changes in the field, we need to explicitly include these phase changes to calculate the optical path of the light traveling in each direction accordingly to the following equations:

$$\sum_i \eta_i d_i + \frac{Arg(r_{A-P})\lambda}{2\pi} = m\lambda \tag{59}$$

$$\sum_i \eta_i d_i + \frac{Arg(r_{S-A})\lambda}{2\pi} = m\lambda \tag{60}$$

where, m is a positive integer, η_i is the real part of the refractive index, d_i is the thickness of the films between the electrodes, r_{A-P} and r_{S-A} are the Fresnel complex reflection coefficients at the interfaces Ag-PEDOT and Surfactant-Ag respectively and $Arg(r)$ is the argument of the complex number. Equations (59) and (60) are only satisfied when $Arg(r_{A-P}) = Arg(r_{S-A})$, so we need to make sure that at least $Arg(r_{A-P}) \sim Arg(r_{S-A})$ when designing the microcavity. If not the case, the asymmetry would origin destructive interference that would reduce the electric field intensity. Combining (59) and (60) we get the resonance condition:

$$\sum_i \eta_i d_i + (Arg(r_{A-P}) + Arg(r_{S-A}))\frac{\lambda}{4\pi} = m\lambda \tag{61}$$

As an example, for a wave of 600 nm, if $n_{PEDOT} = 1.47 + i0.08$, $n_{BHJ} = 2.08 + i0.21$, $n_{C70-bis} = 1.72 + i1.04e - 6$ and $n_{Ag} = 0.12 + i3.73$ then the optical path added by the reflections are $\frac{Arg(r_{A-P})\lambda}{4\pi} = 185.85$ nm and $\frac{Arg(rS-A)\lambda}{4\pi} = 191.25\,nm$ (quite close to each other). According to equation (61), for $m = 1$, if the thickness of PEDOT is 28 nm and surfactant is 8 nm, then technically, an active layer of 81 nm would be enough to produce resonance. It should be noticed that this is an ideal condition that assumes there are reflections only at the Ag interfaces. In the real case, the reflections at the PEDOT-BHJ and BHJ-surfactant interfaces also modify the electric field distribution, affecting the resonant condition, additionally, the active layer is not exactly at the middle of the microcavity, and so, a slightly asymmetric distribution of the field could be more appropriated. The simulation by TMM considering all the reflections indicated that a 70 nm active layer (instead of 81 nm) would be the best choice to maximize the field within the BHJ (Figure 26 a).

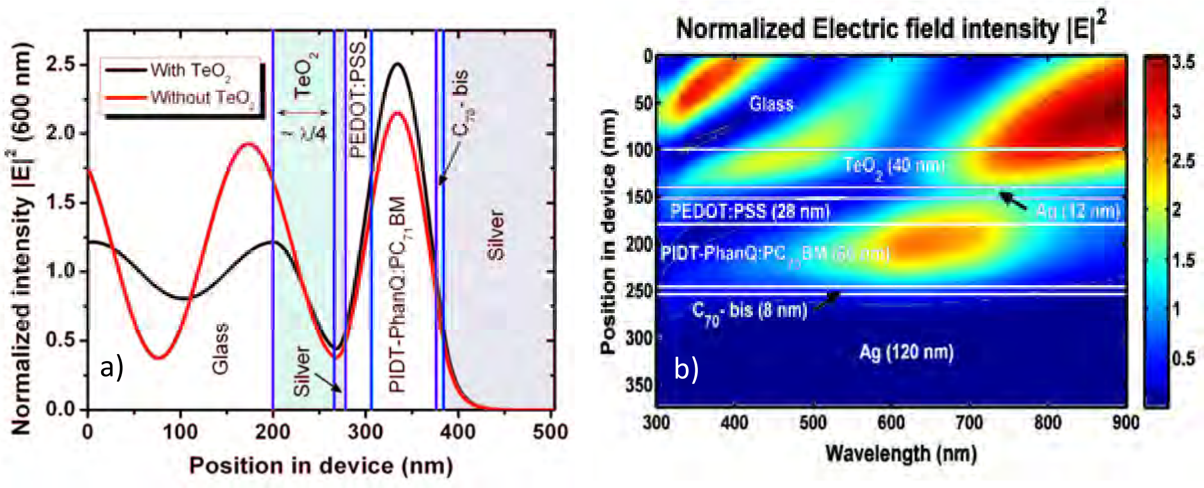

Figure 26 Electric field calculated by TMM considering a unitary incoming intensity for: a) a 600 nm light wave (incident from the left) showing the effect of a 66 nm (≈ λ/4) TeO_2 film on a cell with a 70 nm active layer, notice the dramatic decrease in the reflection and the maximized intensity within the cell respect the case without TeO_2; b) general case considering all the wavelengths (light incoming from the upper side), the thicknesses of all the films corresponds to the dimensions of the actual devices and were selected to enhance $J_{sc-100\%}$.

By introducing a TeO_2 film between the glass and silver, a portion of the light, back reflected by the transparent Ag electrode, can be reflected again towards the solar cells by the interface glass-TeO_2, due to the big difference between the refractive indexes. In order to illustrate the effect of the TeO_2 film, the calculated electric field with and without the TeO_2 film for a single wavelength of 600 nm is plotted in Figure 26a. The thickness of the TeO_2 film (66 nm) is adjusted in order to maximize the electric field within the BHJ.

Because, $\kappa \approx 0$ for both TeO_2 and glass and because $\eta_{TeO2} > \eta_{glass}$, the reflection at this interface does not add any phase change to the wave, therefore, the glass-TeO_2 interface should be placed at an antinode in order to, by constructive interference, reinforce the field within the cell. Since the semitransparent Ag film is very thin and because by design it is placed in a node of the field, the interface glass-TeO_2 will be in the first antinode when the thickness of TeO_2 satisfies:

$$\eta_{TeO_2} d_{TeO_2} = \frac{\lambda}{4} \tag{62}$$

when this is fulfilled, the light attempting to escape from the Ag-Ag system is back reflected by the glass-TeO_2 interface and reintroduced in the Ag-Ag cavity, reinforcing the field within the BHJ. Observe that, in absence of an Ag-Ag microcavity, such reinforcing effect does not exist, so, the transmission spectrum of a glass/TeO_2/Ag substrate alone is expected to be lower than ITO (Figure 28).

Following the previous example, if λ = 600 nm, the corresponding TeO_2 thickness should be $d_{TeO2} = 71\,nm$. Again, this is only a simplified vision of the whole process, the accurate calculation by TMM considering all the interfaces indicates that 66 nm (instead of 71 nm) is the best choice to maximize the field (Figure 26a). In this work, the calculations are mainly based on the predictions of a TMM simulator because of its higher accuracy and the possibility to simultaneously optimize for several wavelengths. Despite the mismatch between the simplified model (consisting on equations (61) and (62)) and the simulation, the simplified model is explained here because it provides a first approach about how to design the OPV architecture when the access to an accurate simulation method is not possible.

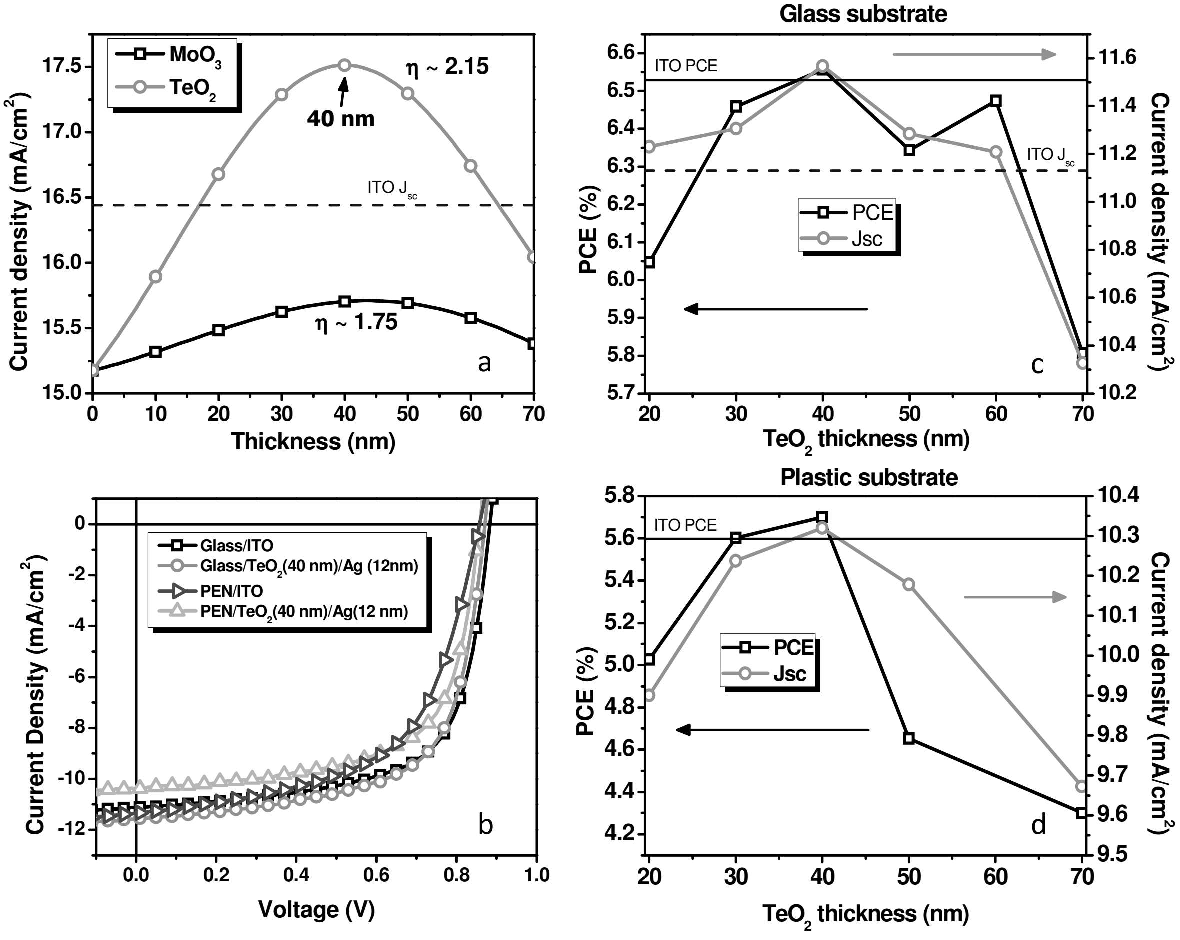

Figure 27 a) Comparison of the simulated current (Jsc-100%) anticipated for devices using different thicknesses of MoO3 and TeO2, respect the simulated current calculated for the ITO device, b) J-V curves for the best performed devices on glass and plastic (in the case of PEN/TeO$_2$/Ag, the curve represents the device after 91 bends, point where the maximum performance was achieved), c) and d) PCE and J$_{sc}$ of devices manufactured on glass and plastic substrate respectively, showing a maximum current at 40 nm as was predicted by the TMM simulation.

Because every wavelength of light absorbed will contribute to the overall performance, it requires tuning of both active layer and TeO$_2$ thicknesses to maximize the field intensity over the whole optical range in order to optimize the devices. The exciton generation rate was calculated at each point in the BHJ by using the electric field calculated by TMM for all meaningful wavelengths (300-900 nm, Figure 26b), the absorbance in the BHJ ($\alpha = \frac{4\pi\kappa}{\lambda}$), and the amount of photons associated with the source of light (intensity spectrum of the solar simulator).

The election of thicknesses for both active layer and TeO_2 film that maximizes $J_{sc-100\%}$ is an efficient way to optimize the performance. The real thicknesses of TeO_2 and BHJ layers used in our devices ($d_{TeO2} = 40\, nm$, $d_{BHJ} = 66\, nm$) are very close to the ones determined by the TMM modeling (considering the whole optical range) to maximize $J_{sc-100\%}$ ($d_{TeO2} = 40\, nm$, $d_{BHJ} = 65\, nm$) (Figure 26b). To clarify the effect of a high refractive index layer on the $J_{sc\text{-}100\%}$ value, we have simulated two materials, MoO_3 ($\eta \approx 1.75$) and TeO_2 ($\eta \approx 2.15$), and compared the results with the same device using ITO as electrode (Figure 27a). Both materials have a positive effect on the generated current. However, the higher refractive index TeO_2 allows the system to reach higher $J_{sc-100\%}$ (when a 40 nm thick TeO_2 film is used) than that calculated for ITO.

Concerning the thickness of Ag as electrode, a too thin or too thick Ag film will lead to high sheet resistance (originated by electron scattering from the surface and grain boundaries) or low transparency [87, 99]. Fortunately, high transparency and low sheet resistance ($R_{\square-TeO2.} =$ 7.02 Ω/□ compared to 13.53 Ω/□ for ITO) can be achieved when high refractive index TeO_2 is used in combination with 12 nm thick Ag. The detailed relationship of transmission and resistance as a function of Ag thickness is depicted in Figure 28. Although the transparency of the hybrid TeO_2/Ag electrode is lower than ITO, the resulting microcavity resonant condition amplifies the electric field within the cell to give higher performance than the ITO based devices.

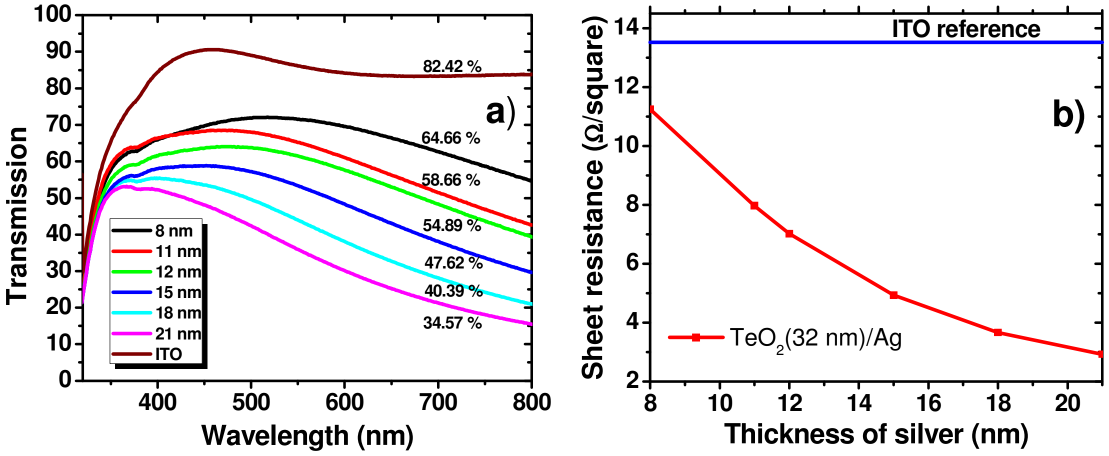

Figure 28 Transmission spectra (showing the average percent transparency) and b) sheet resistance of several glass/TeO2 (32 nm)/Ag electrodes as a function of the thickness of silver.

The PCE and J_{sc} of devices on glass and PEN with different TeO_2 thickness are plotted in Figure 27c and Figure 27d. In both cases, the best device performance was found to be the one based on a 40 nm thick TeO_2 film which fits very well with the results from simulation. The JV curves of the best device based on ITO and TeO_2/Ag coated on glass and PEN are presented in Figure 27b. Due to the high deposition rate required for the deposition (5 Å/s); it is difficult to keep exactly the same thickness of Ag for each device. The slight fluctuations observed on Figure 27c and Figure 27d are attributed to small variation of the Ag thickness that changes the transparency or conductivity of the films which affects the device performance. The PCE of the devices using TeO_2 (40 nm)/Ag substrates ($PCE_{glass-Ag}$ = 6.6 %, PCE_{PEN-Ag} = 5.8 %) surpasses those observed on ITO ($PCE_{glass-ITO}$ = 6.5 %, $PCE_{PEN-ITO}$ = 5.6 %). Although few reports have also shown good device performance when UTMFs were used, the highest achieved efficiency previously reported is only 4.4% [95]. Therefore, it is very encouraging that high efficiency OPVs using UTMFs can be achieved.

2.3.3 Morphological study

The AFM measurements (Figure 29 and Figure 30) revealed that the thermally evaporated TeO_2 exhibits a relatively small and uniform grain size with a root mean square roughness of 0.6 nm on glass and 1.5 nm on PEN. In particular, the PEN film presented large peaks that are considerably smoothed after the application of TeO_2 (Figure 30 a and b). In both substrates, the silver films grew forming extended islands, partially connected among them. These connected islands provide the necessary pathways for the flux of electrical charges in the UTMF.

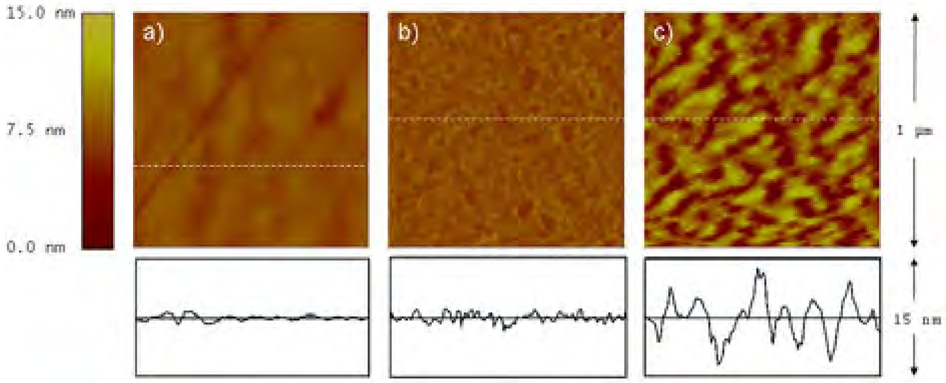

Figure 29 AFM images (1x1 µm2) of the surfaces of: a) glass, b) glass/TeO_2 (40 nm) and c) glass/TeO_2 (40 nm)/Ag (12 nm).

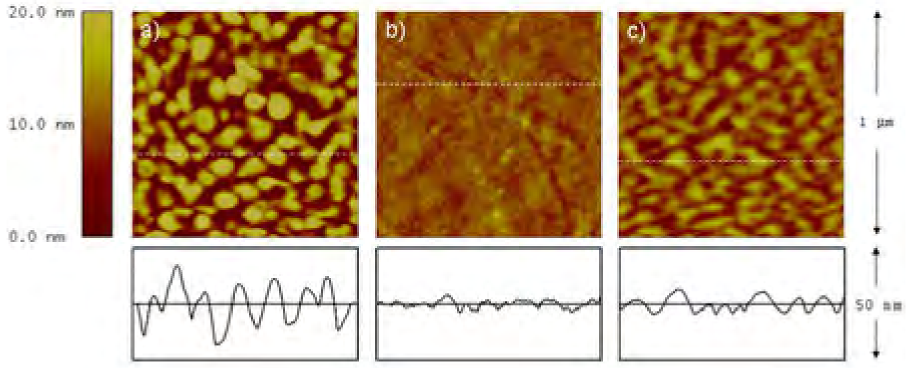

Figure 30 AFM images (1x1 µm2) of the surfaces of: a) PEN, b) PEN/TeO_2 (40 nm) and c) PEN/TeO_2 (40 nm)/Ag (12 nm).

2.3.4 Bending effect

To evaluate possible degradation that may be caused by mechanical bending of flexible OPVs, a series of tests have been performed on devices with ITO and TeO_2/Ag electrode on PEN (as illustrated in Figure 31) using a cylinder (radius R = 0.64 cm) to keep the same bending curvature. The ITO based flexible PSC exhibited a dramatic decrease of its performance starting from the first bending and continued to decrease when bending cycles proceed. In contrast, the performance of the devices with TeO_2 (40 nm)/Ag (12 nm) electrode is much more stable even after more than 100 bending cycles. Indeed, the performance of the TeO_2 based device increased slightly with the bends, growing from an original PCE = 5.7% to 5.8% after 91 bending cycles. A summary of the electric parameters of the OPV cells (corresponding to the J-V curves on Figure 27 b) is shown in Table 3. More details about the evolution of the parameters on the flexible devices as a function of the number of bending cycles can be found in Table 4 and Table 5.

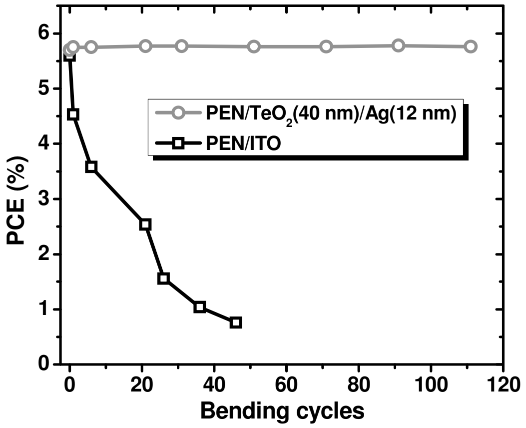

Figure 31 Effect of continuous bending over the PCE of the flexible PSC devices using both TeO_2/Ag and ITO substrates. The performance of ITO decreased immediately after the first bending while the TeO_2/Ag based device remained unharmed even after more than 100 bending cycles.

Table 3 Extracted parameters of the OPV devices on PEN or glass for both ITO and TeO_2/Ag electrodes corresponding to the JV curves shown in Figure 27b.

Substrate	Electrode	n [a]	R_s [Ω cm^2][b]	R_p [Ω cm^2][c]	V_{oc} [V]	J_{sc} [mA cm^{-2}]	FF	PCE [%]
Glass	ITO	2.14	1.42	558.02	0.88	11.13	0.66	6.53
	TeO_2/Ag	2.21	1.36	489.91	0.87	11.57	0.65	6.56
PEN	ITO	2.59	6.74	375.27	0.86	11.35	0.58	5.60
	TeO_2/Ag	2.22	0.74	533.91	0.86	10.39	0.65	5.78

Table 4 Extracted parameters of the ITO based PSC devices on PEN (showing the effect of the bending over the parameters) and glass.

Bends	n	R_s [Ω cm^2]	R_p [Ω cm^2]	V_{oc} [V]	J_{sc} [mA cm^{-2}]	FF	PCE [%]
0	2.59	6.74	375.27	0.86	11.35	0.58	5.60
1	3.23	6.11	213.32	0.81	11.41	0.49	4.53
6	2.38	8.75	114.60	0.79	11.20	0.41	3.58
21	2.29	23.90	85.60	0.76	9.78	0.34	2.54
26	2.96	55.60	82.29	0.75	7.10	0.29	1.56
36	0.91	90.06	36.07	0.66	5.84	0.27	1.04
46	0.43	128.89	22.86	0.64	4.55	0.26	0.76
Glass	2.14	1.42	558.02	0.88	11.13	0.66	6.53

Table 5 Extracted parameters of the TeO2 (40 nm)/Ag (12 nm) based PSC devices on PEN (showing the effect of the bending over the parameters) and glass.

Bends	n	Rs [Ω cm^2]	Rp [Ω cm^2]	Voc [V]	J_{sc} [mA cm^{-2}]	FF	PCE [%]
0	2.21	0.75	508.28	0.86	10.33	0.64	5.70
1	2.16	0.80	492.33	0.86	10.41	0.65	5.75
6	2.23	0.71	550.74	0.86	10.33	0.65	5.75
21	2.16	0.78	521.40	0.86	10.36	0.65	5.77
31	2.17	0.77	528.69	0.86	10.37	0.65	5.77
51	2.15	0.79	522.01	0.86	10.33	0.65	5.76
71	2.18	0.81	521.13	0.86	10.37	0.65	5.76
91	2.26	0.74	533.91	0.86	10.39	0.65	5.78
111	2.18	0.80	520.06	0.86	10.41	0.65	5.76
Glass	2.21	1.36	489.91	0.87	11.57	0.65	6.56

2.3.5 Quantum efficiency

Although all materials are involved in the total absorption of an OPV, only the light absorbed by the active layer contributes to the current generation. Among other data, the use of TMM simulation allowed us to discriminate how much light is lost in reflection or absorption in other layers, providing an easy way to estimate the absorption occurred within the BHJ. In Figure 32a, the experimental EQE and the simulated absorption in the BHJ are plotted together. The extraordinary similarity between measured EQE and modeled absorption curves is a good testimony of the validity of the optical model.

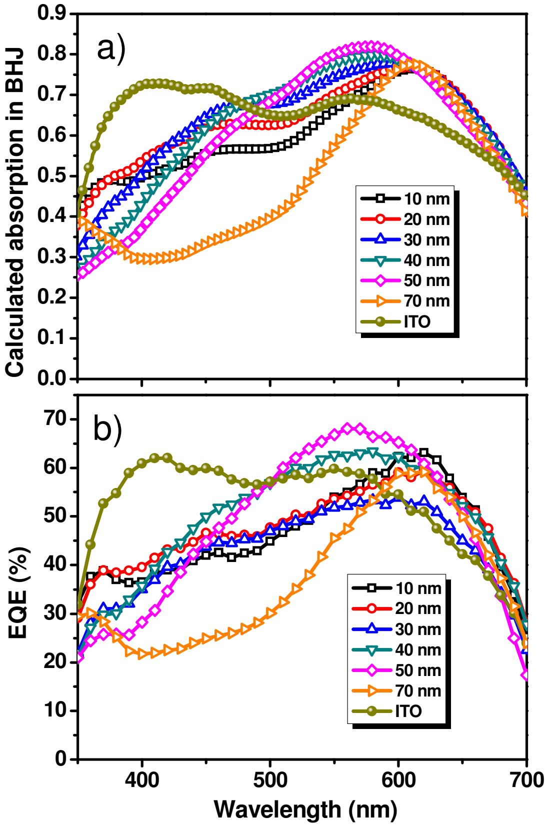

Figure 32 a) Fraction of the total incident light absorbed in the active layer (PIDT-PhanQ:$PC_{71}BM$), calculated by TMM and b) Experimental EQE of devices on ITO and TeO_2/Ag (12 nm). In both cases the thickness of TeO_2 varies from 10 to 70 nm.

Although in principle the TeO_2 film should not really affect the behavior of the cell because the Ag-Ag microcavity remains unchanged, the EQE data revealed that the resonant conditions in the microcavity could be affected by changing the TeO_2 thickness. Since multiple layers are involved in a PSC device, it requires a delicate balance between their dimensions to allow proper charge formation and transport, while keeping the transparent electrode with optimal transmittance and sheet resistance. As an external element with no specific role in the electrical dynamics of the cell, the TeO_2 film can be freely modified to facilitate light absorption to fully explore the potential of the system without affecting the operation of other elements in the cell.

2.3.6 Conclusions of section 2.3

In conclusion, enhanced light trapping and conductivity could be achieved by combining high refractive index TeO_2 with thin Ag film as hybrid transparent UTMF electrode. As a result, OPVs with performance higher than those with ITO electrode on both glass ($PCE_{TeO2/Ag}$ = 6.6 %, PCE_{ITO} = 6.5 %) and plastic ($PCE_{TeO2/Ag}$ = 5.8%, PCE_{ITO} = 5.6%) substrates could be achieved. The flexible devices on PEN/TeO_2/Ag also showed excellent bending stability compared to devices made from the ITO electrode. The EQE of these cells could be easily tuned by simply changing the thickness of the TeO_2 film, offering the possibility of further optimizing light absorption without affecting the electrical attributes of nanometric OPV devices.

2.4 High-Performance Semi-Transparent OPVs with Transparent Cathode Architecture [100]

Semi-transparent organic photovoltaic cells (STOPVs), an extension of OPVs which utilize transparent conductive materials as both electrodes, offer an extensive spectrum of applications such as power-generating windows for buildings and automobiles, foldable solar curtains, and other aesthetic architectural uses. Furthermore, the capability of converting incident light to electric power shows the potential of STOPVs in the field of efficient energy conservation.

When compared to small-molecule based STOPVs produced by vapor deposition or silicon-based STPVs [101], the development of solution processed polymer-based STOPVs is lagging due to the absence of efficient donor polymers and electrodes with proper transparency. STOPVs require more sophisticated materials and refined device engineering to simultaneously optimize both PCE and device transmittance, which are often contradictory to each other. In addition, for STOPVs to have practical solar window applications, good transparency perception (at least $\geq$ 20%) and color rendering properties are required under regular scene illumination [102]. To date, the state-of-the-art polymer-based STOPVs have either relatively low performance ($\leq$ 3%) or unsatisfactory average visible transmittance (AVT) and color purity [32, 103-106]. Therefore, there is a strong need to develop suitable polymer materials and novel device configurations to achieve improved PCE and transmittance for practical applications.

In order for a device to have high PCE and transmittance, in addition to proper color rendering index, it is critical to utilize appropriate thin BHJ layers that can efficiently harvest the proper spectrum of light and electrodes with high transmittance and electrical conductivity. Until now, the frequently reported STOPVs still use a rather thick (at least 100 nm) P3HT:$PC_{61}BM$ based BHJ layer. The dominant absorption of P3HT is located in the yellow-green wavelength region

(500 ~ 600 nm) where human eyes have the highest sensitivity, therefore leading to poor color perception and rendering properties [74, 105-109]. The optimal materials for solar window applications should have ample light absorption outside of regions where human eyes are the most sensitive; at the same time allowing transmittance of visible light extensively. As a result, polymers with a band-gap smaller than P3HT have become viable options for STOPVs [106]. Although these STOPVs show improved transparency perception for the human eye, the derived devices still exhibit only moderate PCEs of $< 3\%$ [32, 106]. Therefore, the search for proper materials still remains a significant challenge to achieve highly efficient polymer-based STOPV with suitable transparency and color perception [110].

In this study, highly efficient STOPVs were fabricated by synergistically combining an ultra-thin BHJ layer and a semitransparent electrode enabled by depositing thin silver Ag metal on top of a solution processed interfacial layer (C_{70}-bis). The efficient high-performance polymer PIDT-PhanQ (Figure 24) with dominant absorption beyond the orange-red wavelength region (> 600 nm), have shown high PCEs of over 6% in BHJ devices derived from this polymer with $PC_{71}BM$ [14, 66, 96]. After simulation and optical modeling (Figure 33 a–c) of numerous device configurations, it was found that the thickness of the PIDT-PhanQ:$PC_{71}BM$ BHJ layer could be further reduced to retain similar light-harvesting ability when Ag was used instead of Ca/Al as cathode.

2.4.1 Device Fabrication

The cleaning of substrates (glass/ITO) and device preparation was made using the same procedure followed in section 2.3.1 for ITO based devices but reducing the Ag anode thickness. Ca (30 nm) and Al (100 nm) or Ag (10 to 100 nm) were thermally evaporated under high vacuum ($< 2\times10^{-6}$ Torr) to serve as the cathode. The rate of Ag evaporation for STOPVs was 2 Å/s.

2.4.2 Experimental results

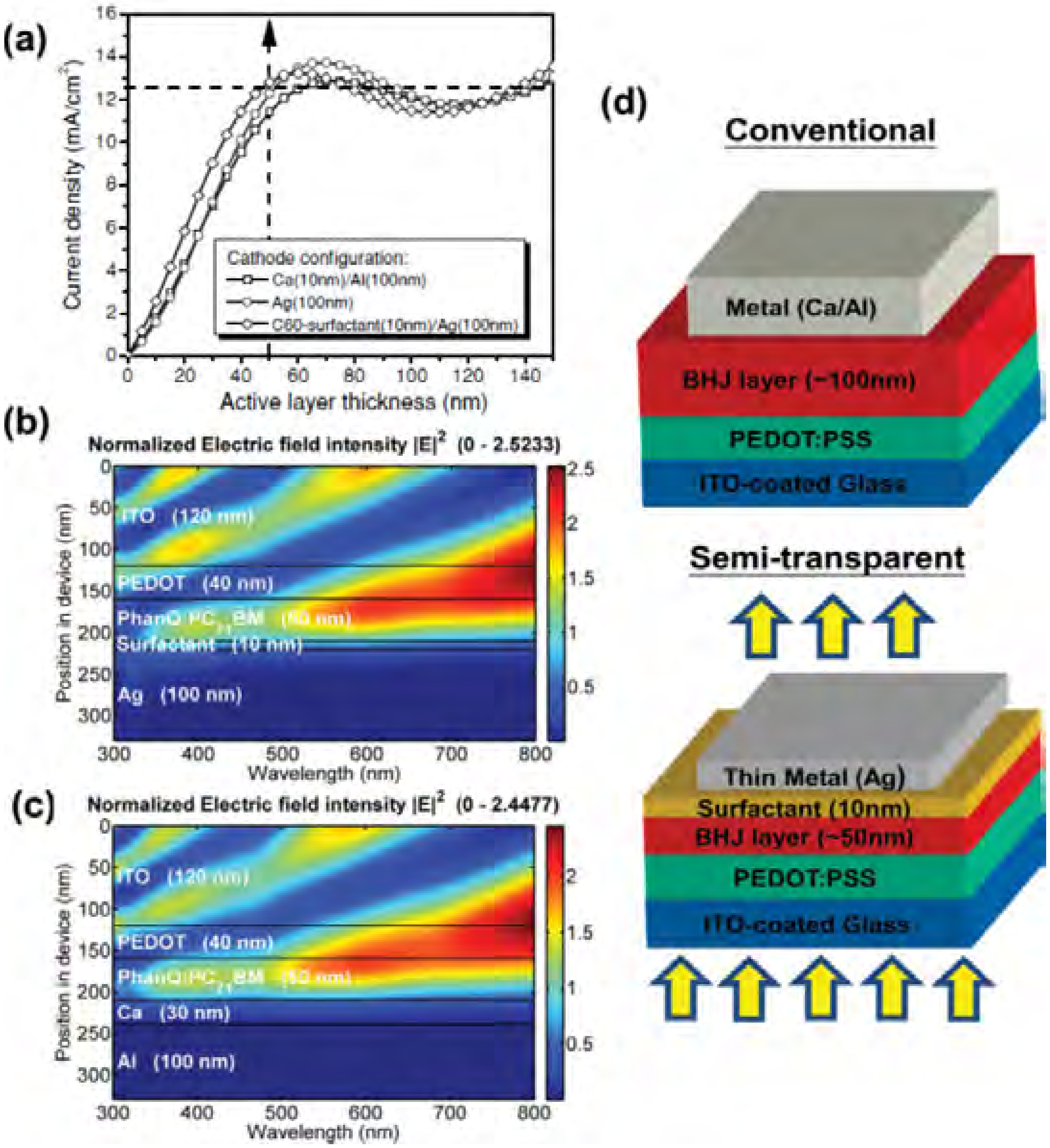

Figure 33 (a) The optical simulation of current density versus active layer thickness under different cathode configuration. Simulated field intensity profile $|E|^2$ normalized with respect to incoming field intensity at normal incidence as a function of wavelength for devices with (b) surfactant/Ag and (c) Ca/Al cathode configuration. (d) Device configuration of ultra-thin STOPVs.

The combination of surfactant and ultra-thin Ag as the hybrid cathode enhances the light absorption in the BHJ layer and improves the transmittance of the devices simultaneously as shown in Figure 33 a-c and Figure 34. Ag is chosen as the thin metal top electrode due to its intrinsically long skin-depth, which allows more photons to pass through the metallic layer, as shown in Figure 34 [76, 111-113]. In addition, it also improves the environmental stability of devices compared to the previously used Ca/Al cathode. This combination of material selection and device engineering facilitates the fabrication of STOPVs with good performance of 5.1% with a corresponding average visible transmittance (AVT) of ≈ 25%. Moreover, these devices also possess good color perception that is close to white light [74, 108, 109, 114].

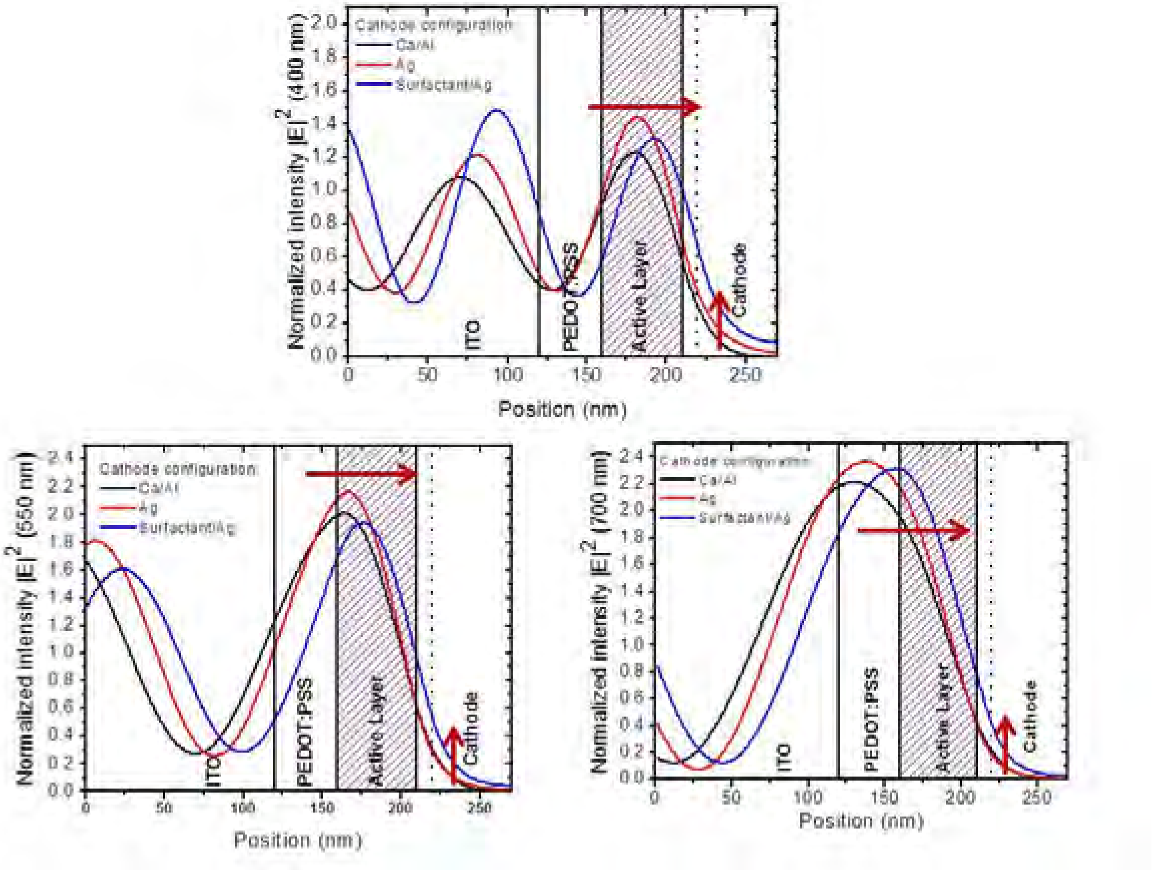

Figure 34 Simulated distribution profile for the optical field intensities in STOPVs, determined at wavelengths of 400, 550, and 700 nm. The layout of conventional structure is ITO (120 nm)/PEDOT:PSS (40 nm)/Active Layer (50 nm)/Ca (30 nm)/Al (100 nm), Ag (100 nm), and Surfactant (10 nm)/Ag (100 nm).

Even though transparent thin metal electrodes have been extensively exploited in organic optoelectronics [87, 95, 115-117], high resistance arising from electron scattering caused by discontinuous surface morphology of thin metal is still a known issue which severely limits device performance [87, 115, 118, 119]. Although numerous methods have been tried to alleviate this problem, such as the use of metal/Ag bilayer or metal in conjunction with metal oxides, it remains a big challenge to obtain a smooth Ag thin film with high optical transmittance and conductivity [87, 115, 117].

When depositing Ag on glass substrate, clusters tend to form during the thin film growth state which leads to rough surface and island-like discontinuous morphologies as illustrated in Figure 35 a) and b). These rough islands are unfavorable for charge transport and efficient charge extraction. Nevertheless, the morphology of evaporated ultra-thin Ag on surfactant-coated substrate is very smooth, as depicted in Figure 35 c) and d). This indicates that the fullerene-containing surfactant functions as a molecular seed layer that improves the thin film formation of Ag. This enhances the lateral film growth compared to the growth on bare glass substrate, especially when the thickness of the film is less than 20 nm [87, 95, 103, 104, 115, 116, 118-120]. The resulting Ag film on surfactant-coated surface shows much lower sheet resistance and better transparency in the visible spectrum, as summarized in Table 6.

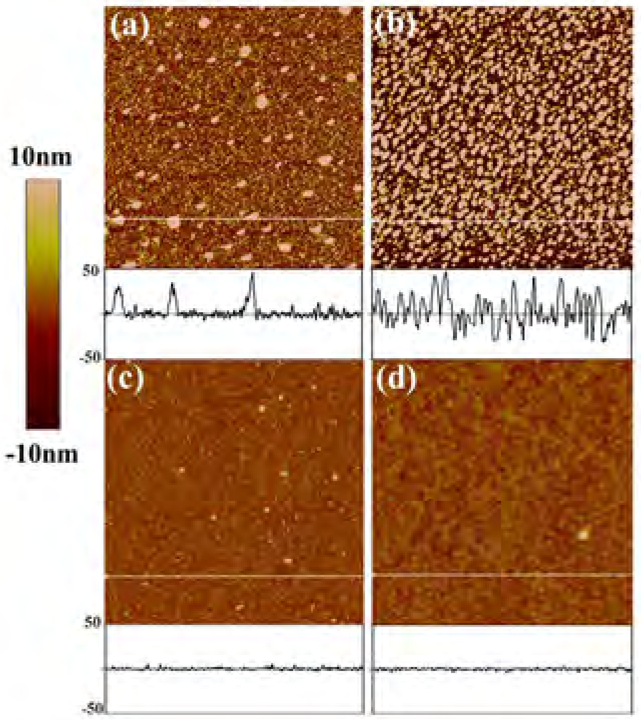

Figure 35 AFM images (5×5μm2) and surface profile (50 nm to -50 nm) of 10 nm thin Ag on (a) glass and (c) surfactant-treated glass, and 20 nm thin Ag on (b) glass and (d) surfactant-coated glass.

Table 6 The summarized photovoltaic parameters and average visible-light transmittance (AVT) of the conventional and semi-transparent devices.

Cathode Structure	V_{oc} (V)	J_{sc} (mA/cm^2)	FF (%)	PCE (%)	R_p ($\Omega \cdot cm^2$)	R_s ($\Omega \cdot cm^2$)	AVT (%) [a]
Conventional Structure							
Ca(30nm)/Al(100m)	0.85	10.83	65	6.12	1008.00	11.14	<0.05
Ag(100nm)	0.75	11.01	56	4.62	403.20	9.24	<0.05
Surfactant/Ag(100nm)	0.87	11.78	64	6.56	775.38	6.24	<0.05
Semi-transparent Structure							
Surfactant /Ag(10nm)	0.79	5.77	57	2.60	1120.00	24.59	30.18
Surfactant /Ag(20nm)	0.84	7.98	63	4.22	1008.00	9.14	31.71
Surfactant /Ag(30nm)	0.84	9.99	61	5.10	775.38	8.61	24.35
Surfactant /Ag(50nm)	0.85	10.69	62	5.63	775.38	7.75	13.03

[a] Visible light wavelength ranging from 380 to 740nm.

The original AVT of the thin Ag with a thickness of 50, 30, 20, and 10 nm on glass is 18, 40, 41, and 66%, respectively. By using the fullerene surfactant/Ag hybrid electrode (Figure 36), the AVT can be improved to 21, 44, 61, and 60%, respectively. The hybrid electrode has all the attributes needed to function as a novel efficient transparent cathode configuration, as can be seen from the better optical management, more effective electron collection, and seeding (nucleation) properties [5, 97].

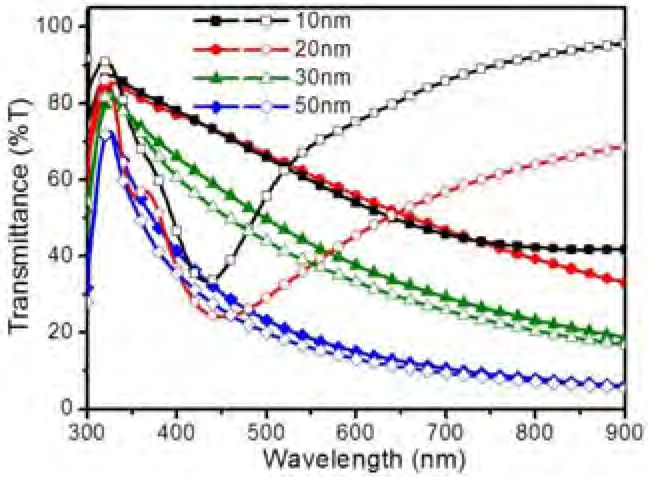

Figure 36 Transmittance of Ag films with different thickness over glass (hollow) and surfactant-treated glass (solid).

According to our optical model (Figure 33 a), a thin (~ 50 nm) of PIDT-PhanQ/$PC_{71}BM$ BHJ layer will have a similar light absorbing capability as a thicker one (~ 90 nm) if Ag, a more reflective material, is used to replace Ca/Al on top of fullerene surfactant. Three kinds of devices with different cathode configurations were fabricated to verify the superior light-harvesting property predicted. The detailed device characteristics including V_{oc}, J_{sc}, FF, and PCE are summarized in Table 6. The devices using Ag as cathode exhibited higher J_{sc} (11.01 and 11.78 mA/cm^2) than the one using Ca/Al (J_{sc} = 10.83 mA/cm^2). Since the fullerene surfactant can tune the work function of metals [97], the device with a surfactant/Ag cathode retains higher V_{oc} (0.87 V) and FF (64%) than the one using only Ag as cathode (V_{oc} = 0.75 V; FF = 56%). These results demonstrate the feasibility of combining the thin BHJ layer (~ 50 nm) of PIDTPhanQ:$PC_{71}BM$

and surfactant/Ag hybrid electrode to fabricate high-efficiency STOPVs. To test this hypothesis, devices employing the surfactant/Ag hybrid electrode with gradually decreased Ag thickness (from 50 to 10 nm) were fabricated. The control device with 100 nm thick Ag cathode was totally opaque as expected. The JV characteristics and the relevant parameters of devices are shown in Figure 37 a) and summarized in Table 6. These devices were able to preserve high V_{oc} and FF (V_{oc} = 0.84–0.85 V; FF = 61–63%) if the fullerene surfactant and thin Ag (20–50 nm) were used.

The decrease of V_{oc} and FF in these devices could be attributed to the increased resistivity of the thin Ag electrodes in these semi-transparent cells [76, 112, 113]. The series resistance (R_s) and the parallel or shunt resistance (R_p) are estimated from the slopes of the J–V curves at the points where V = 0 and V = V_{oc}. As shown in Table 6 and Table 7, both the sheet resistance (R□) and series resistance (R_s) of the devices increase as the Ag thickness decreases, especially for the 10 nm Ag thickness. As expected, the R□ and R_s of devices with a 10 nm thick Ag cathode increased to 92.33 Ω/□ and 24.59 $\Omega\cdot cm^2$, respectively. Subsequently, the V_{oc} and FF decreased to 0.79 V and 57%. As the thickness of the Ag was increased from 20 to 50 nm, the R□ and R_s ranged from 7.15 to 1.7 Ω/□ and 9.14 to 7.75 $\Omega\cdot cm^2$, respectively. This improved resistance remarkably reduced the loss of V_{oc} and FF.

Meanwhile, there was a slight decrease in J_{sc} (7.98–10.69 mA/cm^2) compared to the control device. The decreased J_{sc} of these STOPVs can be attributed to the reduced reflectivity of the thin semi-transparent hybrid cathode and the lower light intensity within the active layer, as shown in Figure 38. The optical field distribution shown in Figure 38 clearly illustrates the tradeoff between absorption and transmittance. Despite the loss of current density in the thinner cathode device, the ultra-thin PIDT-PhanQ:$PC_{71}BM$ BHJ layer could still provide a reasonable J_{sc} of 7.98 and 9.99 mA/cm^2 for devices with 20 and 30 nm Ag used for hybrid cathode.

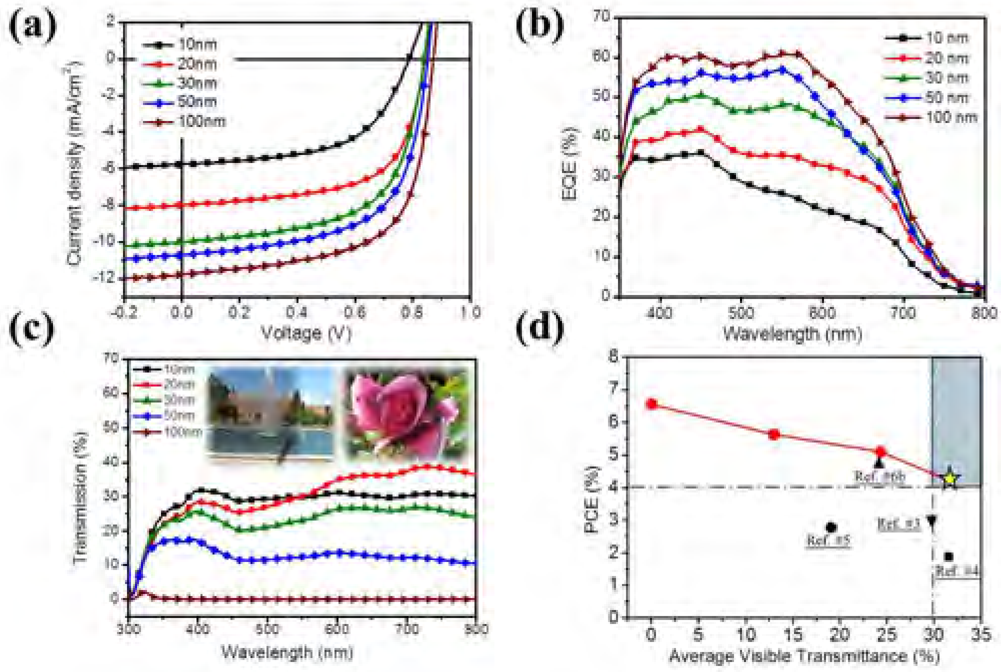

Figure 37 (a) JV curves and (b) EQE spectra of the traditional/semi-transparent devices made with various thickness of Ag as the cathodes measured under illumination (simulated AM1.5G) at 100mWcm-2. (c) The transmission spectra of the corresponding STOPVs, (inset) examples of the appearance of objects when looking through our STOPV devices. (d) The performance of the corresponding STOPVs versus AVT with several important representative results reported in the literature.

Table 7 Sheet resistance (R□) of thin Ag films on different substrates.

Thickness (nm)	R□ (Ω/□)		
	on glass[a]	on surfactant-treated glass	on complete device
10	O.F	92.33	15.03[b]
20	O.F	7.15	4.80
30	O.F	4.20	3.14
50	1.89	1.70	1.65

[a] O.F: Overflow; [b]This value might contribute from ITO.

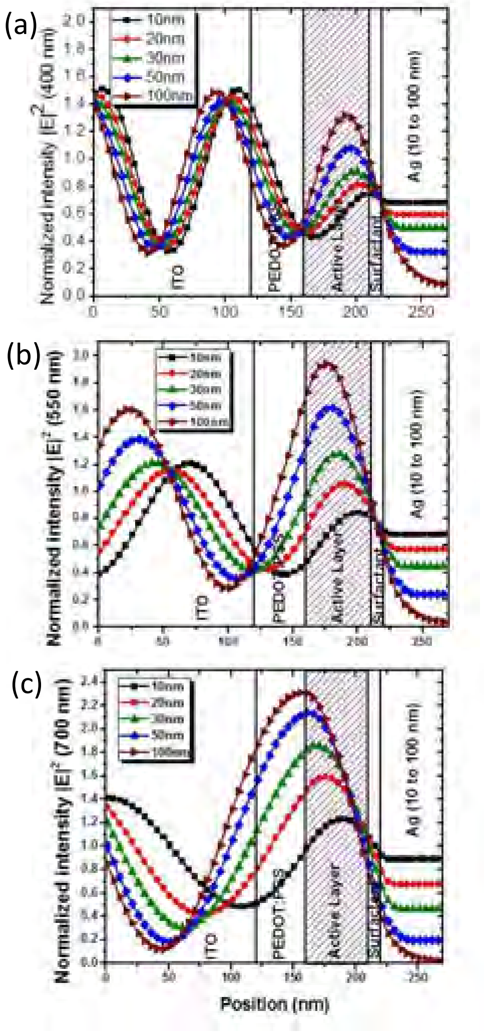

Figure 38 Simulated distribution profiles for the optical field intensities in the studied STOPVs, determined at wavelengths of 400, 550, and 700 nm. The layout of conventional structure is ITO (120 nm)/PEDOT:PSS (40 nm)/Active Layer (50 nm)/Ag (10 to 100 nm).

By taking advantage of the high transmittance hybrid cathode, highly efficient STOPVs had been successfully demonstrated. The J_{sc} of these devices were confirmed by measuring their EQE (Figure 37 b). Notably, after taking into account the different absorption in the active layer, based on the optical simulator, the calculated IQE of the studied STOPVs are all quite similar as shown in Figure 39. It verifies that parasitic absorption in the metal and the reflections toward the light source do not influence the IQE. The combined results from EQE and IQE spectra proved that the design of the cathode is crucial for balancing the absorption and transmittance trade-off in STOPVs. These results also confirmed the advantages of using surfactant/Ag cathodes to simultaneously improve electron extraction and optical field redistribution within the devices.

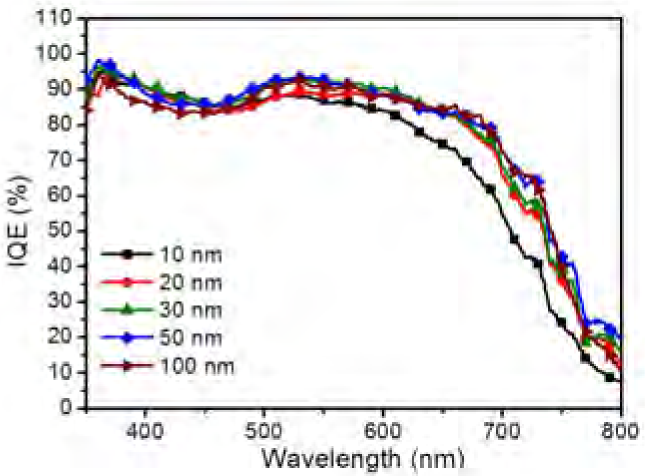

Figure 39 Calculated internal quantum efficiency (IQE) of the studied STOPVs.

The transmission spectra of these STOPVs are presented in Figure 37 c. The AVT of the devices with 50, 30, 20, and 10 nm hybrid cathodes are 13.03 %, 24.35 %, 31.71 %, and 30.18%, respectively. This shows that the transparency of the hybrid cathode compensates for the lower absorption in the active layer, leading to overall moderate device transmittance. Interestingly, the device with the thinner hybrid cathode (10 nm Ag) showed an even lower AVT than the one with 20 nm Ag. This may be caused by the similar remnant scattering effect observed in the 10 nm bare Ag surface shown in Figure 36 [114, 117].

The two photos shown in the Figure 40 were taken through the STOPVs studied in this paper. These photos show high resolution and good color-purity (PCE = 4.2%, AVT ≈ 32%) based on the transparent surfactant/20 nm Ag hybrid cathode and thin BHJ layer. To evaluate the transparency perception of the above STOPVs in human eyes, the tristimulus value (X,Y,Z) and the color coordinates (x,y) were calculated from the transmission spectra while the incident light source was replaced with the AM 1.5 spectrum. The color coordinates of the studied

STOPVs with different thickness of Ag on CIE 1931 chromaticity diagram are illustrated in Figure 40. The corresponding coordinates of the devices derived from 10, 20, 30, and 50 nm hybrid cathode are (0.336, 0.343), (0.359, 0.355), (0.353, 0.350), and (0.341, 0.342), respectively. All these STOPVs showed very nice transparency color perception that is close to white light (0.33, 0.33).

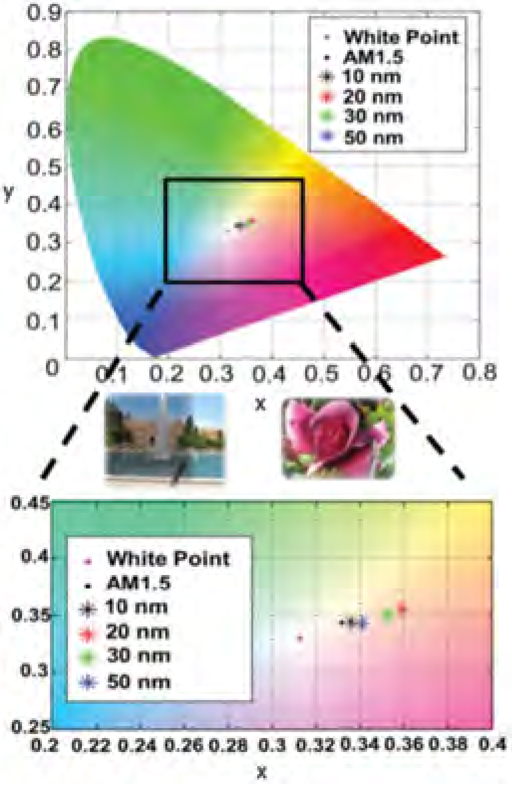

Figure 40 (Top) The representation of color coordinate of the studied STOPVs with different thickness of Ag on CIE 1931 xyY chromaticity diagram. (Bottom) The enlarged color space of the relevant part of the CIE 1931 xyY diagram. All STOPVs are folded with an AM1.5 solar spectrum to calculate the color characteristics. Inset in between: Two digital photographs taken through the semitransparent OPVs incorporating a 20-nm-thick Ag layer.

2.4.3 Conclusions of section 2.4

In summary, we have demonstrated a novel polymer-based STOPV by incorporating an ultra-thin BHJ layer (≈ 50 nm) based on a blend of PIDT-PhanQ with superior light-harvesting abilities and $PC_{71}BM$ along with highly transparent hybrid cathode based on a solution-processed interfacial layer and ultra-thin Ag films. These polymer-based STOPVs exhibited good PCE and AVT with neutral color perception close to that of white light. This result shows great promise for polymer-based STOPVs for solar windows in future green buildings.

2.5 Semi-transparent polymer solar cells based on PBDTTT-C-T and analysis of window application [110]

The feasibility of realizing semi-transparent device structures shows promise for their use in novel applications. Semi-transparent OPV cells are important building blocks for multijunction or tandem devices, which comprise semitransparent front sub-cells stacked with back sub-cells that have a complementary spectral response which acts to enhance sunlight harnessing and device performance. For this purpose, a major amount of the studies on STOPVs have been devoted to the development of transparent electrodes [74, 105, 109, 121-123] as a key step toward the realization of high efficiency tandem organic solar cells. Moreover, STOPVs have been identified as promising candidates for power-generating window applications because they can be integrated with conventional transparent elements such as building and automobile glasses. Building integration is particularly interesting since buildings have large surface areas for harnessing sunlight and have been recognized as one of the major energy consumers and carbon emitters. Therefore, generating clean energy on site from buildings with integrated low-cost photovoltaics could potentially reduce the expense of energy and mitigate the pollution on an appreciable scale.

Though colored windows are useful for aesthetic and decorative purposes, windows with limited chromatic alternations of the light source are generally preferred. They allow a natural color spectrum for environments in which the quality of the illumination is important. The fast development of novel organic photovoltaic materials [124, 125] over the past years can be leveraged in realizing highly efficient STOPV cells with desirable optical effects. However, systematic study and optimization of the optical properties of STOPVs for window integration are scarce and have just started to be performed.

Ameri et al. [106] suggested that STOPVs based on poly[2,6-(4,4-bis-(2-ethylhexyl)-4H-cyclopenta[2,1-b;3,4-b']dithiophene)-alt-4,7-(2,1,3-benzothiadiazole)] (PCPDTBT) and a [6,6]-phenyl-C71-butyric acid methyl ester ($PC_{71}BM$) blend can provide a more natural transparency color perception than the solar cells based on a P3HT:$PC_{71}BM$ blend. Colsmann et al. [32] demonstrated that STOPVs based on the blend of $PC_{71}BM$ and poly[(4,4'-bis(2-ethylhexyl)dithieno[3,2-b:2',3'-]silole)-2,6-diyl-alt-(2,1,3-benzothiadiazole)-4,7-diyl] (PSBTBT) are suitable candidates for window applications due to the remarkable transparency color perception and color rendering capacity afforded by the transmitted light. However, further breakthroughs, especially in the performance of STOPVs, rely on the use of more advanced materials and conscious optical engineering.

In this study we developed high-performance STOPVs in the inverted structure comprising blends of PBDTTT-C-T (Figure 41) [15], which is a low bandgap polymer based on thieno[3,4-b]thiophene (TT) and benzo[1,2-b:4,5-b']dithiophene (BDT) alternating units with $PC_{71}BM$, as the active material. By tuning the thickness of the reflective metal electrode, the power conversion efficiency (PCE) of the semi-transparent devices ranges from 7.56% to 4.25% with the corresponding transparency ranging from 2% to 36%. The transmitted light of these devices under the air mass 1.5 global (AM1.5G) illumination also exhibits extraordinary transparency color perceptions and rendering capacities, favoring the use of PBDTTT-CT:$PC_{71}BM$ based semi-transparent solar cells for real-life window applications.

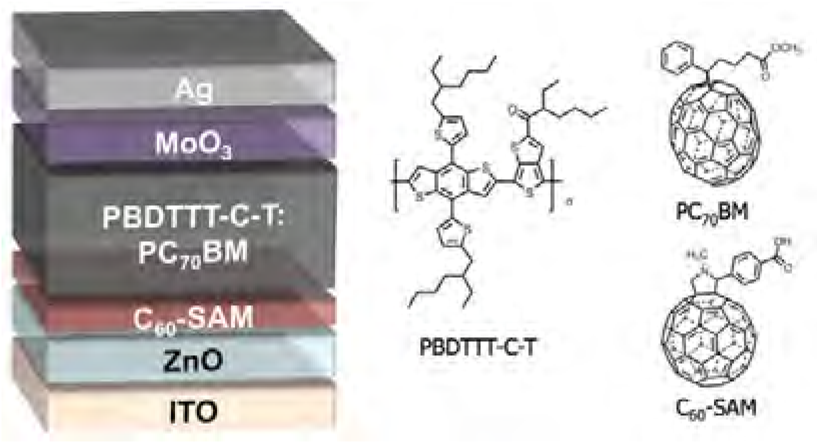

Figure 41 Device architecture of inverted cells and the chemical structures of the active materials PBDTTT-C-T and $PC_{71}BM$ and the self-assembled molecule C_{60}-SAM.

2.5.1 Device fabrication

In this work, we have fabricated semi-transparent inverted devices based on PBDTTT-C-T and $PC_{71}BM$ as active materials to explore their potential for window applications. The inverted architecture is known to have several advantages over the conventional architecture such as improved stability and compatibility with roll-to-roll processes [126, 127]. The layout of the device architecture is shown in Figure 41. The fabrication processes of the STOPV cells are described as follows. PBDTTT-C-T (10 mg/ml) and $PC_{71}BM$ (15 mg/ml) were dissolved in dichlorobenzene solution with 3 vol.% of 1,8-diiodooctane (DIO) as the solvent additive. Pre-cleaned ITO coated glass substrates (see section 2.3.1.1) are sequentially spin-coated with ZnO sol–gel, a C_{60} based self-assembled monolayer (C_{60}-SAM, Figure 41), and the PBDTTT-C-T:$PC_{71}BM$ active layer. Finally, MoO_3 (5 nm) and the Ag anode with variable thickness (t_{Ag}= 0–60 nm) are thermally evaporated through patterned masks, defining the nominal area of the devices to be 10.08 mm^2.

2.5.2 Experimental results

The inverted STOPV cells exhibit a grayish or neutral color appearance due to the complementary and balanced absorption from the PBDTTT-C-T polymer and $PC_{71}BM$ over the visible spectrum. Figure 42a demonstrates the transmission spectra of the solar cells with varying Ag thickness (open symbols) obtained via UV-Vis-NIR spectroscopy. The transmission curve of an Ag electrode free sample (t_{Ag} = 0 nm) is also taken for comparison. The average visible transmittance (AVT), or the average of the transmittance of the solar cells in the visible region (370–740 nm), of the semi-transparent devices are presented in Table 8. As the thickness of the reflective Ag electrode varies from 6 nm to 60 nm, the AVT can be tuned accordingly from ≈ 35.9% to ≈ 2.0%, showing the flexibility of transparency management through electrode thickness control. Though the required transparency for windows depends on the working environment, it is generally considered that an AVT of 25% is the benchmark for window applications [128]. In addition, we also show that the AVT of the device without Ag (t_{Ag} = 0 nm) is around 50%. Figure 42b and c demonstrate viewing through the STOPV devices of different transparencies.

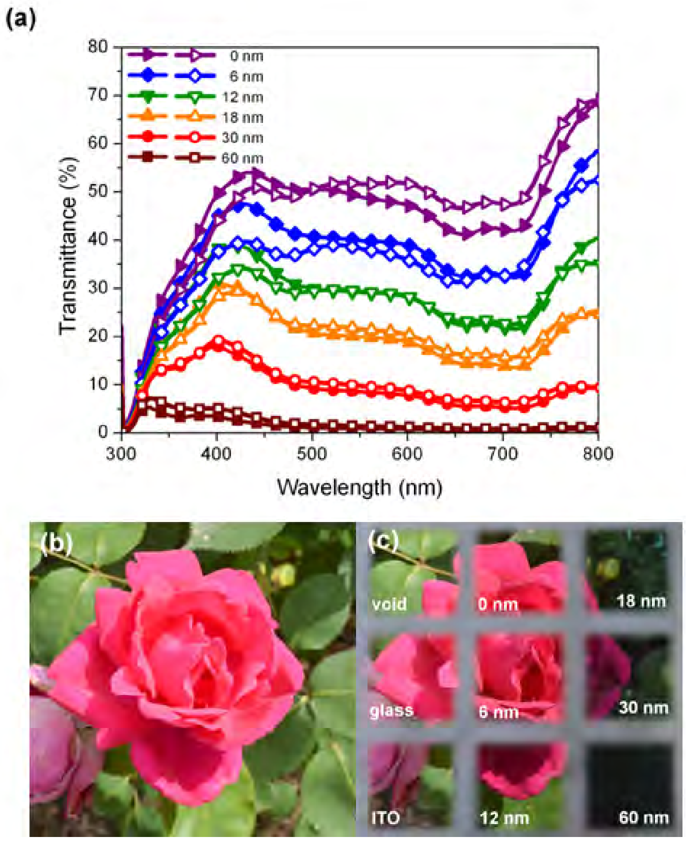

Figure 42 (a) Transmission spectrum of the STOPVs from optical modeling (closed symbols) and the real devices (open symbols). (b and c) Photographs of a pink rose taken with exactly the same camera settings (shutter, aperture, white balance, etc.) on a sunny day. Photograph (c) was taken through semi-transparent devices with the six different Ag thicknesses and blank ITO and glass substrates.

Table 8 Optical properties of the semitransparent devices.

Ag thickness (nm)	AVT (%)	HPT (%)	CIE 1931 (x,y)	CCT (K)	$\lvert\Delta_{uv}\rvert$	General CRI
60	2.0	1.4	(0.2650, 0.2617)	15894	3.90×10^{-3}	94.8
30	10.6	9.5	(0.2917, 0.3010)	8390	3.98×10^{-5}	96.7
18	21.3	21.1	(0.3091, 0.3227)	6764	1.76×10^{-3}	97.3
12	27.9	28.9	(0.3187, 0.3351)	6156	3.34×10^{-3}	96.8
6	35.9	37.3	(0.3225, 0.3442)	5943	6.11×10^{-3}	96.3
0	48.7	51.3	(0.3323, 0.3478)	5507	3.44×10^{-3}	98.0

Device JV measurements were performed under a nitrogen atmosphere with simulated AM1.5 global solar irradiation at 1 Sun intensity (100 mW/cm^2), and the EQE was recorded with a lock-in-amplifier under chopped monochromatic illumination in an ambient environment. Figure 43 and Figure 44 show the JV curves and the external quantum efficiencies (EQE) of the semi-transparent PBDTTT-CT:PC$_{71}$BM devices with different t_{Ag} values, respectively. The sheet resistance ($R_□$) of thin Ag electrodes is characterized using four-point probe measurements on independent samples of Ag films with the same thickness of devices deposited on a 50 nm layer of MoO_3 on glass substrates. Thin Ag films on the MoO_3 substrates have shown $R_□$ values comparable to those of common ITO substrates. A summary of device characteristics can be found in Table 9.

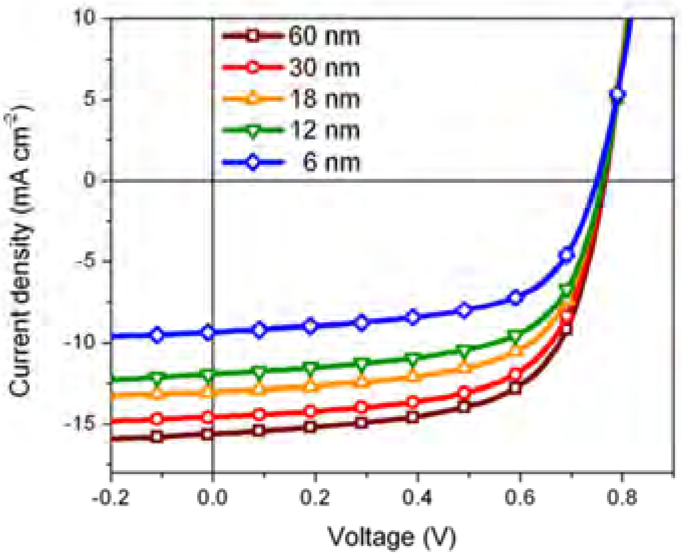

Figure 43 J-V characteristics of the semitransparent devices with different thicknesses of the silver metal electrode under AM1.5G illumination at 100 mW/cm^2.

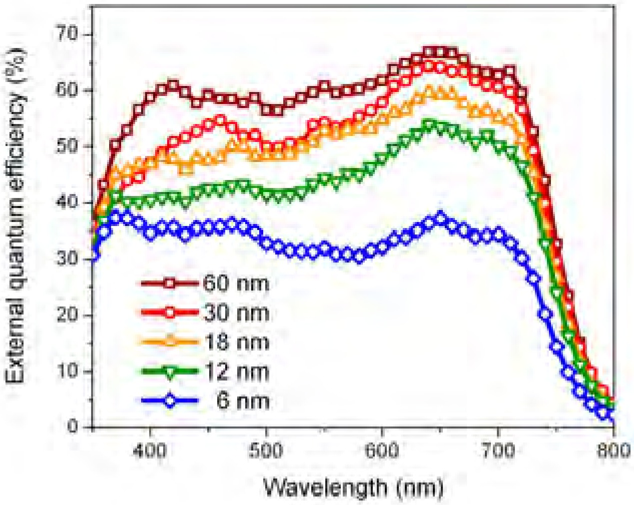

Figure 44 External quantum efficiency of the STOPVs.

Table 9 Electrical characteristics of the semitransparent solar cells.

Ag thickness (nm)	V_{oc} (V)	J_{sc} (mA cm^{-2})	FF	PCE (%)	R_s (Ω cm^2)	R_p (Ω cm^2)	R□ (Ω/□)
60[a]	0.77 (0.76)[b]	12.13 (12.21)	0.61 (0.57)	5.69 (5.34)	6.4	540.4	1.1
60	0.77 (0.76)	15.64 (15.09)	0.64 (0.63)	7.56 (7.21)	5.4	540.4	1.1
30	0.76 (0.76)	14.54 (14.37)	0.64 (0.62)	7.05 (6.84)	5.7	766.5	3.4
18	0.76 (0.76)	13.01 (12.99)	0.63 (0.62)	6.22 (6.10)	6.4	740.0	8.3
12	0.76 (0.76)	11.94 (11.75)	0.62 (0.62)	5.62 (5.50)	6.4	547.7	12.3
6	0.75 (0.75)	9.33 (9.25)	0.61 (0.61)	4.25 (4.19)	9.2	668.4	8.8×10^8

[a] Device without C_{60}-SAM modification at the ZnO/active layer interface.

[b] Numbers in parentheses indicate the average values.

The least transparent STOPV device (t_{Ag} = 60 nm, AVT = 2%) shows excellent device performance (J_{sc} = 15.64 mA/cm^2, PCE = 7.56%), comparable to the inverted device based on PBDTTT-C-T:$PC_{71}BM$ reported by Li et al [129]. High performance STOPVs are obtained by optimizing the interfacial property of the devices [130, 131]. We found that the modification of the ZnO/active layer interface with the C_{60}-SAM is crucial in our case for optimal device performance. Devices without SAM modification at the ZnO/active layer interface are found to be significantly less efficient; about 20% lower PCE is observed for the device (t_{Ag} = 60 nm) without the C_{60}-SAM modification as shown in Table 9. The C_{60}-SAM has been shown to improve the electron extraction at the interface [126, 132].

The performance of the solar cells is plotted against the AVT and displayed in Figure 45. It can be observed that the AVT and the device performance oppose each other nearly linearly, which clearly shows the tradeoff between the transparency and photon collection. The performance of several representative STOPVs [32, 104-106] reported earlier is also displayed in Figure 45 for comparison. Note the semi-transparent devices based on PBDTTT-C-T:$PC_{71}BM$ show significantly improved performance compared to other STOPVs with similar transparencies. Furthermore, the devices with t_{Ag} = 12 and 18 nm are particularly attractive among the data points since they have presented very practical AVTs between 21% and 28% with excellent PCEs of 6.2% to 5.6%.

2.5.3 Optical perception by the human eye

The visual appearances of the semi-transparent solar cells perceived by human eyes are also key properties in determining their suitability for applications. Due to the spectrally dependent response of the human eyes, the human perception of color and transparency may vary from the experimental values acquired from the machine. For example, the human perception of transmittance (HPT) of semi-transparent solar cells based on P3HT:$PC_{71}BM$ is distinctly lower than its AVT [106]. Therefore, we analyze the effect of the response of the human eyes by calibrating the transmission spectra of the STOPVs with the human eye sensitivity (the y color-matching function) following the procedure reported by Ameri et al [106]. The analysis shows only small differences between the HPT and AVT of our STOPV devices as summarized in Table 8, which can be attributed to the balanced absorption of the PBDTTT-C-T:$PC_{71}BM$ blend over the visible range as revealed in the transmission spectra. The trivial difference between the AVT and HPT suggest that our STOPV cells act similarly to neutral density filters, which is ideal for window applications.

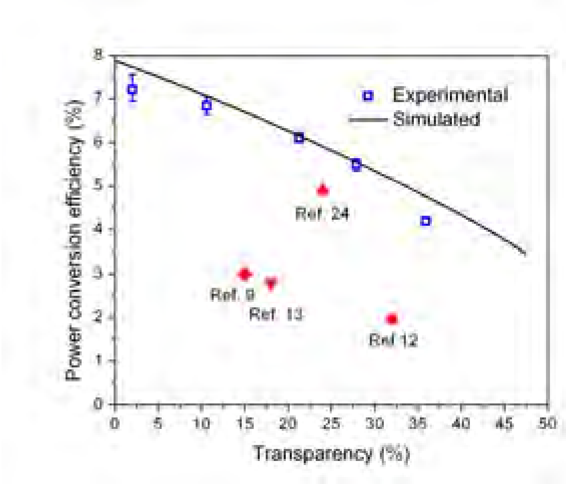

Figure 45 Experimental (blue markers) and simulated (black line) relationships between the power conversion efficiency and the transparency of the semitransparent devices. Representative semi-transparent OPV devices reported earlier are also displayed for comparison (red markers).

The transparency color perceptions of the STOPVs are depicted using the CIE 1931 chromaticity diagram (xyY), which is specifically designed to represent the colors perceptible to the human eyes. The transmitted light is represented by the product of the AM1.5G solar spectrum and the transmission spectrum of each semi-transparent device, and the corresponding color coordinates CIE 1931 (x,y) are summarized in Table 8. The representation of the color coordinates of the STOPVs are also displayed in the CIE 1931 chromaticity diagram in Figure 46. The color coordinates of the STOPV devices with thin Ag electrodes ($t_{Ag} = 30$ nm) are located in the low colorfulness area in the CIE chromaticity diagram, indicating good achromatic or neutral color sensations when looking through the devices under AM1.5G illumination. The transmitted light through the device with $t_{Ag} =$ 12 nm and $t_{Ag} =$ 18 nm show color coordinates particularly close to the standard daylight illuminant D65 $(x_{D65}, y_{D65}) = (0.3128, 0.3290)$ at $(x_{Ag12}, y_{Ag12}) = (0.3187, 0.3351)$ and $(x_{Ag18}, y_{Ag18}) = (0.3091, 0.3227)$, respectively, capable of providing extremely high quality illumination with achromatic sensation. The color coordinates move in the direction of the blue corner of the CIE chromaticity diagram as the Ag electrode gets thicker, but overall the color coordinates of the STOPVs suggest transparency color perceptions of neutral colors from the transmitted light with very little color bias caused by the PBDTTT-C-T:$PC_{71}BM$ based semi-transparent solar cells, which is also illustrated in Figure 42c where the background colors (pink flower and green leaves) were only slightly altered by the semi-transparent devices.

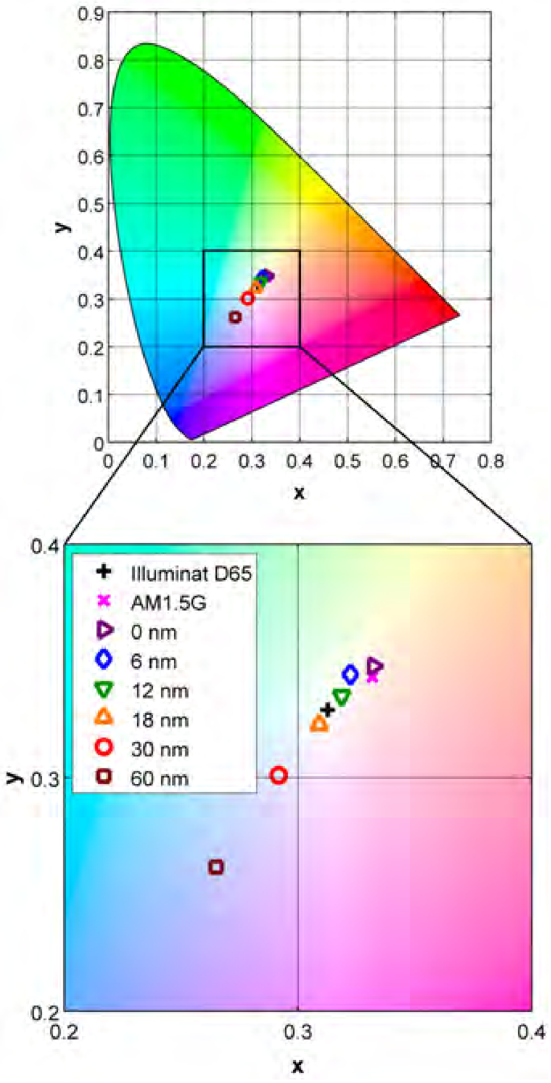

Figure 46 Representation of the color coordinates of the STOPV devices with different thickness of Ag electrode under AM1.5G illumination on the CIE chromaticity diagram xyY (1931) and the enlarged image. The color coordinates representation of D65 standard daylight illuminant and AM1.5G illumination are also presented.

2.5.4 Color rendering capacity

To this point we have demonstrated that the transmitted lights of semi-transparent BDTTT-C-T:$PC_{71}BM$ OPV devices under AM1.5G illumination are good metamers, or dissimilar spectral distributions that produce the same color sensation, to nearly white light illuminants. However, white light illuminants do not necessarily provide appropriate color rendering capacities. Therefore, we further evaluate the color rendering indices (CRIs) of the transmitted light of the STOPV cells.

Transforming the CIE 1931 (x,y) coordinates of the devices to the UCS CIE 1960 (u,v) color space, the new coordinates are displayed in Figure 47. The CCTs of the points and their corresponding distances to the Planckian locus (Δ_{uv}) are calculated from the UCS coordinates and summarized in Table 8. Notably, all points are very close to the Planckian locus with all $|\Delta_{uv}|$ less than 0.05, indicating the transmitted light of all devices are all close to those of blackbody radiators.

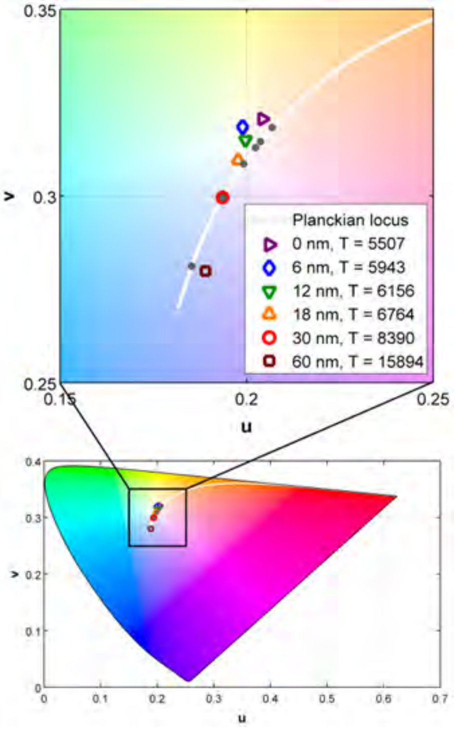

Figure 47 Planckian locus and the UCS coordinates CIE 1960 (u,v) of the semi-transparent STOPV devices. The gray dots represent the nearest Planckian radiators.

Before applying the test sample method, the transmission spectrum of any of the semitransparent devices was folded first with the AM1.5 spectrum, using the resultant spectrum as illuminant for the color samples TCS01-08. The general CRIs of the transmitted light of all the STOPVs are listed in Table 8, the special CRIs are listed in Table 10.

Table 10 Special color rendering indices (CRIs) of the transmitted light of the STOPV devices under AM1.5G illumination.

	0 nm	6 nm	12 nm	18 nm	30 nm	60 nm
CRI TCS01	97.7	96.2	96.3	97.5	97.9	97.6
CRI TCS02	98.7	97.6	97.6	97.8	96.8	94.8
CRI TCS03	99.5	99.3	98.9	98.3	96.0	91.2
CRI TCS04	98.2	97.1	97.1	97.7	96.6	93.0
CRI TCS05	98.1	96.7	96.9	98.0	98.4	98.2
CRI TCS06	98.8	97.5	97.5	97.6	96.5	94.5
CRI TCS07	98.1	97.9	97.2	97.2	96.2	93.7
CRI TCS08	95.1	93.9	93.1	94.6	95.5	95.6

The CRIs of all our functional devices are close to 100. To the best of our knowledge, these are the highest general CRI values ever reported for STOPVs. The UCS points of a representative semi-transparent OPV device ($t_{Ag} = 12$ nm), the nearest Planckian locus point, and the color samples under both the tested and the reference illumination are plotted in Figure 48. As implied by the excellent general CRIs, the color point corresponding to the STOPV cell is almost superimposed on the nearest point on the Planckian locus. Similarly, the corresponding sample color points under both kinds of illuminations are nearly superimposed, clearly demonstrating the exceptional color rendering properties of this system.

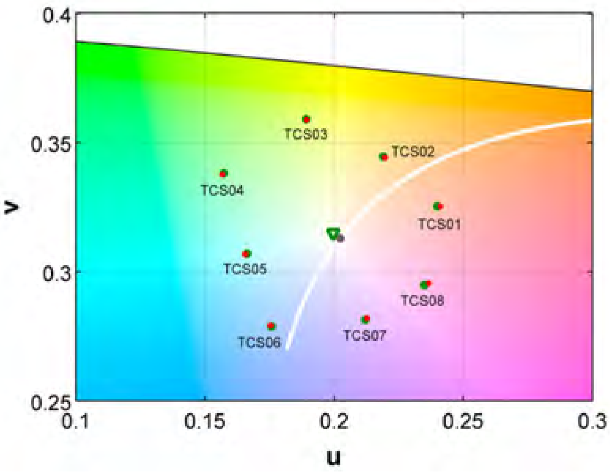

Figure 48 Determination of the color rendering index of the semi-transparent STOPV device with 12 nm Ag electrode. The central green triangle represents the transmitted light of the PBDTTT-C-T:PC$_{71}$BM STOPV solar cell under AM1.5G illumination. The surrounding green dots correspond to the TCS01–08 illuminated by the transmitted light of the STOPV cell under AM1.5G illumination. The red dots represent the TCS01–08 illuminated by the reference Standard Illuminant D of CCT = 6156 K.

2.5.5 Optical simulations

In order to investigate and exploit the full potential of this system, particularly concerning the limitation of transparency imposed on the highest achievable efficiency, optical simulations of the STOPV cells were performed. The optical model comprises 120 nm of ITO, following by 33 nm of sol–gel ZnO, 90 nm of the PBDTTT-C-T:PC$_{71}$BM (1:1.5 w/w) active layer, 5 nm of MoO$_3$, and finally an Ag layer with variable thickness. The electric field intensity profiles of two representative STOPVs (t_{Ag} = 12 nm and 60 nm) can be visualized in Figure 49.

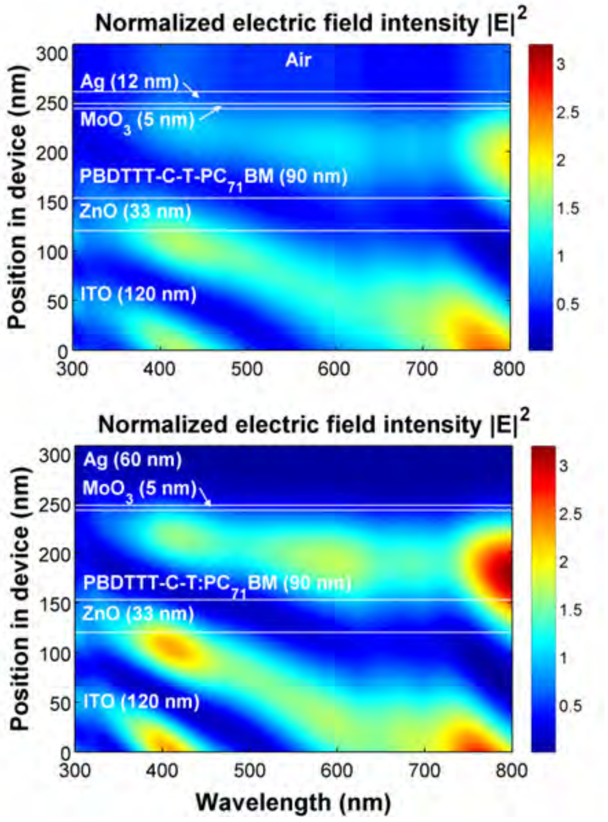

Figure 49 Simulations for the electric field intensity profile in the studied semi-transparent OPV devices with 12 nm (top figure) and 60 nm (bottom figure) of Ag electrode.

A higher intensity of electric field distributed in the device with a thicker Ag electrode is observed, as expected, due to less transmitted photon loss. From the electric field distributions, simulated transmission curves of the STOPVs are derived and compared with the experimental curves in Figure 42. We note that the simulated curves are in exceptionally good agreement with the experimental curves, confirming the validity of the model.

For the devices with 12 nm and 60 nm Ag electrodes exciton generation rates are presented in Figure 50. It can be observed that the excitons are generated efficiently over the visible regime, which explains the effectiveness of photocurrent generation from the PBDTTT-C-T:PC$_{71}$BM system.

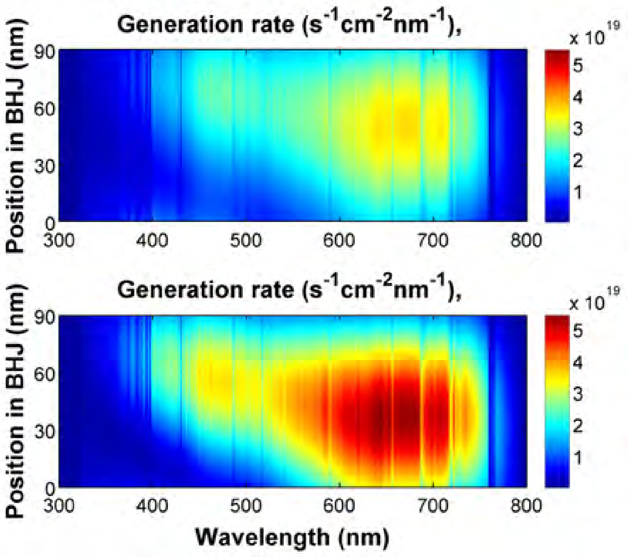

Figure 50 Simulations of exciton generation rate in the studied STOPV devices with 12 nm (top figure) and 60 nm (bottom figure) of Ag electrode.

Figure 51 plots the exciton generation rate against the continuous change of t_{Ag} (0–100 nm). The trend indicates that the generation rate is fairly sensitive to the change of t_{Ag} when t_{Ag} is small starting with a close to linear increment as Ag begins to build up, doubles at $t_{Ag} \approx 25$ nm, and finally reaches a plateau when $t_{Ag} > 65$ nm. The monotonic enhancement of generation rate upon the application of the reflective electrode in the PBDTTT-CT:$PC_{71}BM$ inverted cell explains the effectiveness of tuning the transparency through control of the thickness of the metal electrode.

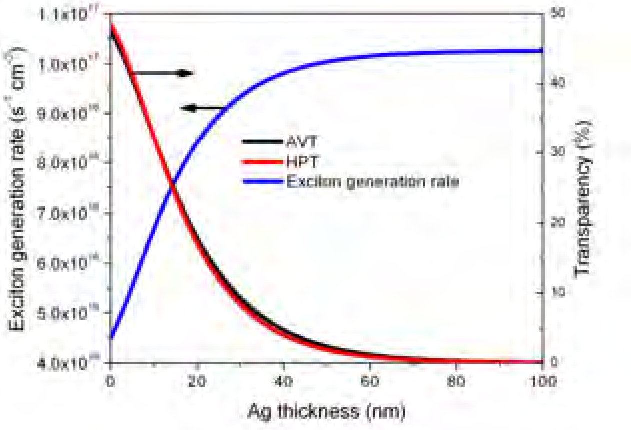

Figure 51 Dependence of the exciton generation rate to the thickness of the Ag electrode from optical modeling (blue curve). The dependence of the average visible-light transmittance (AVT, black curve) and human perception of transmittance (HPT, red curve) of devices simulated from the optical model at various Ag thicknesses are also displayed.

Interestingly, the observation is very different from the simulation of semi-transparent inverted P3HT:$PC_{71}BM$ device performed by Ameri et al. [106], where applying a 100 nm opaque reflective electrode to the device only results in relatively mild enhancement of the generation rate (N_{ph} as presented by Ameri et al.). We attribute the difference between the two systems to the optical effect of the hole-transporting layer. By replacing the 5 nm MoO_3 in the optical model with 100 nm PEDOT:PSS as used in the P3HT:$PC_{71}BM$ inverted solar cell, we observed that the difference of generation rate between devices with and without the 100 nm Ag electrode becomes insignificant (data not shown). Figure 51 also shows the simulations of AVT and HPT at various Ag thicknesses. Again, the figure reveals that HPT is almost identical to AVT at every thickness of Ag.

From the simulation, we can also estimate the relationship between the highest achievable PCE and transparency by using $J_{sc-100\%}$, Voc = 0.76, and FF = 0.63. The calculation establishes a nearly linear relationship between the highest achievable PCE and the AVT (Figure 45), which fits the experimental data almost quantitatively. This relationship makes it possible to build devices with predictable performance and transparency. The success of the optical simulations in portraying the behavior of the PBDTTT-C-T:PC$_{71}$BM system indicates their usefulness in designing or engineering future STOPV systems.

2.5.6 Conclusions of section 2.5

We have demonstrated high efficiency semi-transparent OPV cells with significantly improved performance compared to other STOPVs of similar transparency. The STOPV devices under AM1.5 illumination provide close to white or achromatic transparency color perceptions, especially for the devices with thin Ag electrodes ($t_{Ag} = 30$ nm). The transmitted light from the STOPVs further demonstrates extraordinary transparency color rendering capacities with the highest CRIs (> 96) ever reported for semi-transparent OPV devices. These combined advantages prove that inverted STOPVs based on the PBDTTT-C-T:PC$_{71}$BM blend can provide high quality transmitted light that is suitable for window applications. We have also established that the TMM optical model combined with the test sample method can accurately portrays the optical behaviors of STOPV systems.

2.6 Experimental results using a recently adquired glove-box system with integrated thermal evaporator at the CIO laboratories, México

As the only member in the group with experience using glove box systems and thermal evaporators due to my research stay at the University of Washington, I was in charge of setting up a recently acquired glove box with integrated thermal evaporator in order to enable it for the manufacture of OPVs. Since every thermal evaporator behaves slightly different depending on the geometry, the type of sources, the evaporation boats, etc., this section refers to unpublished data derived from experiments performed at the CIO laboratories as long as observations regarding the requirements for getting well performed devices using this particular evaporator.

Figure 52 shows some of the JV curves I got in some of our former experiments with this evaporator. Several conditions were attempted such as using several thicknesses of the active layer, changing the thickness of the film between the active layer and the metallic top-contact, letting the system to make vacuum overnight in order to reach a lower pressure and using both architectures (inverted and conventional) in order to discard degradation as a factor involved in a poor performance. All cases were characterized by high series resistance and low parallel resistance, both cases undesirable for the performance of the devices. This behavior is commonly observed in cells where there is abundance of defects and the films, despite not shorted, are partially penetrated by the surrounding layers. Experiments evaporating the metallic top-contact at different speeds resulted in totally shorted devices when a relatively high deposition speed (1-2 Å/s) is used to deposit the film immediately over the BHJ (such as MoO_3, Ca or Al). The JV curves showed in Figure 52 corresponds to devices prepared by using only 0.1 Å/s. This result suggested that the evaporation process can potentially perforate the active layer, producing as consequence, devices with low performance.

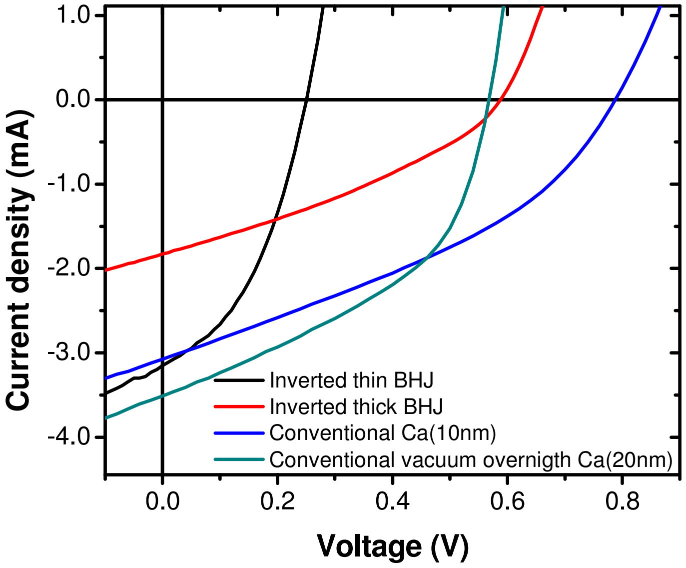

Figure 52 Former experiments. The inverted solar cells were prepared following the structure ITO/ZnO nanoparticles/P3HT:PCBM/MoO_3/Ag. Conventional solar cells were prepared following ITO/PEDOT:PSS/P3HT:PCBM/Ca/Al.

As a proof of concept, inverted devices using the configuration ITO/ZnO nanoparticles/P3HT:PCBM/PEDOT:PSS/Ag were prepared. In this case the PEDOT:PSS film is applied by spin coating, therefore there is no risk of perforating the BHJ during the deposition of the HTL. The Ag film was applied at a speed of 0.04 Å/s during the first 10 nm and after that a speed of 2 Å/s is used to get a final Ag thickness of 120 nm. As it can be observed in Figure 53, the fill factor and the current density dramatically increased with respect to the cases in Figure 52 supporting the idea that the low efficiency was consequence of partially shorted devices. It should be mentioned that the P3HT:PCBM surface is very hydrophobic, making nearly impossible to deposit, by spin coating, water based solutions like PEDOT:PSS. In order to prepare the devices, a diluted solution of PEDOT:PSS/Butanol/Isopropil alcohol (1/2/2) was used. This solution was deposited on top of the P3HT:PCBM forming a very thin film with good results. On top of that, a film of pure PEDOT:PSS was spin coated to get the desired thickness. Despite our efforts, the thickness of PEDOT:PSS was still not uniform and the thickness of the films were not reproducible, so an accurate control of the device performance using PEDOT:PSS on top of the BHJ was impossible. Regardless of the limitation, this experiment confirmed that the deposition of the charge transport layer on top of the BHJ is critical in order to increase the FF, therefore, this film should be deposited under very controlled conditions in order to avoid any damage to the BHJ film.

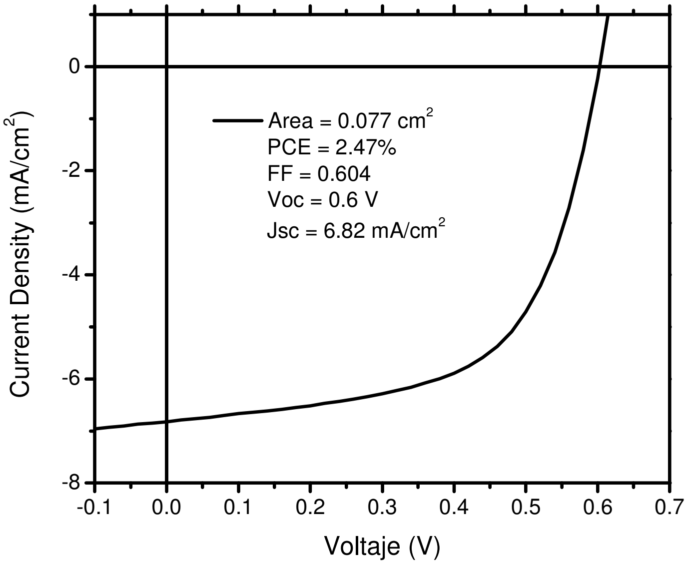

Figure 53 Inverted cell prepared by applying PEDOT:PSS as HTL and Ag at a low speed rate (0.04 Å/s) to avoid damages to the organic film.

A new type of evaporation boat was employed in order to avoid damages to the organic film during the evaporation process. These evaporation boats were closed, ensuring the source material is always hidden from the cells substrates. This way we guarantee that the only material deposited on the cells is the vapor coming from the material and not chunks expelled due to the high temperature. The cells prepared for this experiment, both conventional and inverted using P3HT:$PC_{71}BM$, were optimized using the optical simulator, getting ideal thicknesses of 198 nm for the inverted case and 215 nm for conventional one. Since no big variation in the calculated current density was observed according to the simulator, a thickness of 210 nm was used for both architectures. Deposition rates of 0.1 Å/s were used for both MoO_3 and Ca. In this experiment the V_{oc} and J_{sc} behaved as expected for this organic blend (Figure 54) according to the reported in literature [58], the FF was slightly low (0.45) indicating that penetration of MoO_3 and Ca in the BHJ could still be present to certain degree, nevertheless the overall good performance (PCE = 3.02%), the reproducibility of the results (all manufactures devices worked and observed a similar behavior) and the high V_{oc} and J_{sc} values suggested that the penetration problem was mostly solved by using the closed boats. On the other hand, the high reproducibility and efficiency of the devices for a blend whose standard reported efficiency is around 4% [58], established that the evaporator is currently in good condition for the manufacture of reasonable well performed OPV devices in a laboratory scale.

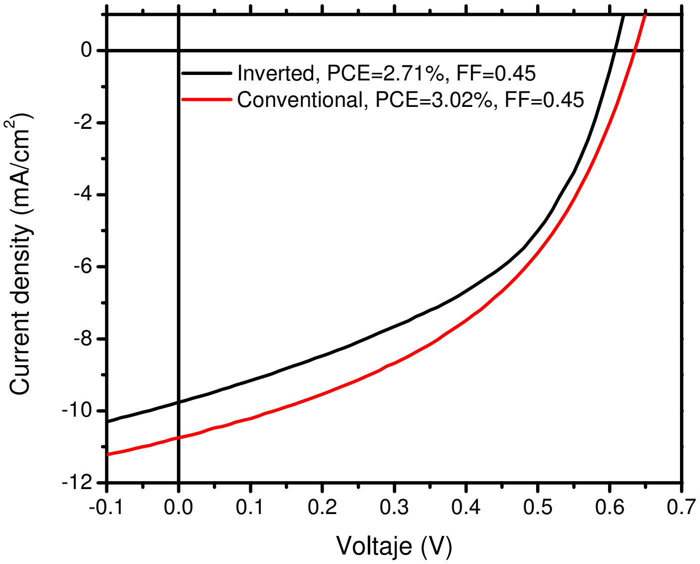

Figure 54 JV curves of conventional and inverted cells prepared by using closed evaporation boats.

3. Conclusions and future work

Despite particular conclusions are presented by the end of each project discussed, herein some of the most important conclusions of this thesis are summarized.

1. Wood's metal alloy used as cathode permits an economical, easy and fast way to manufacture OPV cells under environmental conditions without the need of high vacuum chambers or any specialized equipment like the one used to apply aluminum, for this reason it can be used for express testing of new promising organic materials. In this work the performance of boronate derivatives M1 and M2, and the polymer MEH–PPV in OPVs devices was tested using this approach. EQE measurements demonstrated that the proposed boronates behaves as electron donor when used in blend with MEH-PPV and $PC_{61}BM$. $V_{oc} \approx 600$ mV and J_{sc} as high as 3.1 mA/cm^2 under solar (AM1.5) illumination were measured for MEH–PPV:M1:$PC_{61}BM$ based samples. Measurements of FF from the J–V curves, under Xe lamp illumination, allowed estimating the electrical efficiencies under solar illumination up to 0.8%.
2. The photovoltaic performance of OPVs cells based on the polymer blend P3HT:$PC_{61}BM$ (1:2 wt. ratio) tested for both conventional and inverted architectures by using Wood´s metal and silver paint as cathode and anode respectively using a totally free vacuum steps process was found to be very acceptable in comparison with previous reports of devices based on the same polymer blend. The electrical performance of OPV cells fabricated with

Wood's metal was V_{oc} = 528 mV, J_{sc} = 7.35 mA/cm^2 and FF = 0.45 with an efficiency PCE = 1.8 % while with silver paint V_{oc} = 530 mV, J_{sc} = 9.64 mA/cm^2, FF = 0.42 and PCE = 2.19% was achieved. We associate the higher efficiency got for the inverted cell to the better stability associated with this architecture. Our results also indicated that, while thermal evaporation can cause severe damage to the organic films, Wood's metal and silver paint are friendly with the organic films.

3. Enhanced light trapping and conductivity were achieved by combining high refractive index TeO_2 with a thin Ag film as hybrid transparent UTMF electrode on PIDT-PhanQ:$PC_{71}BM$ based devices. As a result, OPVs with performance higher than those with ITO electrode on both glass ($PCE_{TeO2/Ag}$ = 6.6 %, PCE_{ITO} = 6.5 %) and plastic ($PCE_{TeO2/Ag}$ = 5.8%, PCE_{ITO} = 5.6%) substrates were achieved. The flexible devices on PEN/TeO_2/Ag also showed excellent bending stability compared to devices made from ITO electrode. The EQE of these cells could be easily tuned by simply changing the thickness of the TeO_2 film, offering the possibility of further optimizing light absorption without affecting the electrical attributes of nanometric OPV devices.
4. A novel polymer-based STOPV was demonstrated by incorporating an ultra-thin BHJ layer (~ 50 nm) based on a blend of PIDT-PhanQ:$PC_{71}BM$ along with highly transparent hybrid cathode based on a solution-processed interfacial layer and ultra-thin Ag films. These polymer-based STOPVs exhibited good PCE and AVT (5.1% and 24.35% respectively for a 30 nm Ag film) with neutral color perception close to that of white light. This result shows great promise for polymer-based STOPVs for solar windows in future green buildings.
5. We have demonstrated high efficiency semi-transparent OPV cells with significantly improved performance compared to other STOPVs of similar transparency. The STOPV devices under AM1.5 illumination provide close to white or achromatic transparency color perceptions, especially for the devices with thin Ag electrodes (t_{Ag} = 30 nm). The transmitted light from

the STOPVs further demonstrates extraordinary transparency color rendering capacities with the highest CRIs (> 96) ever reported for semi-transparent OPV devices. These combined advantages prove that inverted STOPVs based on the PBDTTT-C-T:$PC_{71}BM$ blend can provide high quality transmitted light that is suitable for window applications. We have also established that the TMM optical model combined with the test sample method can accurately portrays the optical behaviors of STOPV systems.

Future work: An interesting aspect of the cell simulator developed during this thesis is the fact that it can be continuously extended to represent new aspects of the solar cell behavior, as an example, incorporating models for the drift and diffusion of carriers with bimolecular recombination and field dependent generation mechanisms [133], the description can be extended to portray not only the current density but the complete electrical behavior of the cells, allowing to directly calculate power conversion efficiencies from the model.

Regarding STOPVs, since in this thesis the analysis method using CRI indexes was successfully tested, the calculation process can be reversed in order to theoretically predict conditions for the development of devices with good color rendering and average transparency. As an example, the simulator is currently capable to simultaneously vary the thickness of several layers in order to better control the color rendering of the cell. For vividly colorful polymers like P3HT, the neutral semitransparent devices develop by this technique would experience a loss in current since thinner active layers must be used to ensure a reasonably average transparency. A tradeoff between transparency and efficiency would be required for this type of devices. Preliminary results on this field show that the color rendering of devices based on the TeO_2/Ag substrate can be tailored more efficiently that devices based on ITO substrate. In this way the ultrathin silver electrode developed in this thesis as substitute for ITO can be exploited for the development of new sorts of semitransparent devices employing common organic blends.

Tandem solar cells are devices where the absorptions of two complementary materials are employed to extend the photoactive range of the cell. In order to maximize the efficiency, the tandem cell can be seen as two coupled optical cavities that should appropriately be in resonance in order to maximize the internal electric field. Since both cells are connected in series, the current density produced by both devices must be equal in order to avoid one device to hinder the performance of the other. Since optical simulation is capable to estimate the photon absorption and because an EQE measurement coupled to the optical simulation can be used to determine the real current density of a particular polymer blend, our software can be used as a tool for the design of tandem devices with optimized coupled cavities and equal current densities. This way the development of tandem devices of superior performance is easily achievable using the software as a guideline for the design of devices.

4. Appendix

This appendix is intended to describe with a little more detail the method employed to calculate the electric field within the solar devices. The whole theory required to perform the calculations was already described in chapter 1. Herein, the discussion topics will be more closely related to the algorithms than the theory itself. All calculations were performed using Matlab.

The system is defined by the stack of materials, a list of thicknesses, the spectrum of the illuminant employed to test the cell, a range of wavelengths and a parameter indicating which film is the BHJ, in this way:

```
layers={'Air' 'substrate' 'material1' 'material2' ... 'materialn' 'Air'};
thick=[10 1000000 120 33 ... 40 10]; %in nm
illuminant=xlsread('PowerSimulator.xls');
lambda=300:1:900;
activefilm=4; %in this case 'material2'
```

Since the calculations consider only light traveling perpendicular to the interfaces, an incidence angle is not required. A library with the complex refractive index ($n = \eta(\lambda) + i\kappa(\lambda)$) of all materials in steps of 1 nm is used. Each material name (`'substrate'`, `'materialn'`, etc.) identifies only one material in the library and stores the refractive index in the optical range. Two air films (refractive index $n = 1$ for the whole optical range) are added to account for reflections at the first and last interface; the thickness of such films does not affect the calculations as long as it is not zero. The light is assumed to come from the left side. Also it is always assumed the second material will be some sort of substrate, so the interference within it is incoherent. Matrices I and L are calculated by means of functions:

```
function I = Imatrix(n1,n2)
r=(n1-n2)/(n1+n2);
t=2*n1/(n1+n2);
I=[1 r; r 1]/t; %eq (3)

function L = Lmatrix(n,d,l)
xi=2*pi*n*d*i/l;
L=[exp(-xi) 0; 0 exp(xi)]; %eq (4)
```

Where `n1` and `n2` in function `Imatrix` are the complex refractive index before and after the interface respectively. On the other hand `n`, `d` and `l` in function `Lmatrix` are the refractive index of the film, its thickness and the wavelength of the light in nm. The total reflection and transmission of the system (where `n(m,l)` stands for refractive index of film `m` at wavelength `l`) are calculated in this way:

```
for l=1:length(lambda)
   %Substrate
   S1=Imatrix(n(1,l),n(2,l)); %n(1,l) refractive index of air
   xi=2*pi*n(2,l)/lambda(l);  %n(2,l) refractive index of glass
   %Incoherent absorption of glass
   Inc=[abs(exp(-1i*xi*thick(2)))^2 0; 0 abs(exp(1i*xi*thick(2)))^2];

      %Solar cell interfaces
   S2=I_mat(n(2,l),n(3,l));
   for film=3:(length(thick)-1)
      S2=S2*Lmatrix(n(film,l),thick(film),lambda(l))*Imatrix(n(film,l),n(
film+1,l));
   end %eq (8)

   %Fresnel coefficients, air-glass
   r0m=S1(2,1)/S1(1,1);
   t0m=1/S1(1,1);
   rm0=-S1(1,2)/S1(1,1);
   tm0=(S1(1,1)*S1(2,2)-S1(1,2)*S1(2,1))/S1(1,1);
   %Air-glass intensity matrix
   T1=[1 -abs(rm0)^2; abs(r0m)^2 abs(t0m*tm0)^2-
abs(r0m*rm0)^2]/abs(t0m)^2; %eq (25)

   %Fresnel coefficients, solar cell
   rmN=S2(2,1)/S2(1,1);
   tmN=1/S2(1,1);
   rNm=-S2(1,2)/S2(1,1);
   tNm=(S2(1,1)*S2(2,2)-S2(1,2)*S2(2,1))/S2(1,1);
   %Intensity transfer matrix of solar cell films
   T2=[1 -abs(rNm)^2; abs(rmN)^2 abs(tmN*tNm)^2-
abs(rmN*rNm)^2]/abs(tmN)^2; %eq (25)
```

```
   %Total intensity matrix
   T=T1*Inc*T2;
   %Total reflectance and transmitance for wavelength “l”
   Ref(l)=T(2,1)/T(1,1); %eq (27)
   Tran(l)=1/T(1,1); %eq (28)
end
```

Now, in order to calculate the spectrograms of $|E|^2$ normalized, first we calculate the effect of only the reflection and absorption of the substrate, which is done using intensity matrices (incoherent case). This can be done using the matrices `T1` and `Inc` already calculated as is shown next for a wavelength `l`:

```
Tglass=T1*Inc;
TranGlass(l)=(1/Tglass(1,1))*(real(n(2,l))/real(n(1,l))); %transmitance
just before the right interface of the substrate
```

Then, the field in the solar cell is calculated using amplitude matrices (coherent case). The field is calculated in positions called `posX`.

```
interfX=cumsum(thick); %positions of the interfaces
posX=(stepsize/2):stepsize:sum(thick); %positions to evaluate field
layerX=
sum(repmat(posX,length(t),1)>repmat(interfX',1,length(posX)),1)+1;
%layer in which point posX is in
for material = 3:length(thick)
      xi=2*pi*n(material,l)/range(l);
      dj=thick(material);
      pointF=find(layerX == material); %indexes of points in the current
film
      x=posX(pointF)-interfX(material-1); %distances to previous
interface
      Sprime=Imatrix(n(2,l),n(3,l));
      for film=3:material-1
            Sprime=Sprime*Lmatrix(n(film,l),thick(film),lambda(l))*Imatri
      x(n(film,l),n(film+1,l)); %eq (15)
      end
      for film=material+1:length(t)
            Sdoubleprime=Sdoubleprime*Imatrix(n(film-
1,l),n(film,l))*Lmatrix(n(film,l),thick(film),lambda(l)); %eq (16)
      end
      % Normalized |E|2  profile
E(pointF,l)=(Sdoubleprime(1,1)*exp(-1i*xi*(dj-
x))+Sdoubleprime(2,1)*exp(1i*xi*(dj-
x)))./(Sprime(1,1)*Sdoubleprime(1,1)*exp(-
1i*xi*dj)+Sprime(1,2)*Sdoubleprime(2,1)*exp(1i*xi*dj)); %eq (24)
end
```

This process should be repeated for all wavelengths (done by another `for l=1:length(lambda)` cycle) to get the E amplitude in the whole optical range and in all positions of the cell. Squaring the amplitude, spectrograms like Figure 26 are obtained. Finally the energy dissipated at the BHJ considering the spectrum of the illuminant and the absorption and reflection by the substrate is calculated as follows:

```
% Absorption coefficient of each film
a=zeros(length(t),length(lambda));
for film=3:length(thick)
     a(film,:)=4*pi*imag(n(film,:))./(lambda*1e-7);
end

%energy dissipated in BHJ combining eq (31) and (32).
pointsBHJ=find(layerX == activefilm);
Q=repmat(a(activefilm,:).*(real(n(activefilm,:))./real(n(2,:))).*illumina
nt.*TranGlass,length(pointsBHJ),1).*(abs(E(pointsBHJ,:)).^2);
```

while the number of photogenerated charges (like shown in Figure 50) is expressed as:

```
exiton=(Q*1e-3).*repmat(lambda*1e-9,length(pointsBHJ),1)/(h*c);
```

where `h` is the Planck constant and `c` is the speed of light.

5. | References

[1] *Atmospheric Carbon Dioxide and Carbon Isotope Records*. 2013; Available from: http://cdiac.ornl.gov/trends/co2/contents.htm.

[2] *GISS Surface Temperature Analysis*. 2013; Available from: http://data.giss.nasa.gov/gistemp/graphs_v3/.

[3] *Global climate change*. 2013; Available from: http://climate.nasa.gov/.

[4] S.K. Hau, H.-L. Yip, N.S. Baek, J. Zou, and K. O'Malley, *Air-stable inverted flexible polymer solar cells using zinc oxide nanoparticles as an electron selective layer.* Appl. Phys. Lett., 2008. **92**: p. 253301.

[5] J.Y. Kim, S.H. Kim, H.-H. Lee, K. Lee, W. Ma, X. Gong, and A.J. Heeger, *New architecture for high-efficiency polymer photovoltaic cells using solution-based titanium oxide as an optical spacer.* Adv. Mater., 2006. **18**: p. 572–576.

[6] J.Y. Kim, K. Lee, N.E. Coates, D. Moses, T.-Q. Nguyen, M. Dante, and A.J. Heeger, *Efficient tandem polymer solar cells fabricated by all-solution processing.* Science, 2007. **317**: p. 222-225.

[7] *Transparent cost database*. 2013; Available from: http://en.openei.org/apps/TCDB/.

[8] *Best research efficiencies chart*. 2013; Available from: http://www.nrel.gov/ncpv/images/efficiency_chart.jpg.

[9] R.R. Lunt, N.C. Giebink, A.A. Belak, J.B. Benziger, and S.R. Forrest, *Exciton diffusion lengths of organic semiconductor thin films measured by spectrally resolved photoluminescence quenching.* Journal of applied physics, 2009. **105**: p. 053711.

[10] A. Haugeneder, M. Neges, C. Kallinger, W. Spirkl, U. Lemmer, J. Feldmann, U. Scherf, E. Harth, A. Gügel, and K. Müllen, *Exciton diffusion and dissociation in conjugated polymer/fullerene blends and heterostructures.* Physical review B, 1999. **59**: p. 15346-15351.

[11] G. Yu and A.J. Heeger, *Charge separation and photovoltaic conversion in polymer composites with internal donor/acceptor heterojunctions.* J. Appl. Phys., 1995. **78**: p. 4510-4515.

[12] G. Yu, J. Gao, J.C. Hummelen, F. Wudl, and A.J. Heeger, *Polymer photovoltaic pells: enhanced efficiencies via a network of internal donor-acceptor heterojunctions.* Science, 1995. **270**: p. 1789-1791.

[13] E. Fortunato, D. Ginley, H. Hosono, and D.C. Paine, *Transparent Conducting Oxides for Photovoltaics.* MRS Bull., 2007. **32**: p. 242-247.

[14] Y. Zhang, J. Zou, H.-L. Yip, K.-S. Chen, D.F. Zeigler, Y. Sun, and A.K.-Y. Jen, *Indacenodithiophene and Quinoxaline-Based Conjugated Polymers for Highly Efficient Polymer Solar Cells.* Chem. Mater., 2011. **23**: p. 2289–2291.

[15] L. Huo, S. Zhang, X. Guo, F. Xu, Y. Li, and J. Hou, *Replacing Alkoxy Groups with Alkylthienyl Groups: A Feasible Approach To Improve the Properties of Photovoltaic Polymers.* Angewandte Chemie International Edition, 2011. **50**: p. 9697–9702.

[16] H.-Y. Chen, J. Hou, S. Zhang, Y. Liang, G. Yang, Y. Yang, L. Yu, Y. Wu, and G. Li, *Polymer solar cells with enhanced open-circuit voltage and efficiency.* Nature Photonics, 2009. **3**: p. 649 - 653.

[17] Y. Liang and L. Yu, *A New Class of Semiconducting Polymers for Bulk Heterojunction Solar Cells with Exceptionally High Performance.* Acc. Chem. Res., 2010. **43**: p. 1227–1236.

[18] Y. Liang, Z. Xu, J. Xia, S.-T. Tsai, Y. Wu, G. Li, C. Ray, and L. Yu, *For the Bright Future—Bulk Heterojunction Polymer Solar Cells with Power Conversion Efficiency of 7.4%.* Advanced Materials, 2010. **22**: p. E135–E138.

[19] S.K. Hau, H.-L. Yip, H. Ma, and A.K.-Y. Jen, *High performance ambient processed inverted polymer solar cells through interfacial modification with a fullerene self-assembled monolayer.* Appl. Phys. Lett., 2008. **93**: p. 233304.

[20] J.A. Duffie and W.A. Beckman, *Solar Engineering of thermal processes,* 1980, USA: John Wiley & Sons.

[21] A. Moliton and J.-M. Nunzi, *How to model the behaviour of organic photovoltaic cells.* Polymer International, 2006. **55**: p. 583-600.

[22] B.C. Thompson and J.M.J. Fréchet, *Polymer–Fullerene Composite Solar Cells.* Angewandte Chemie International Edition, 2007. **47**: p. 58–77.

[23] R. Kroon, M. Lenes, J.C. Hummelen, P.W.M. Blom, and B.d. Boer, *Small Bandgap Polymers for Organic Solar Cells.* Polymer Reviews, 2008. **48**: p. 531-582.

[24] L.A.A. Pettersson, L.S. Roman and O. Inganäs, *Modeling photocurrent action spectra of photovoltaic devices based on organic thin films.* J. Appl. Phys., 1999. **86**: p. 487-496.

[25] P. Peumans, A. Yakimov and S.R. Forrest, *Small molecular weight organic thin-film photodetectors and solar cells.* J. Appl. Phys., 2003. **93**: p. 3693-3723.

[26] C.C. Katsidis and D.I. Siapkas, *General transfer-matrix method for optical multilayer systems with coherent, partially coherent, and incoherent interference.* Applied Optics, 2002. **41**: p. 3978-3987.

[27] G.F. Burkhard, E.T. Hoke and M.D. McGehee, *Accounting for Interference, Scattering, and Electrode Absorption to Make Accurate Internal Quantum Efficiency Measurements in Organic and Other Thin Solar Cells.* Adv. Mater., 2010. **22**: p. 3293–3297.

[28] W.D. Wright, *A re-determination of the trichromatic coefficients of the spectral colours.* Trans. Opt. Soc., 1929. **30**: p. 141.

[29] J. Guild, *The Colorimetric Properties of the Spectrum.* Phil. Trans. R. Soc. Lond. A, 1932. **230**: p. 149-187.

[30] J.M. Geusebroek, R. Boomgaard, A.W.M. Smeulders, and T. Gevers, *Color constancy from physical principles.* Pattern Recogn. Lett., 2003. **24**: p. 1653-1662.

[31] J. Schanda, *Colorimetry Understanding the CIE System,* 2007, USA: John Wiley & Sons. 71-73.

[32] A. Colsmann, A. Puetz, A. Bauer, J. Hanisch, E. Ahlswede, and U. Lemmer, *Efficient Semi-Transparent Organic Solar Cells with Good Transparency Color Perception and Rendering Properties.* Advanced Energy Materials, 2011. **1**: p. 599–603.

[33] D.B. Judd, D.L. Macadam, G. Wyszecki, H.W. Budde, H.R. Condit, S.T. Henderson, and J.L. Simonds, *Spectral Distribution of Typical Daylight as a Function of Correlated Color Temperature.* J. Opt. Soc. Am., 1964. **54**: p. 1031-1040.

[34] D.-Y. Tzeng and R.S. Berns, *A Review of Principal Component Analysis and Its Applications to Color Technology.* Color Research & Application, 2005. **30**: p. 84-98.

[35] J.L. Simonds, *Application of Characteristic Vector Analysis to Photographic and Optical Response Data.* J. Opt. Soc. Am., 1963. **53**: p. 968-971.

[36] J.F. Salinas, J.-L. Maldonado, G. Ramos-Ortíz, M. Rodríguez, M.-A. Meneses-Nava, O. Barbosa-García, R. Santillan, and N. Farfán, *On the use of Woods metal for fabricating and testing polymeric organic solar cells: An easy and fast method.* Solar Energy Materials & Solar Cells, 2011. **95**: p. 595–601.

[37] F.C. Krebs, *Air stable polymer photovoltaics based on a process free from vacuum steps and fullerenes.* Solar Energy Materials & Solar Cells 2008. **92**: p. 715–726.

[38] A.D. Pasquier, S. Miller and M. Chhowalla, *On the use of Ga–In eutectic and halogen light source for testing P3HT–PCBM organic solar cells.* Solar Energy Materials & Solar Cells, 2006. **90**: p. 1828–1839.

[39] J.L. Maldonado, G. Ramos-Ortíz, M.L. Miranda, S. Vázquez-Córdova, M.A. Meneses-Nava, O. Barbosa-García, and M. Ortíz-Gutiérrez, *Two examples of organic opto-electronic devices: light emitting diodes and solar cells.* Am. J. Phys., 2008. **76**: p. 1130–1136.

[40] M. Rodríguez, J.L. Maldonado, G. Ramos-Ortíz, J.F. Lamère, P.G. Lacroix, N. Farfán, M.E. Ochoa, R. Santillan, M.A. Meneses-Nava, O. Barbosa-García, and K. Nakatani, *Synthesis and nonlinear optical characterization of novel boronate derivatives of cinnamaldehyde.* New J. Chem., 2009. **33**: p. 1693–1702.

[41] M. Rodríguez, R. Castro-Beltrán, G. Ramos-Ortíz, J.L. Maldonado, N. Farfán, O. Domínguez, J. Rodríguez, R. Santillan, M.A. Meneses-Nava, O. Barbosa-García, and J. Peon, *Synthesis and third-order non linear optical studies of a novel four-coordinated organoboron derivative and a bidentate ligand.* Synth. Met., 2009. **159**: p. 1281–1287.

[42] F. Qiao, A. Liu, Y. Zhou, Y. Xiao, and P.O. Yang, *Bulk heterojunction organic solar cell based on a novel fluorescent fluorine-boron complex.* J. Mater. Sci., 2009. **44**: p. 1283-1286.

[43] F. Padinger, R.S. Rittberger and N.S. Sariciftci, *Effect of postproduction treatment on plastic solar cells.* Adv.Funct.Mater., 2003. **13**: p. 1–4.

[44] H.H.N.S. Sariciftci, *Polymer solar cells.* Adv. Polym. Sci., 2008. **214**: p. 1-86.

[45] H. Hoppe, M. Niggemann, C. Winder, J. Kraut, R. Hiesgen, A. Hinsch, D. Meissner, and N.S. Sariciftci, *Nanoscale morphology of conjugated polymer/fullerene based bulk heterojunction solar cells.* Adv. Funct. Mater., 2004. **14**: p. 1005-1011.

[46] P.M. Borsenberger and D.S. Weiss, *Organic Photoreceptors for Xerography,* 1998, New York: Marcel Dekker Inc.

[47] D.W. Sievers, V. Shrotriya and Y. Yang, *Modeling optical effects and thickness dependent current in polymer bulk-heterojunction solar cells.* J. Appl. Phys., 2006. **100**: p. 114509.

[48] R.P.B. Jr., R.D. Gomez, W.N. Herman, and D.B. Romero, *Organic photovoltaic devices based on a block copolymer/fullerene blend.* Org.Electron., 2006. **7**: p. 508–513.

[49] F. Qiao, A. Liu, Y. Xiao, Y.P. Ou, J.Q. Zhang, and Y.C. Sang, *Enhanced photovoltaic characteristics of solar cells based on n-type triphenodioxazine derivative.* Microelectron. J., 2008. **39**: p. 1568–1571.

[50] J.-K.Lee, K.Fujida, T.Tsutsui, and M.-R.Kim, *Synthesis and photovoltaic properties of soluble fulleropyrrolidine derivatives for organic solar cells.* Sol. EnergyMater.Sol.Cells, 2007. **91**: p. 892–896.

[51] *Heliatek consolidates its technology leadership by establishing a new world record for organic solar technology with a cell efficiency of 12%.* 2013; Available from: http://www.heliatek.com/newscenter/latest_news/neuer-weltrekord-fur-organische-solarzellen-heliatek-behauptet-sich-mit-12-zelleffizienz-als-technologiefuhrer/?lang=en.

[52] B. Domercq, C. Grasso, J.L. Maldonado, M. Halik, S. Barlow, S.R. Marder, and B. Kippelen, *Electron-transport properties and use in organic light-emitting diodes of a bis(dioxaborine)fluorene derivative.* J. Phys. Chem. B, 2004. **108**: p. 8647–8651.

[53] C. Chang, C.-I. Chao and R.-H. Lee, *Enhancing the efficiency of MEH-PPV and PCBM based polymer solar cells via optimization of device configuration and processing conditions.* Journal of Applied Polymer Science, 2006. **101**: p. 1919–1924.

[54] C. Salto, J.-F. Salinas, J.-L. Maldonado, G. Ramos-Ortíz, M. Rodríguez, M.-A. Meneses-Nava, O. Barbosa-García, J.-A.D. Oso, and M. Ortíz-Gutiérrez, *Performance of OPVs cells with the eutectic alloy Wood's metal used as cathode and P3HT:PC61BM blend as active layer.* Synthetic Metals, 2011. **161**: p. 2412–2416.

[55] C.K. F, *All solution roll-to-roll processed polymer solar cells free from indium-tin-oxide and vacuum coating steps.* Org. Electron., 2009. **10**: p. 761–768.

[56] F.C. Krebs, T. Tromholt and M. Jørgensen, *Upscaling of polymer solar cell fabrication using full roll-to-roll processing.* Nanoscale, 2010. **2**: p. 873–886.

[57] F.C. Krebs, T.D. Nielsen, J. Fyenbo, M. Wadstrøm, and M.S. Pedersen, *Manufacture, integration and demonstration of polymer solar cells in a lamp for the Lighting Africa initiative.* Energy Environ. Sci., 2010. **3**: p. 512–525.

[58] Y. He, B. Peng, G. Zhao, Y. Zou, and Y. Li, *Indene addition of [6,6]-phenyl-C61-butyric acid methyl ester for high-performance acceptor in polymer solar cells.* J. Phys. Chem. C, 2011. **115**: p. 4340–4344.

[59] E. Nasybulin, S. Wei, M. Cox, I. Kymissis, and K. Levon, *Morphological and spectroscopic studies of electrochemically deposited poly(3,4-ethylenedioxythiophene) (PEDOT) hole extraction layer for organic photovoltaic device (OPVd) fabrication.* J. Phys. Chem. C, 2011. **115**: p. 4307–4314.
[60] Z. Liu, D. He, Y. Wang, H. Wu, and J. Wang, *Graphene doping of P3HT:PCBM photovoltaic devices.* Synthetic Metals, 2010. **160**: p. 1036–1039.
[61] D. Chirvase, J. Parisi, J.C. Hummelen, and V. Dyakonov, *Influence of nanomorphology on the photovoltaic action of polymer–fullerene composites.* Nanotechnology, 2004. **15**: p. 1317–1323.
[62] K. Inoue, R. Ulbricht, P.C. Madakasira, M. Zhou, S.B. Lee, J. Ferraris, and A.A. Zakhidov, *High efficiency P3HT/PCBM solar cell.* Mater. Res. Soc. Symp. Proc., 2005. **836**: p. 69–74.
[63] W.J.E. Beek, M.M. Wienk, M. Kemerink, X. Yang, and R.A.J. Janssen, *Hybrid Zinc Oxide Conjugated Polymer Bulk Heterojunction Solar Cells.* J. Phys. Chem. B, 2005. **109**: p. 9505–9516.
[64] A. Verma and J.W. Evans, *Measurements of the electrical conductivity of Wood's alloy and other low melting point alloys.* Metall. Mater. Trans. B, 1994. **25B**: p. 937.
[65] D.R. Lide, *CRC Handbook of Chemistry and Physics,* 2008, Boca Raton, FL: CRC Press.
[66] J.-F. Salinas, H.-L. Yip, C.-C. Chueh, C.-Z. Li, J.-L. Maldonado, and A.K.-Y. Jen, *Optical Design of Transparent Thin Metal Electrodes to Enhance In-Coupling and Trapping of Light in Flexible Polymer Solar Cells.* Adv. Mater., 2012. **24**: p. 6362–6367.
[67] N.S. Sariciftci, L. Smilowitz, A.J. Heeger, and F. Wudl, *Photoinduced Electron Transfer from a Conducting Polymer to Buckminsterfullerene.* Science, 1992. **258**: p. 1474-1476.
[68] S.E. Shaheen, C.J. Brabec, N.S. Sariciftci, F. Padinger, T. Fromherz, and J.C. Hummelen, *2.5% efficient organic plastic solar cells.* Appl. Phys. Lett., 2001. **78**: p. 841-843.
[69] J. Weickert, R.B. Dunbar, H.C. Hesse, W. Wiedemann, and L. Schmidt-Mende, *Nanostructured Organic and Hybrid Solar Cells.* Adv. Mater., 2011. **23**: p. 1810-1828.
[70] D.-H. Ko, J.R. Tumbleston, A. Gadisa, M. Aryal, Y. Liu, R. Lopez, and E.T. Samulski, *Light-trapping nano-structures in organic photovoltaic cells.* J. Mater. Chem., 2011. **21**: p. 16293-16303.
[71] A.C. Tolcin, *2009 Minerals Yearbook INDIUM,* . USGS2011, USA.
[72] O. Inganäs, Nat. Photonics, 2011. **5**: p. 201-202.
[73] Y. Leterrier, L. Medico, F. Demarco, J.A.E. Manson, U. Betz, M.F. Escola, M.K. Olsson, and F. Atamny, *Mechanical integrity of transparent conductive oxide films for flexible polymer-based displays.* Thin Solid Films, 2004. **460**: p. 156-166.
[74] S.K. Hau, H.-L. Yip, J. Zou, and A.K.-Y. Jen, *Indium tin oxide-free semi-transparent inverted polymer solar cells using conducting polymer as both bottom and top electrodes.* Org. Electron., 2009. **10**: p. 1401–1407.

[75] S.-I. Na, S.-S. Kim, J. Jo, and D.-Y. Kim, *Efficient and Flexible ITO-Free Organic Solar Cells Using Highly Conductive Polymer Anodes.* Adv. Mater., 2008. **20**: p. 4061–4067.

[76] J. Xue, S. Uchida, B.P. Rand, and S.R. Forrest, *4.2% efficient organic photovoltaic cells with low series resistances.* Appl. Phys. Lett., 2004. **84**: p. 3013-3015.

[77] S. Choi, W.J. Potscavage and B. Kippelen, *Area-scaling of organic solar cells.* J. Appl. Phys., 2009. **106**: p. 054507.

[78] J. Liu, A.W. Hains, J.D. Servaites, M.A. Ratner, and T.J. Marks, *Highly Conductive Bilayer Transparent Conducting Oxide Thin Films for Large-Area Organic Photovoltaic Cells.* Chem. Mater., 2009. **21**: p. 5258–5263.

[79] Y. Xia, K. Sun and J. Ouyang, *Solution-Processed Metallic Conducting Polymer Films as Transparent Electrode of Optoelectronic Devices.* Advanced Materials, 2012. **24**: p. 2436–2440.

[80] Z. Tang, L.M. Andersson, Z. George, K. Vandewal, K. Tvingstedt, P. Heriksson, R. Kroon, M.R. Andersson, and O. Inganäs, *Interlayer for Modified Cathode in Highly Efficient Inverted ITO-Free Organic Solar Cells.* Advanced Materials, 2012. **24**: p. 554–558.

[81] R.C. Tenent, T.M. Barnes, J.D. Bergeson, A.J. Ferguson, B. To, L.M. Gedvilas, M.J. Heben, and J.L. Blackburn, *Ultrasmooth, Large-Area, High-Uniformity, Conductive Transparent Single-Walled-Carbon-Nanotube Films for Photovoltaics Produced by Ultrasonic Spraying.* Adv. Mater., 2009. **21**: p. 3210–3216.

[82] J. Wu, H.A. Becerril, Z. Bao, Z. Liu, Y. Chen, and P. Peumans, *Organic solar cells with solution-processed graphene transparent electrodes.* Appl. Phys. Lett., 2008. **92**: p. 263302.

[83] J.-Y. Lee, S.T. Connor, Y. Cui, and P. Peumans, *Solution-Processed Metal Nanowire Mesh Transparent Electrodes.* Nanoletters, 2008. **8**: p. 689-692.

[84] J. Zou, H.-L. Yip, S.K. Hau, and A.K.-Y. Jen, *Metal grid/conducting polymer hybrid transparent electrode for inverted polymer solar cells.* Appl. Phys. Lett., 2010. **96**: p. 203301.

[85] M.-G. Kang and L.J. Guo, *Nanoimprinted Semi-Transparent Metal Electrode and its Application in OLED.* Adv. Mater., 2007. **19**: p. 1391-1396.

[86] K. Tvingstedt and O. Inganäs, *Electrode Grids for ITO Free Organic Photovoltaic Devices.* Advanced Materials, 2007. **19**: p. 2893–2897.

[87] B. O'Connor, C. Haughn, K.-H. An, K.P. Pipe, and M. Shtein, *Transparent and conductive electrodes based on unpatterned, thin metal films.* Appl. Phys. Lett., 2008. **93**: p. 223304.

[88] K. Kushida, K. Hattori, S. Arai, T. Iimori, and F. Komori, *Initial stage of Ag growth on Ge(001) surfaces at room temperature.* Surf. Sci., 1999. **442**: p. 300–306.

[89] A. Anders, E. Byon, D.-H. Kim, K. Fukuda, and S.H.N. Lim, *Smoothing of ultrathin silver films by transition metal seeding.* Solid State Commun., 2006. **140**: p. 225–229.

[90] S.G. Corcoran, G.S. Chakarova and K. Sieradzki, *Stranski-Krastanov Growth of Ag on Au(111) Electrodes.* Phys. Rev. Lett., 1993. **71**: p. 1585-1588.

[91] R. Lazzari and J. Jupille, *Silver layers on oxide surfaces: morphology and optical properties.* Surf. Sci., 2001. **482-485**: p. 823-828.

[92] D. Jeannot, J. Pinard, P. Ramoni, and E.M. Jost, *Physical and Chemical Properties of Metal Oxide Additions to Ag-SnO2 Contact Materials and Predictions of Electrical Performance.* IEEE Trans. Comp. Hybrids Manuf. Technol., 1994. **17**: p. 17-23.

[93] J. Gilot, I. Barbu, M.M. Wienk, and R.A. Janssen, *The use of ZnO as optical spacer in polymer solar cells: Theoretical and experimental study.* Appl. Phys. Lett., 2007. **91**: p. 113520.

[94] Z.B. Wang, M.G. Helander, J. Qiu, D.P. Puzzo, M.T. Greiner, Z.M. Hudson, S. Wang, Z.W. Liu, and Z.H. Lu, *Unlocking the full potential of organic light-emitting diodes on flexible plastic.* Nat. Photonics, 2011. **5**: p. 753-757.

[95] N.P. Sergeant, A. Hadipour, B. Niesen, D. Cheyns, P. Heremans, P. Peumans, and B.P. Rand, *Design of Transparent Anodes for Resonant Cavity Enhanced Light Harvesting in Organic Solar Cells.* Adv. Mater., 2012. **24**: p. 1-5.

[96] C.-Z. Li, C.-C. Chueh, H.-L. Yip, K.M. O'Malley, W.-C. Chen, and A.K.-Y. Jen, *Effective interfacial layer to enhance efficiency of polymer solar cells via solution-processed fullerene-surfactants.* J. Mater. Chem., 2012. **22**: p. 8574-8578.

[97] K.M. O’Malley, C.-Z. Li, H.-L. Yip, and A.K.-Y. Jen, *Enhanced Open-Circuit Voltage in High Performance Polymer/Fullerene Bulk-Heterojunction Solar Cells by Cathode Modification with a C60 Surfactant.* Adv. Energy Mater., 2012. **2**: p. 82-86.

[98] C.-Z. Li, H.-L. Yip and A.K.-Y. Jen, *Functional fullerenes for organic photovoltaics.* J. Mater. Chem., 2012. **22**: p. 4161–4177.

[99] S. D.Yambem, K.-S. Liao and S.A. Curran, *Flexible Ag electrode for use in organic photovoltaics.* Solar Energy Materials & Solar Cells, 2011. **95**: p. 3060–3064.

[100] C.-C. Chueh, S.-C. Chien, H.-L. Yip, J.F. Salinas, C.-Z. Li, K.-S. Chen, F.-C. Chen, W.-C. Chen, and A.K.-Y. Jen, *Toward High-Performance Semi-Transparent Polymer Solar Cells: Optimization of Ultra-Thin Light Absorbing Layer and Transparent Cathode Architecture.* Adv. Energy Mater., 2013. **3**: p. 417–423.

[101] J. Yoon, A.J. Baca, S.-I. Park, P. Elvikis, J.B.G. III, L. Li, R.H. Kim, J. Xiao, S. Wang, T.-H. Kim, M.J. Motala, B.Y. Ahn, E. Duoss, J.A. Lewis, R.G. Nuzzo, P.M. Ferreira, Y. Huang, A. Rockett, and J.A. Rogers, *Ultrathin Silicon Solar Microcells for Semitransparent, Mechanically Flexible, and Micro-concentrator Module Designs.* Nature Materials, 2008. **7**: p. 907-915.

[102] *The transparency of Samsung transparent smart window presented at 2012 international consumer electronics show (CES).* Available from: http://www.youtube.com/watch?v=mTVPVobDrms.

[103] J. Meiss, M.K. Riede and K. Leo, *Optimizing the morphology of metal multilayer films for indium tin oxide (ITO)-free inverted organic solar cells.* J. Appl. Phys., 2009. **105**: p. 063108.

[104] J. Meiss, T. Menke, K. Leo, C. Uhrich, W.-M. Gnehr, S. Sonntag, M. Pfeiffer, and M. Riede, *Highly efficient semitransparent tandem organic solar cells with complementary absorber materials.* Appl. Phys. Lett., 2011. **99**: p. 043301.

[105] J. Huang, G. Li and Y. Yang, *A Semi-transparent Plastic Solar Cell Fabricated by a Lamination Process.* Adv. Mater., 2008. **20**: p. 415–419.

[106] T. Ameri, G. Dennler, C. Waldauf, H. Azimi, A. Seemann, K. Forberich, J. Hauch, M. Scharber, K. Hingerl, and C.J. Brabec, *Fabrication, Optical Modeling, and Color Characterization of Semitransparent Bulk-Heterojunction Organic Solar Cells in an Inverted Structure.* Advanced Functional Materials, 2010. **20**: p. 1592–1598.

[107] F.-C. Chen, J.-L. Wu, K.-H. Hsieh, W.-C. Chen, and S.-W. Lee, *Polymer photovoltaic devices with highly transparent cathodes.* Org. Electron., 2008. **9**: p. 1132–1135.

[108] Y. Zhou, H. Cheun, S. Choi, W.J.P. Jr., C. Fuentes-Hernandez, and B. Kippelen, *Indium tin oxide-free and metal-free semitransparent organic solar cells.* Appl. Phys. Lett., 2010. **97**: p. 153304.

[109] Y. Zhou, H.S. Cheun, S. Choi, C. Fuentes-Hernandez, and B. Kippelen, *Optimization of a Polymer Top Electrode for Inverted Semitransparent Organic Solar Cells.* Organic Electronics, 2011. **12**: p. 827-831.

[110] K.-S. Chen, J.-F. Salinas, H.-L. Yip, L. Huo, J. Hou, and A.K.-Y. Jen, *Semi-transparent polymer solar cells with 6% PCE, 25% average visible transmittance and a color rendering index close to 100 for power generating window applications.* Energy Environ. Sci., 2012. **5**: p. 9551–9557.

[111] R.A. Chipman, *Theory and Problems of Transmission Lines,* . Schaum Outline Series1968, New York: McGraw-Hill.

[112] A. Hadipour, D. Cheyns, P. Heremans, and B.P. Rand, *Electrode Considerations for the Optical Enhancement of Organic Bulk Heterojunction Solar Cells.* Adv. Energy Mater., 2011. **1**: p. 930–935.

[113] R.F. Bailey-Salzman, B.P. Rand and S.R. Forrest, *Semitransparent organic photovoltaic cells.* Appl. Phys. Lett., 2006. **88**: p. 233502.

[114] M.-H. Chen, J. Hou, Z. Hong, G. Yang, S. Sista, L.-M. Chen, and Y. Yang, *Efficient Polymer Solar Cells with Thin Active Layers Based on Alternating Polyfluorene Copolymer/Fullerene Bulk Heterojunctions.* Adv. Mater., 2009. **21**: p. 4238–4242.

[115] R.A. Hatton, M.R. Willis, M.A. Chesters, and D. Briggs, *A robust ultrathin, transparent gold electrode tailored for hole injection into organic light-emitting diodes.* J. Mater. Chem., 2003. **13**: p. 722-726.

[116] G.H. Jung, K. Hong, W.J. Dong, S. Kim, and J.-L. Lee, *BCP/Ag/MoO3 Transparent Cathodes for Organic Photovoltaics.* Advanced Energy Materials, 2011. **1**: p. 1023–1028.

[117] R. Koeppe, D. Hoeglinger, P.A. Troshin, R.N. Lyubovskaya, V.F. Razumov, and N.S. Sariciftci, *Organic Solar Cells with Semitransparent Metal Back Contacts for Power Window Applications.* ChemSusChem, 2009. **2**: p. 309–313.

[118] R.S. Sennett and G.D. Scott, *The Structure of Evaporated Metal Films and Their Optical Properties.* J. Opt. Soc. Am., 1950. **40**: p. 203–210.

[119] L. VJ, N.P. Kobayashi, M.S. Islam, W. Wu, P. Chaturvedi, N.X. Fang, S.Y. Wang, and R.S. Williams, *Ultrasmooth Silver Thin Films Deposited with a Germanium Nucleation Layer.* Nano Lett., 2009. **9**: p. 178–182.

[120] L. Ke, S.C. Lai, H. Liu, C.K.N. Peh, B. Wang, and J.H. Teng, *Ultrasmooth Silver Thin Film on PEDOT:PSS Nucleation Layer for Extended Surface Plasmon Propagation.* ACS Appl. Mater. Interface, 2012. **4**: p. 1247–1253.

[121] X. Wang, T. Ishwara, W. Gong, M. Campoy-Quiles, J. Nelson, and D.D.C. Bradley, *High-Performance Metal-Free Solar Cells Using Stamp Transfer Printed Vapor Phase Polymerized Poly(3,4-Ethylenedioxythiophene) Top Anodes.* Advanced Functional Materials, 2012. **22**: p. 1454–1460.

[122] W. Gaynor, J.-Y. Lee and P. Peumans, *Fully Solution-Processed Inverted Polymer Solar Cells with Laminated Nanowire Electrodes.* ACS Nano, 2010. **4**: p. 30-34.

[123] Y. Xia, K. Sun and J. Ouyang, *Highly conductive poly(3,4-ethylenedioxythiophene):poly(styrene sulfonate) films treated with an amphiphilic fluoro compound as the transparent electrode of polymer solar cells.* Energy Environ. Sci., 2012. **5**: p. 5325-5332.

[124] G. Li, R. Zhu and Y. Yang, *Polymer solar cells.* Nature Photonics, 2012. **6**: p. 153–161.

[125] Y.-J. Cheng, S.-H. Yang and C.-S. Hsu, *Synthesis of Conjugated Polymers for Organic Solar Cell Applications.* Chem. Rev., 2009. **109**: p. 5868–5923.

[126] S.K. Hau, H.-L. Yip, H. Ma, and A.K.-Y. Jen, *High performance ambient processed inverted polymer solar cells through interfacial modification with a fullerene self-assembled monolayer* Appl. Phys. Lett., 2008. **93**: p. 233304

[127] F.C. Krebs, S.A. Gevorgyan and J. Alstrup, *A roll-to-roll process to flexible polymer solar cells: model studies, manufacture and operational stability studies.* J. Mater. Chem., 2009. **19**: p. 5442-5451.

[128] N. Drolet. *Organic Photovoltaic: Efficiency and Lifetime Challenges for Commercial Viability*. in *2012 MRS Spring Meeting & Exhibit*. 2012. San Francisco, CA, Moscone West Convention Center, Marriott Marquis.

[129] X. Li, W.C.H. Choy, L. Huo, F. Xie, W.E.I. Sha, B. Ding, X. Guo, Y. Li, J. Hou, J. You, and Y. Yang, *Dual Plasmonic Nanostructures for High Performance Inverted Organic Solar Cells.* Advanced Materials, 2012. **24**: p. 3046–3052.

[130] H.-L. Yip and A.K.-Y. Jen, *Recent Advances in Solution-Processed Interfacial Materials for Efficient and Stable Polymer Solar Cells.* Energy & Environmental Science, 2012. **5**: p. 5994-6011.

[131] H. Ma, H.-L. Yip, F. Huang, and A.K.-Y. Jen, *Interface Engineering for Organic Electronics.* Advanced Functional Materials, 2010. **20**: p. 1371–1388.

[132] S.K. Hau, H.-L. Yip, O. Acton, N.S. Baek, H. Ma, and A.K.-Y. Jen, *Interfacial modification to improve inverted polymer solar cells.* J. Mater. Chem., 2008. **18**: p. 5113-5119.

[133] L.J.A. Koster, E.C.P. Smits, V.D. Mihailetchi, and P.W.M. Blom, *Device model for the operation of polymer/fullerene bulk heterojunction solar cells.* Physical Review B, 2005. **72**: p. 085205.